

Numerical simulation of dislocation motion in icosahedral quasicrystals

Von der Fakultät Physik der Universität Stuttgart
zur Erlangung der Würde eines
Doktors der Naturwissenschaften (Dr. rer. nat.)
genehmigte Abhandlung

von
GUNTHER SCHAAF
aus Stuttgart

Hauptberichter: Prof. Dr. H.-R. Trebin
Mitberichter: Prof. Dr. G. Wunner

Tag der mündlichen Prüfung: 30. September 2002

Institut für Theoretische und Angewandte Physik
Universität Stuttgart
2002

Contents

Introduction	1
Zusammenfassung	3
1 Quasicrystals	13
1.1 Examples of quasicrystals	14
1.2 Structure models	15
1.3 From quasiperiodic order to quasicrystals	17
1.4 The icosahedral binary tiling (IBT)	23
2 Dislocations	27
2.1 Overview	27
2.2 Dislocations in a continuum picture	31
2.3 Dislocations in crystals	35
2.4 Plasticity	43
2.5 Dislocations in quasicrystals	45
3 Molecular dynamics	57
3.1 Statistical Mechanics	58
3.2 Integrators	61
3.3 Potential	62
3.4 Linked-cell method	63
3.5 Boundaries	65
3.6 Ensembles	68
3.7 Non-equilibrium molecular dynamics	70

4	Visualization	75
5	Results of the simulations	81
5.1	Overview	81
5.2	Simulation of a perfect sample	84
5.3	Simulations of a sample containing a dislocation	93
5.4	Energy of a model dislocation	105
6	Conclusions and outlook	119
A	Some remarks on continuum mechanics	123
A.1	Fundamentals	123
A.2	Classical theory of elasticity	124
B	Estimation of the nucleation stress of a dislocation loop	127
	List of figures	129
	List of tables	130
	References	131
	Glossary	147

Introduction

Quasicrystals, discovered in 1984 by SHECHTMAN ET AL. [1], are a new class of solids with fascinating properties. They have long range translational order, as indicated by a diffraction pattern which consists of sharp Bragg peaks. However, this order is combined with non-crystallographic symmetries. Hence, quasicrystals cannot consist of one basic structural unit periodically repeated in space. Instead, at least two such units, called *tiles*, are arranged non-periodically. In the description of an n -dimensional quasiperiodic structure more than n length scales appear. This leads to additional *phason* degrees of freedom. The lack of translational periodicity provides a challenge for solid state physicists as many established tools making use of it cannot be applied.

Like in periodic crystals, quasicrystalline plasticity is mediated by dislocations. This could be shown from measurements of their density in deformed specimens and from *in-situ* observations in a transmission electron microscope. Quasicrystals are brittle at low temperatures but ductile at temperatures above 80% of the melting temperature. Due to the non-periodicity quasicrystalline dislocations are always accompanied by a two-dimensional stacking fault. Because of its relation to phason displacements it is called *phason wall*. The interaction of dislocations with obstacles present in the structure is not yet fully understood. Several models of quasicrystalline plasticity have been proposed.

In many fields of modern physics computer simulations provide a bridge between theoretical models and experimental observations. For such a simulation a physical system is transformed into a simple model system tractable with numerical methods. In this thesis a model quasicrystal with icosahedral symmetry is constructed and stabilized with pair interactions. The evolution of the system in time is investigated

with molecular dynamics (MD), a method to solve the classical equations of motion of a many-particle system. They are integrated numerically by a discretization of time.

The physical observables are derived from the positions and momenta of the atoms. Of course, both real structures and real interactions are much more complicated than assumed in our calculations. We can therefore hardly expect an accurate quantitative description. However, we are mainly interested in a qualitative understanding of quasicrystalline plasticity.

In shear simulations on a 2D model quasicrystal at various temperatures [2, 3] the nucleation of dislocations could be observed and their motion could be studied. We have performed a similar calculation in a 3D model system and observed dislocations compatible with a Peierls-Nabarro (PN) model. The high nucleation stresses lead to partial amorphization of the structure.

In a second simulation series a single PN dislocation with the observed glide system was built into the structure. Its motion under an applied shear stress was studied at various temperatures. The dislocation was curved which indicates pinning at obstacles. The motion becomes more viscous with increasing temperature.

For an interpretation of the results a static calculation of the Peierls energy of an idealized dislocation was performed. The energy landscape provided a good explanation of the observed dislocation configurations. It was even possible to identify a specific structure element which serves as a dominant obstacle.

Outline

The first section is a brief introduction to quasicrystals. Their structure and a generation method are described as well as the model quasicrystal used in the simulations. The next section deals with the theory of dislocations and plasticity. Some basic definitions and properties are explained and extended to the quasicrystalline case, together with results of experiments and simulations. Molecular dynamics (MD) is the topic of the third section. We show how a shear deformation can be modeled. A discussion of the visualization technique follows. A chapter with the results of the simulations and a summary conclude this thesis.

Zusammenfassung

Quasikristalle sind eine relativ junge Materialklasse, die im Jahre 1982 entdeckt wurde¹. Im Beugungsbild einer Legierung der Zusammensetzung $\text{Al}_{86}\text{Mn}_{14}$ fand man scharfe Bragg-Peaks, was auf eine weitreichende Translationsordnung hinweist. Ihre Anordnung hatte jedoch die Symmetrie eines *Ikosaeders*, eine sogenannte *nichtkristallographische Symmetrie*, d.h. sie ist unverträglich mit der den periodischen Kristallen² eigenen *Translationsperiodizität*.

Ein Kristall lässt sich ausgehend von einer Einheitszelle konstruieren, z.B. einem Würfel. Durch periodisches Aneinanderreihen vieler solcher Bausteine entsteht ein translationsperiodisches Gitter. Durch Dekoration mit Atomen erhält man einen Kristall. Man kann leicht zeigen, dass nur Gitter mit zwei-, drei-, vier- oder sechszähliger Rotationssymmetrie erzeugt werden können, also insbesondere keine mit fünfzähliger Symmetrie, wie sie beim Ikosaeder auftritt. Es wurde relativ schnell klar, dass man es mit einer ganz neuen Stoffklasse zu tun hatte, die eine Art Mittelstellung zwischen den Kristallen und den amorphen Stoffen einnimmt. Wie hat man sich ihre Struktur vorzustellen?

Die Lösung fand sich in einer Arbeit aus den 1970er Jahren, in der ein nichtperiodisches Muster mit zehnzähliger Rotationssymmetrie präsentiert wurde, das *Penrose-Tiling*³. Durch Verwendung von mehr als einem Baustein konnte das kristallographische Lemma umgangen werden. Im Penrose-Tiling sind es zwei Rhomben mit Innenwinkeln,

¹In dieser Zusammenfassung geben wir keine Literaturzitate an, stattdessen verweisen wir auf die Kapitel 1–5.

²Im folgenden schreiben wir für periodische Kristalle kurz **Kristalle**. Damit sind **nicht** Quasikristalle gemeint.

³Tiling lässt sich mit „Parkettierung“ übersetzen.

die Vielfache von 36° sind.

Im Gegensatz zu Gittervektoren in Kristallen können ganzzahlige Linearkombinationen von Quasigittervektoren neue Vektoren ergeben, die zwar parallel zu den ursprünglichen Gittervektoren sind, jedoch zu diesen in einem irrationalen Längenverhältnis stehen. Es treten damit in n Dimensionen $d > n$ Längenskalen auf, was sich auch in der Zahl der Freiheitsgrade widerspiegelt. Neben den gewöhnlichen n translatorischen Freiheitsgraden, deren Anregung wie in Kristallen der Erzeugung von Phononen entspricht, gibt es $d - n$ zusätzliche Freiheitsgrade. Ihre Anregung entspricht der Erzeugung eines *Phasons* oder einem *phasonischen Flip*. Hierbei tritt eine Umordnung der Bausteine auf.

Ein (dreidimensionales) Tiling mit ikosaedrischer Symmetrie konnte ebenfalls konstruiert werden. Es besteht aus zwei verschiedenen Rhomboedern, deren Raumwinkel Vielfache von $4\pi/20$ sind. Sein Beugungsbild stimmte hinsichtlich der Positionen der Peaks recht gut mit dem von $i\text{-Al}_{86}\text{Mn}_{14}$ ⁴ überein. Durch Dekoration mit drei verschiedenen Atomen nach bestimmten Regeln erhält man ein Strukturmodell für $i\text{-AlMgZn}$. Eine binäre Dekoration (es wird nicht zwischen Al und Zn unterschieden) erweist sich als geeignet für *Computersimulationen*, da sie durch *Lennard-Jones-Paarpotenziale* stabilisiert werden kann. Wir bezeichnen die entstehende Struktur als *ikosaedrisches Binärtiling (IBT)*.

Die mechanischen Eigenschaften von Quasikristallen konnten erst mit Beginn der 1990er Jahre untersucht werden, als die Erzeugung strukturell hochperfekter Einquasikristalle möglich wurde. Quasikristalle sind spröde bei tiefen Temperaturen, werden jedoch duktil oberhalb etwa 80% der Schmelztemperatur. Dieser *Spröde-Duktil-Übergang* und die ebenfalls beobachtete *Entfestigung* (zusehends leichtere Verformbarkeit bei hohen Verzerrungen) sind zwei zentrale Aspekte der Quasikristallplastizität⁵. In verschiedenen Experimenten konnte gezeigt werden, dass sie durch *Versetzungen* verursacht wird. Wir diskutieren daher im folgenden kurz einige Eigenschaften von Versetzungen.

Versetzungen sind lineare Defekte in Festkörpern. Sie wurden in den 1930er Jahren vorgeschlagen, um die Diskrepanz zwischen den gemessenen Werten von Schubfestigkeiten in Kristallen und den theoretischen Mo-

⁴Das „i“ bedeutet ikosaedrisch.

⁵In Kristallen beobachtet man fast immer eine Verfestigung.

dellen zu erklären, die mehrere Größenordnungen betragen. Letztere gingen von einer Abgleitung zweier Kristallhälften als Ganzes entlang einer Gleitebene aus. Das hierzu notwendige simultane Brechen aller Bindungen zwischen den Hälften führte zu den hohen Werten.

Eine Stufenversetzung befindet sich am Ende einer zusätzlichen atomaren Halbebene, die in einen Kristall eingeschoben wird. Während durch Relaxationsprozesse die Atome fast überall wieder ihre ursprünglichen Positionen einnehmen, bleibt am Ende der Halbebene ein linienförmiger, topologischer Defekt erhalten. Plastische Verformung ist jetzt allein durch die Bewegung der Versetzung möglich: dann wandert die zusätzliche Halbebene durch den Kristall und führt zu einer Abscherung, sobald sie eine freie Oberfläche erreicht. Für eine solche *Gleitbewegung* müssen nur die Bindungen im Versetzungskern gebrochen werden, wofür drastisch niedrigere Spannungen ausreichen.

Bei der Deformation eines Kristalles werden oberhalb einer kritischen Spannung Versetzungsquellen aktiviert. Die neu entstandenen Versetzungen führen dann zur plastischen Verformung. Wird ihre Dichte zu hoch, so behindern sie sich gegenseitig, was zur Verfestigung führt.

Jede Versetzung ist charakterisiert durch ihren *Burgersvektor* \mathbf{b} . Er gibt die mit ihr assoziierte Verschiebung an. Eine *Stufenversetzung* ist charakterisiert durch einen Burgers-Vektor orthogonal zu ihrer *Linienrichtung* ξ . Beide Vektoren spannen die Gleitebene auf. Daneben gibt es *Schraubenversetzungen* bei denen \mathbf{b} und ξ parallel sind (und es beliebig viele Gleitebenen gibt), sowie gemischte Versetzungen mit Stufen- und Schraubenanteil. Eine Versetzung kann sich auch senkrecht zu ihrer Gleitebene bewegen, was als *Klettern* bezeichnet wird. Hierfür muss jedoch diffusive Bewegung von Atomen stattfinden, denn die Halbebene muss vergrößert oder verkleinert werden. Klettern findet daher nur bei hohen Temperaturen statt.

Durch einen Burgersumlauf um die Versetzung herum kann \mathbf{b} bestimmt werden; dies entspricht einer Integration des Verschiebungsfeldes entlang einer Kurve, die auf den Kristallgittervektoren verläuft. Burgersvektoren sind zumeist Gittervektoren, ansonsten zöge die Versetzung einen Stapelfehler mit divergenter Fehlpassungsenergie nach sich.

Die Verzerrungen in Kernnähe erzeugen ein weitreichendes Spannungsfeld mit einem charakteristischen $1/r$ -Abfall (r ist der Abstand vom Kern). Zur Berechnung der Wechselwirkung zwischen einer Versetzung und einem punktförmigen Hindernis (z.B. einem Fremdatom) wird

die *Linienspannungsnaherung* verwendet, die die Versetzung als flexible Saite mit einer gewissen Biegesteifigkeit auffasst. Das Hindernis übt eine Kraft auf die Versetzung aus und verbiegt sie. Die Gegenkraft aufgrund der Biegesteifigkeit führt zu einer Gleichgewichtskonfiguration. Die Versetzung nimmt eine gekrümmte Form um das Hindernis herum ein.

Zur Bestimmung der Kernstruktur sind atomistische Rechnungen notwendig, die meist numerisch durchgeführt werden müssen. Ein wichtiges analytisches Modell des Verschiebungsfeldes des Kernes stammt von PEIERLS UND NABARRO. Sie berechneten die Rückstellkräfte aufgrund der verzerrten Bindungen im Kern. Sie führen zu einem möglichst kleinen Kern, was jedoch eine sehr starke Kompression der Atome in Richtung von \mathbf{b} nach sich zieht. Diese verursacht wiederum eine Gegenkraft die den Kern aufweitet. Im Gleichgewicht entsteht das *Peierls-Nabarro (PN)-Verschiebungsfeld* in Form eines Arcustangens. Ein neuer Parameter taucht auf: die *Weite* des Kernes ζ . Sie entspricht der oben beschriebenen Kernausdehnung und kann auch als Halbwertsbreite der lorentzförmigen Burgersvektordichte definiert werden.

Die Bewegung einer Versetzung erfolgt in einem Potenzial, das im PN-Modell berechnet werden kann. Es ist periodisch in der Gitterkonstanten. Die Versetzung liegt bevorzugt in einem Minimum. Zu ihrer Bewegung über das nächste Maximum hinweg ist eine kritische Spannung nötig, die *Peierlsspannung*. Bei endlichen Temperaturen stellt man sich vor, dass ein Teil der Versetzung thermisch aktiviert das Maximum überwindet. Damit entstehen zwei gebogene Abschnitte, genannt *Kinken*, die sich voneinander fort bewegen, bis die ganze Versetzung das Maximum überquert hat. Man spricht vom *Peierlsmechanismus*.

Die bislang diskutierten Eigenschaften von Versetzungen lassen sich weitgehend auf Quasikristalle übertragen. Ein wesentlicher Unterschied folgt jedoch aus der fehlenden Translationssymmetrie: sich bewegende Versetzungen hinterlassen zwangsläufig einen *Stapelfehler*. Er äußert sich in veränderten Atomanordnungen, die phasonischen Flips entsprechen. Der Stapelfehler wird daher als *Phasonenwand* bezeichnet. Quasikristalline Burgersvektoren haben $d > n$ Komponenten: n phononische, die wie im kristallinen Fall die Verschiebung der Atome beschreiben und $d - n$ phasonische. Letztere parametrisieren die Dichte der phasonischen Flips in der Phasonenwand und damit deren Energie.

Der Spröde-Duktil-Übergang bei 80% der Schmelztemperatur kann

mit Hilfe der Phasonenwand verstanden werden. Die Bewegung der Versetzungen kostet Energie, sodass sie bei tiefen Temperaturen unbeweglich bleiben. Bei hohen Temperaturen kann die Phasonenwand hingegen diffusiv ausheilen, und sie werden beweglich. Auch die beobachtete Entfestigung hat ihre Ursache in der Phasonenwand, die eine Schwächung der perfekten Struktur darstellt und somit eine hocheffektive Quelle immer neuer beweglicher Versetzungen ist.

Wir diskutieren nun den mikroskopischen Mechanismus der Versetzungsbewegung. Aufgrund der fehlenden Translationssymmetrie trifft eine sich bewegende Versetzung auf unterschiedliche Atomanordnungen, die ihrer Bewegung auch unterschiedlich stark entgegenwirken. Im einfachsten Fall nimmt man einen *erweiterten Peierlsmechanismus* in einer quasiperiodischen Energielandschaft an. Die experimentelle Beobachtung langer, gerader Versetzungsabschnitte wird hierdurch erklärt.

Alternativ dazu wurde der *Cluster-Reibungs-Mechanismus* vorgeschlagen. In vielen Strukturmodellen kommen hochsymmetrische Cluster vor, die aufgrund ihrer großen Stabilität als Hindernis auf die Versetzung wirken. Die Versetzung bewegt sich leicht zwischen den Clustern, hängt an diesen jedoch fest und muss sie thermisch aktiviert überwinden.

Beide Mechanismen unterscheiden sich im *Aktivierungsvolumen* V , das in Spannungsrelaxationsexperimenten gemessen werden kann. Es kann geometrisch interpretiert werden. Z.B. ist im Peierlsmechanismus V das Produkt aus der Länge des Burgersvektors b , der Periodizität der Energiefunktion und dem Kinkenabstand. Daraus folgt dass V in der Größenordnung einiger b^3 ist. Größere Werte lassen hingegen auf strukturelle Hindernisse wie die oben beschriebenen Cluster schließen.

Um zur Aufklärung der Natur des Bewegungsmechanismus beizutragen wurde in der vorliegenden Arbeit die Versetzungsbewegung in einem einfachen ikosaedrischen Modellquasikristall in Abhängigkeit von der Temperatur auf einem Computer simuliert. Die dabei verwendete Methode der *Molekulardynamik (MD)* wird im Folgenden vorgestellt.

Mit MD bezeichnet man die numerische Lösung der klassischen Bewegungsgleichungen eines Vielteilchensystems. Durch Integration zu diskreten Zeitpunkten werden die Teilchentrajektorien im Phasenraum bestimmt. Mittels statistischer Mechanik bestimmt man aus ihnen thermodynamische Observablen wie Temperatur, Druck o.ä.

Ausgehend von einer Startkonfiguration werden die auf ein Teilchen

wirkenden Kräfte aus einem *Lennard-Jones-Potenzial* durch Gradientenbildung bestimmt. Daraus berechnet man seine Impulsänderung und seine neuen Koordinaten, dann geht der Zyklus wieder von vorne los. Das Lennard-Jones Potenzial enthält zwei freie Parameter: die Tiefe und die Position des Minimums. Letztere wurde an interatomare Abstände angepasst.

Der wesentliche Teil der Rechenzeit entfällt auf die Kraftberechnung. Sie lässt sich durch verschiedene Maßnahmen linear in der Teilchenzahl halten: da das Potenzial für große Atomabstände schnell gegen null geht, wird es oberhalb eines bestimmten Radius „abgeschnitten“, d.h. die Wechselwirkung findet nur mit den nächsten Nachbarn statt. Diese werden mit einem *Linked-Cell-Algorithmus* bestimmt.

Der verwendete Algorithmus lässt sich *parallelisieren*, wodurch sich die Rechenzeit insbesondere bei großen Teilchenzahlen stark verkürzt. Hierzu wird das Zellgitter auf ein Gitter aus Prozessoren abgebildet. Falls Atome über Prozessorgrenzen hinweg wechselwirken, muss Kommunikation zwischen den Prozessoren stattfinden. Die großen Teilchenzahlen waren nötig, um verfälschende Randeffekte möglichst auszuschalten. Aus dem selben Grund wurden häufig *periodische Randbedingungen* verwendet: Teilchen, die die Probe verlassen, kommen durch die gegenüberliegende Seite wieder zurück.

Die Simulationen wurden mit dem am Institut entwickelten Programm IMD (ITAP Molekulardynamik) durchgeführt. Es erlaubt die Simulation verschiedener thermodynamischer Ensembles, insbesondere können die Simulationstemperatur oder der -druck durch Einsatz eines Thermostaten oder eines Barostaten vorgegeben werden. Zur Simulation einer Scherdeformation wurden die Bewegungsgleichungen um einen Geschwindigkeitsgradienten erweitert; dieser erlaubt die Modellierung eines *Scherflusses*.

Ein großes Problem bestand in der Darstellung der Ergebnisse. Eine Versetzung kann im Inneren der Probe aufgrund der sich gegenseitig verdeckenden Atome nur unter Schwierigkeiten aufgefunden werden. Wir haben daher eine neue *Visualisierungsmethode* entwickelt, die Gebrauch von der starken Bindungsverzerrung in Kernnähe macht.

Anhand der defektfreien Startkonfiguration wird eine Liste aller Bindungen zwischen bestimmten Atomen aufgestellt. Eine aus der Simulation erhaltene Konfiguration wird anhand dieser Liste überprüft, und alle Bindungen entweder als intakt oder gebrochen klassifiziert. Als

Kriterium dient hierbei ihre Längenänderung bzw. die Abweichung von der ursprünglichen Orientierung im Raum. Beide Werte dürfen gewisse Schranken nicht überschreiten.

Eine vergleichbare Klassifikation der Bausteine kann durchgeführt werden. Die Darstellung der „gebrochenen“ Bausteine liefert ein Bild der Phasonenwand und des Versetzungskerns an ihrem Rand. Ferner können auch die intakten Bindungen dargestellt werden. Ergänzt durch neu hinzugekommene Bindungen, die durch die Phasonenwand hindurch laufen, erhält man ein Quasigitter, auf dem Burgersumläufe durchgeführt werden können.

Eine erste Reihe von Simulationen wurde an einer defektfreien Probe von 222.160 Atomen durchgeführt. Die Probe wurde bei konstantem Druck und verschiedenen Temperaturen geschert. Zunächst wurde ein elastisches Verhalten gefunden; oberhalb einer kritischen Spannung trat plastische Deformation auf. Aufgrund der periodischen Randbedingungen nukleierte stets eine Versetzungsschleife, die sich rasch ausdehnte. Sobald sie größer als die Probenquerabmessung war, annullierten ihre Schraubenabschnitte und zwei einzelne Stufenversetzungen blieben übrig, die rasch voneinander fortglitten. Sie erreichten etwa 75% der Scherwellengeschwindigkeit. Leider führte die Rekombination der Versetzungen nach einmaligem Durchgang zu einer partiellen Amorphisierung entlang der Gleitebene. Die Probenhälften rutschten anschließend starr aneinander ab.

Immerhin konnten aus diesen Simulationen Informationen über das bevorzugte Gleitsystem gewonnen werden: die Gleitebene war normal zu einer zweizähligen Richtung, der Burgersvektor entsprach der kurzen Diagonale der Seitenfläche eines Rhomboeders. Er lässt sich aus einer statischen Berechnung der Fehlpassungsenergie als Funktion der Verschiebung begründen: diese Funktion hat in unmittelbarer Nähe des Burgersvektors ein Minimum. Die Versetzungsweiten betragen etwa $5\sigma_0$, wobei σ_0 dem kleinsten auftretenden Atomabstand entspricht. Er ist so groß wie eine halbe Rhomboederkantenlänge.

Eine entsprechende Versetzung wurde daraufhin in eine größere Probe mit 581.612 Atomen eingebaut. Dazu wurde ein Peierls-Nabarro-Verschiebungsfeld verwendet. Die Probe wurde relaxiert, mit festen Rändern versehen und bei vorgegebenem Druck bei einer tiefen Temperatur von nahezu 0%, bei einer mittleren Temperatur von 43% und bei einer hohen Temperatur von 73% der Schmelztemperatur geschert.

Die kritische Spannung zur Auslösung der Versetzungsbewegung war um einen Faktor von 2,5 geringer. Ihr Wert kann als Abschätzung der Peierlsspannung dienen.

Bei den beiden höheren Temperaturen wurde das Aktivierungsvolumen bestimmt. Während es bei der mittleren Temperatur unrealistisch kleine Werte von $1.4b^3$ annahm, wurde bei der hohen Temperatur $6.5b^3$ gemessen. Dieser Wert ist auch relativ klein, selbst wenn ein Peierlsmechanismus angenommen wird.

Die Messwerte sind allerdings mit Vorsicht zu betrachten, da sie einerseits durch Messungen an einer Einzelversetzung gewonnen wurden, anstatt wie im Experiment an einem Ensemble aus typischerweise 10^8 Versetzungen. Des weiteren waren die Scherraten sehr hoch, sodass sich die Versetzung im wesentlichen spannungsgetrieben bewegte. Thermische Aktivierung fand zwar statt, wie wir aus den unten diskutierten mikroskopischen Beobachtungen schließen können, hat offenbar aber nur eine geringe Rolle gespielt.

Interessante Erkenntnisse ergaben sich aus einer mikroskopischen Analyse der Form und der Bewegung der Versetzungskerne. In allen Simulationen hatten wir es mit gekrümmten Versetzungen zu tun, was auf Wechselwirkung mit Hindernissen schließen lässt. Bei der Simulation mit Temperatur nahe null bewegte sich die Versetzung sprunghaft: sie verharrte lange in einer stabilen Position und sprang dann um bis zu $15\sigma_0$ weiter in eine neue, stabile Position. Die Versetzung hing dabei solange am stärksten Hindernis fest bis die akkumulierte Spannung zum Losreißen ausreichte. Ihre Trägheit bewegt sie weiter bis ein neues Hindernis stark genug war um sie erneut aufzuhalten.

Bei der mittleren und der hohen Temperatur überwandene kurze Segmente der Versetzung die Hindernisse einzeln. Sie bewegten sich auch nur wenige σ_0 weit. Insgesamt wirkt die Bewegung dadurch viskos. Daraus schließen wir auf einen — wenn auch nur geringen — thermischen Beitrag. Die Probe wird mit steigender Temperatur duktiler, da auch die Geschwindigkeit der Versetzungen zunahm. Bei der hohen Temperatur wurde auch eine Kletterbewegung beobachtet. Ursache hierfür ist die Simulationsgeometrie, die die Vergrößerung des Kernes begünstigte.

Zu einer genaueren Bestimmung des Mechanismus der Gleitbewegung haben wir ein weiteres Mal eine PN-Versetzung in die größere Probe eingebaut. Durch Variation der Kernkoordinate (des Wendepunktes des Arcustangens) konnte ihre Bewegung durch die Probe mo-

delliert werden. Als Funktion der Kernkoordinate wurde die unrelaxierte Energie der Versetzung bestimmt. Sie spiegelt einige Eigenschaften der aus dem PN-Modell hergeleiteten Energie wider, wie durch Testrechnungen an einer hexagonalen Struktur (in 2D) gezeigt werden konnte. Sowohl die Periodizität in der Gitterkonstanten als auch die Abhängigkeit von der Weite wurden korrekt reproduziert.

Rechnungen an einem 2D-Quasikristall lieferten eine in der Kernkoordinate quasiperiodische Energie. Sie wies verschiedene Extrema auf, die aus früheren Simulationen bekannten Hindernissen der Versetzungsbewegung zugeordnet werden konnten. Wir folgern hieraus, dass wir aus der Position der Extrema der Energiefunktion auf die Hindernisse der Versetzungsbewegung schließen dürfen.

Im IBT waren uns die Hindernisse zunächst nicht bekannt. Aus der beschriebenen Rechnung erhalten wir eine Energiefläche in Abhängigkeit von der Kernkoordinate und einer weiteren Koordinate, die die dazu senkrechten Richtung in der Gleitebene parametrisiert. Sie besteht **nicht** aus langen geraden Abschnitten, sodass wir einen Peierlsmechanismus ausschließen. Im Gegensatz zum Experiment haben wir ja auch keine geradlinigen Versetzungen in unseren Simulationen beobachtet. Es wäre sehr aufschlussreich, entsprechende Rechnungen an Realstrukturen durchzuführen. Leider liegen für diese unseres Wissens keine geeigneten Potenziale vor.

Werden diese gekrümmten Versetzungskonfigurationen in die Energielandschaft einbettet, sieht man, dass sie bevorzugt in den Tälern verlaufen. Dies gilt natürlich nicht überall. Z.B. kann sich die Versetzung aufgrund der Linienspannung nicht beliebig stark verbiegen und liegt in vielen Fällen auch „auf halber Höhe“. Die ermittelte Energiefläche kann offenbar die beobachteten Versetzungskonfigurationen erklären.

Indem wir die Atome hinsichtlich der Anordnung ihrer Nachbarn in Kategorien einteilen, haben wir überprüft, ob in der Nähe der Maxima eine bestimmte Atomanordnung gehäuft auftritt. Dies ist in der Tat der Fall: während alle anderen gleichmäßig über die Energielandschaft verteilt waren, war eine einzelne Anordnung stark mit den Positionen der Maxima korreliert. Sie wies die meisten Bindungen zwischen verschiedenen Atomen auf. Diese Art von Bindungen ist bei den von uns gewählten Potenzialparametern energetisch bevorzugt. Wir betrachten daher dieses Strukturelement als wichtiges Hindernis der Versetzungsbewegung.

In unseren Simulationen einer Scherdeformation des IBT konnten wir das bevorzugte Gleitsystem identifizieren. Wir haben bei verschiedenen Temperaturen die Bewegung von Versetzungen unter dem Einfluss der Scherspannung analysiert. Bei höherer Temperatur wurde die Struktur duktiler, auch beobachteten wir dort einen breiteren Versetzungskern und eine breitere Phasonenwand. Sie verbreitert sich im weiteren Verlauf der Simulation durch Diffusionsprozesse noch weiter. Bei sehr hohen Temperaturen trat auch Klettern auf.

Die Versetzungen nahmen aufgrund der Wechselwirkung mit Hindernissen eine gekrümmte Form ein. Ihr Verhalten weist Ähnlichkeiten zu den Vorhersagen des Cluster-Reibungs-Modelles auf. Es kann nicht mit einem Peierlsmechanismus erklärt werden. Ein dominierendes Hindernis konnte mit Hilfe einer statischen Berechnung der Energie einer Versetzung identifiziert werden.

Unter der Annahme, dass die Versetzungen Hindernisse überwinden indem sie eine kurze Strecke um das Hindernis herum klettern (ein Verhalten, das in Simulationen an 2D Quasikristallen bereits beobachtet wurde) könnte die Zunahme der Duktilität mit steigender Temperatur verstanden werden. Ein solches Verhalten würde auch zu den breiten Versetzungskernen und Phasonenwänden führen. Leider ist die Auflösung der von uns entwickelten Visualisierungsmethode nicht fein genug, um die Beobachtung solcher Kletterprozesse zuzulassen.

Chapter 1

Quasicrystals

The first quasicrystal was discovered in 1982 by SHECHTMAN ET AL. [1] during the investigation of rapidly cooled AlMn alloys. The electron diffraction pattern of the alloy of composition $\text{Al}_{86}\text{Mn}_{14}$ consisted of sharp Bragg peaks which form a pattern of two-, three-, and five-fold rotational symmetry (from left to right in figs. (1.1)) for specific sample orientations. The phase had icosahedral symmetry and was termed *icosahedral* AlMn (i-AlMn for short).

The sharp Bragg peaks indicate a *long range translational order* of the structure. The order cannot be crystalline¹, however, because the observed icosahedral symmetry is not compatible with translational periodicity. Indeed, the spots cannot be indexed according to any Bravais lattice. In the following years many attempts were undertaken to explain the new structure in terms of conventional crystalline models [4]. With time the sample quality increased and all these explanations failed. It became commonly accepted that a new class of solids had been discovered. The name *quasicrystal* was first introduced by LEVINE AND STEINHARDT [5].

In the first section of this chapter various quasicrystalline systems are presented as well as some of their physical properties. The important question of how to describe the structure of quasicrystals is discussed in the second section. There we also discuss a general method for their

¹Throughout this thesis the terms "crystal" or "crystalline" are used for periodic structures and **not** for quasicrystals.

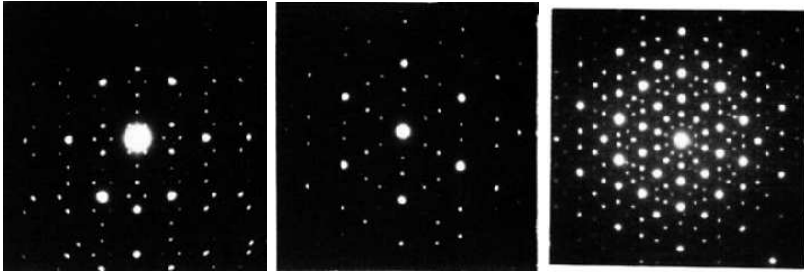


Figure 1.1: Diffraction patterns of $\text{Al}_{86}\text{Mn}_{14}$ (from [1]). The view direction is along an axis of (from left to right) two-fold, three-fold, and five-fold symmetry.

generation and give some examples. The concluding section describes several model quasicrystals which have been used in former computer simulations (and in this thesis).

1.1 Examples of quasicrystals

Up to now many other quasicrystalline systems have been discovered. Some of them had other non-crystallographic symmetries than icosahedral. BENDERSKY [6] observed an axis of ten-fold symmetry in an AlMn phase of almost identical chemical composition as i-AlMn. This *decagonal* phase belongs to the *T-phases* which possess a two-dimensional quasiperiodicity. They consist of quasiperiodic planes stacked periodically in the third direction. Within this class *octagonal* [7] and *dodecagonal* [8] quasicrystals were also found. A sample of decagonal AlCuCo is shown in the right part of fig. 1.2. Another class, the *one-dimensional quasicrystals*, have been observed in the systems AlCuMn and AlNiSi [9]. They consist of periodic planes stacked quasiperiodically.

All these quasicrystals were produced under non-equilibrium conditions and, as a consequence, were metastable. In 1986, the first thermodynamically stable quasicrystal was discovered in the system AlCuLi [10]. Millimeter-sized samples of triacontahedral morphology could be produced. They had a large degree of static disorder which can be at-

tributed to frozen-in phason strain [11, 12]. Only one year later TSAI

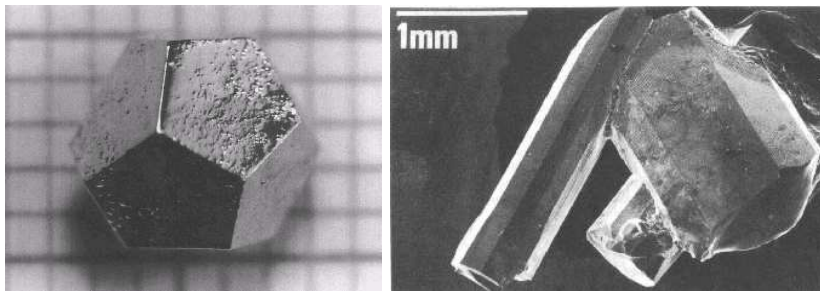


Figure 1.2: Samples of quasicrystals. Left: i-HoMgZn (from [13]), right: sample of decagonal AlCuCo (from [14]).

ET AL. [15] found a quasicrystal in the AlCuFe system by conventional solidification. Large single grains with almost no frozen-in phason strain could be grown. Many mechanical experiments which require centimeter-sized samples were performed on i-AlPdMn [16].

Until recently all known stable quasicrystals consisted of at least three metallic elements. In 2000, TSAI ET AL. [17] discovered a stable binary quasicrystal in a CdYb alloy. It is a packing of icosahedral clusters whose internal structure breaks the icosahedral symmetry.

Quasicrystals have a lot of interesting properties like a very large electrical resistivity [18] and a very low heat conductivity [19]. For details we refer to [20, 21], where also several technological applications are presented. We discuss the *mechanical* properties of quasicrystals in sec. 2.5.

1.2 Structure models

Before the discovery of quasicrystals solids were divided into two main classes: crystals which possess *long-range translational order* and amorphous structures which do not. It was commonly accepted that such an order can only be achieved by the periodic repetition of one basic structural unit in space. This is also the very construction principle

of a crystal. The counterpart to crystals are the *amorphous structures* which are not ordered on large length scales. There is only a *short-range translational order* as a result of favored interatomic distances. Quasicrystals are in an intermediate position between the two groups: on the one hand they are translationally ordered. But on the other hand their lack of translational periodicity implies a complex structure with a large variety of local atomic neighborhoods.

1.2.1 Crystals and amorphous structures

A perfect crystal is an infinite array of atoms which are located at the sites of a point set, the (*crystalline*) *lattice*². It is generated by periodic repetition of a *unit cell* spanned by d *lattice vectors* in d -dimensional space. Every vector connecting two lattice points can be written as an **integer** linear combination of the lattice vectors.

A lattice also has an *orientational order* corresponding to the orientations of the edges of the unit cell. These edges connect *nearest neighbors*, i.e., lattice sites separated by the least possible distance. We call them *bonds*³. For illustration purposes we consider a simple cubic lattice. Its unit cell is a cube whose edges define a Cartesian coordinate system. Every lattice site, and hence, every atom has six nearest neighbors. The orientational order manifests itself in the orientation of the bonds along either the x -, the y -, or the z -direction.

In x-ray or electron diffraction experiments, the diffraction pattern of the structure is observed. Translational periodicity leads to a periodic arrangement of Bragg peaks. In experiments the intensity $I(\mathbf{q})$ is measured where \mathbf{q} is the diffraction vector. $I(\mathbf{q})$ is the square of the diffraction amplitude $S(\mathbf{q})$. $S(\mathbf{q})$ is the Fourier transform of the density of the diffraction centers:

$$S(\mathbf{q}) = \int \rho(\mathbf{r}) e^{i\mathbf{q}\mathbf{r}} d^3\mathbf{r} \quad (1.1)$$

We assume that the atoms act as point-like diffraction centers. Then

²Generally, there is not only one atom, but an arrangement of several atoms, the *basis* at each lattice site.

³By “bonds” we do not mean chemical bonds, but rather lines connecting nearest neighbors.

$\rho(\mathbf{r})$ is a sum of delta distributions⁴. From eq. (1.1) follows that a periodic arrangement of delta distributions in real space becomes a periodic arrangement of delta functions in reciprocal space. This is the *reciprocal lattice* of the structure. One speaks of a *translationally ordered structure*⁵. For example, a simple cubic lattice also has a simple cubic reciprocal lattice.

The reciprocal vector \mathbf{q} of a specific Bragg peak can be decomposed into a linear combination of n reciprocal vectors \mathbf{g}_i which form a basis. The n coefficients form the *index* of the peak. In d -dimensional periodic structures $n = d$ is always fulfilled. As we will see later, $n > d$ is characteristic of quasiperiodic structures.

Translational periodicity restricts the operations which leave the lattice invariant. Let us consider rotations by angles of $2\pi/n$. We denote such a rotation *n-fold*. As KEPLER had already shown in 1619, only two-, three-, four-, and six-fold rotational symmetries are allowed in 2D and 3D⁶. All other rotational symmetries are called *non-crystallographic*. Imagine for instance a grouping of three pentagons around one point. A gap remains while three heptagons would overlap.

In amorphous structures there is translational order only on short length scales. It results from the atomic interactions that favor certain interatomic distances Δr_i . This order decays with increasing distance. As a consequence, there is no global orientational order. The diffraction pattern consists of diffuse concentric rings with radii of $2\pi/\Delta r_i$.

1.3 From quasiperiodic order to quasicrystals

How can we construct a *quasilattice*, i.e., a quasiperiodic analogue to a lattice which has the property of long-range order but no translational symmetry? The answer is to use two basic structural units and was found in an older work of PENROSE [22]: the *Penrose tiling* (left part of

⁴In the case of electron diffraction $\rho(\mathbf{r})$ corresponds to the electron charge density. An additional *structure factor* depending on the electron density distribution in the unit cell would appear in the equations.

⁵From this definition follows that both crystals and quasicrystals are translationally ordered. An older definition did not include quasicrystals.

⁶Except for the six-fold symmetry, all these are present in the simple cubic lattice.

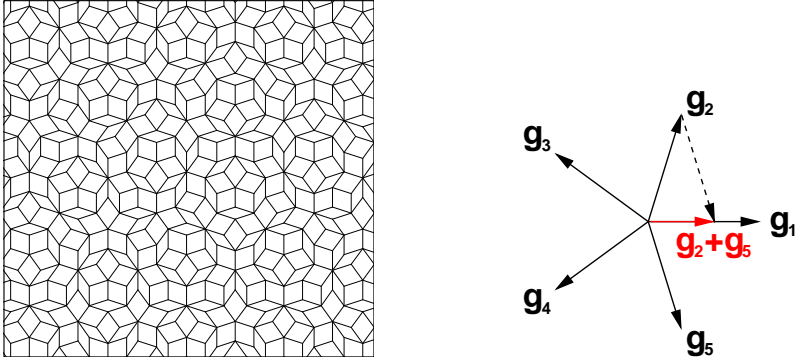


Figure 1.3: Left: Penrose tiling. The bonds are parallel to the vectors in the “five-fold star”.

(fig. 1.3). A *tiling* is a gapless, non-overlapping filling of the plane (or the 3D space) consisting of two or more *tiles*, i.e., polygons (polytopes in 3D). The Penrose tiling consists of **two** tiles, a thick and a thin rhomb arranged non-periodically. The bonds form angles which are multiples of 36° and the structure has a non-crystallographic decagonal symmetry on the average. The diffraction pattern shows a perfect decagonal symmetry.

A similar 3D structure is the *3D-Penrose tiling* [23, 24]. It has icosahedral symmetry and consists of two tiles: a prolate and an oblate rhombohedron (fig. 1.4). Their edges occur in six possible orientations corresponding to the vectors pointing from the center to the vertices of an icosahedron. Similar to crystals, the vertices are arranged on families of parallel planes. However, the interplanar distances vary in a non-periodic sequence.

Let us now define quasiperiodic order. A *quasiperiodic function* is a superposition of two harmonic functions in \mathbb{R} whose period lengths are in an irrational ratio:

$$f(x) = \sin x + \sin \alpha x, \quad \alpha \in \mathbb{R} \setminus \mathbb{Q} . \quad (1.2)$$

We perform a corresponding modulation on the points of a cubic lattice in one direction. If α were rational the new lattice would still be periodic

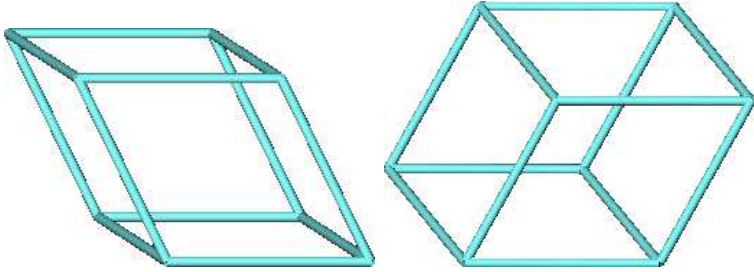


Figure 1.4: The 3D Penrose tiling consists of two tiles: a prolate (left) and an oblate rhombohedron (right).

with a larger unit cell. For irrational α a quasiperiodic structure is obtained. Its diffraction pattern still consists of sharp Bragg peaks⁷.

Quasiperiodic order is a necessary but not sufficient condition for a quasicrystal. In addition, a non-crystallographic symmetry is required⁸. However, a non-crystallographic symmetry forces quasiperiodicity. It even puts constraints on the value of the incommensurate ratio α ⁹. Consider the five vectors \mathbf{g}_i pointing from the center of a pentagon to its vertices (right part of fig. 1.3). Certain linear combinations lead to new vectors parallel to one of the \mathbf{g}_i but with an irrational length ratio (for instance $\mathbf{g}_1 - \mathbf{g}_2$ and \mathbf{g}_1). These ratios are τ, τ^2, \dots which is a direct consequence of the pentagonal order¹⁰.

We define a *quasicrystalline structure* as a quasiperiodic structure **with non-crystallographic symmetry**¹¹. The quasilattice is defined as a tiling with delta distributions at each of its vertices. To obtain a quasicrystal a *decoration* with atoms is performed according to specific rules.

⁷These Bragg peaks must be indexed by four numbers instead of three.

⁸Quasiperiodic structures with a crystallographic symmetry are called *incommensurate structures*. They serve as structure models of mercury chain salts [25].

⁹Except in the 1D case, where incommensurate structures and quasicrystals cannot be distinguished.

¹⁰ τ is the *golden mean* defined as the positive root of the polynomial $x^2 - x - 1$. Its value is $(\sqrt{5} + 1)/2 \approx 1.618034\dots$

¹¹In accordance to the definition of a translationally ordered structure we determine the non-crystallographic symmetry from the diffraction pattern.

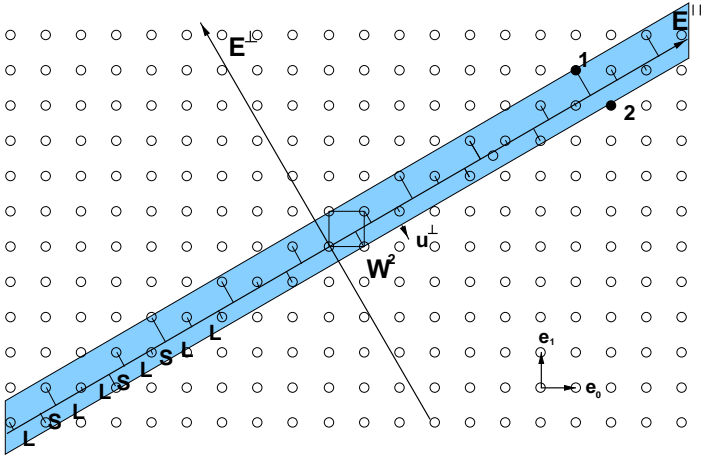


Figure 1.5: Cut and project method. The two-dimensional square lattice \mathbb{Z}^2 is projected onto the one-dimensional physical space E^{\parallel} . A 1D quasicrystal is obtained.

1.3.1 Cut and project method

In higher dimensions, periodic structures and non-crystallographic symmetries are compatible. For example, a 5D hypercube has an axis of 5-fold rotational symmetry. Hence, it is quite natural to describe quasicrystalline structures in high-dimensional space. To obtain their low-dimensional representation they are projected into low-dimensional spaces. We describe the *cut and project method* [26, 27], first at the simplest possible example: the construction of a 1D quasiperiodic chain. Then we show how to construct the Penrose tiling and the 3D Penrose tiling.

In fig. 1.5 the *physical space* E^{\parallel} is embedded into the 2D square lattice \mathbb{Z}^2 . It is a straight line through the origin with slope α . The straight line perpendicular to E^{\parallel} with slope $-1/\alpha$ is the *perpendicular space* E^{\perp} . The points of \mathbb{Z}^2 are projected on E^{\parallel} . If α were rational a periodic one-dimensional lattice would be obtained. In the case of an irrational α the projection is a dense point set. We introduce the *strip* S

constructed from the translation of the unit square W^2 along E^\parallel . The restrictions to points within S leads to a discrete point set which is **not** periodic.

The tiles are line segments between two points of the chain. There are two tiles, a long (L) and a short (S) line segment with lengths $\cos \alpha$ and $\sin \alpha$. They are the projections of the lattice vectors of \mathbb{Z}^2 . With the special choice $\alpha = 1/\tau$ the *Fibonacci chain* is obtained¹². Note that two numbers are needed to index this 1D structure.

The Penrose tiling can be constructed by a projection from \mathbb{Z}^5 onto a two-dimensional subspace E^\parallel . Its irrational embedding is realized by the condition that it has only the origin in common with the hyperlattice: $\mathbb{Z}^5 \cap E^\parallel = 0$. The projected unit vectors $\mathbf{g}_1, \dots, \mathbf{g}_5$ form the "five-fold star" of fig. 1.3. The 5D hypercube W^5 has ten 2D facets, which project onto the two Penrose rhombs, each in five different orientations.

The 3D Penrose tiling is a projection from \mathbb{R}^6 onto an irrationally embedded three-dimensional subspace E^\parallel which is invariant under the action of the icosahedral group. The projected unit vectors $\mathbf{g}_1, \dots, \mathbf{g}_6$ point to the vertices of an icosahedron. The twenty 3D facets of W^6 project on E^\parallel onto the two different rhombohedra (fig. 1.4), each in ten different orientations.

We return to the 1D case and assume a rational slope of E^\parallel . As mentioned above, the resulting structure is periodic. The period length L_n of the system increases the better the slope approximates a given irrational number. In the case of the Fibonacci chain, the approximations are the ratios of two successive Fibonacci numbers F_n and F_{n+1} . For instance, if the slope is $F_5/F_4 = 5/3$ a periodic chain with unit cell *LSLLS* and period length $3\tau + 2$ is obtained. It is called *approximant* of degree n . In the limit $n \rightarrow \infty$ the period length diverges and the structure becomes quasiperiodic.

Approximants also exist in the 2D and 3D case. They can be described as crystals with a very large unit cell. Their atomic neighborhoods correspond almost everywhere to those of a perfect quasicrystal. Some alloys of almost similar composition as a quasicrystal are described

¹²The Fibonacci chain is defined by the two substitution rules $S \rightarrow L$ and $L \rightarrow LS$ which must be applied iteratively to the initial element S . A non-periodic series of elements is obtained whose lengths correspond to the Fibonacci numbers F_n . They are defined by $F_0 := 0$, $F_1 := 1$, and $F_n := F_{n-1} + F_{n-2}$ for $n > 1$.

as approximant phases to the corresponding quasicrystalline structures.

1.3.2 Elementary excitations

Rigid displacements $\mathbf{U} \in \mathbb{R}^d$ of the periodic hyperstructure can be decomposed into displacements $\mathbf{u}^{\parallel} \in E^{\parallel}$ and $\mathbf{u}^{\perp} \in E^{\perp}$. Obviously, their dimensions are n and $d - n$. We revisit the Fibonacci chain of fig. 1.5. If there is only a displacement component $\mathbf{u}^{\parallel} \neq 0$ the atoms are shifted parallel to E^{\parallel} by \mathbf{u}^{\parallel} which corresponds to a rigid translation of the whole quasicrystal. A spatially varying \mathbf{u}^{\parallel} leads to strain and to distorted tiles. Their sequence is not changed, however. The excitation of elastic waves is also possible. From that follows that \mathbf{u}^{\parallel} corresponds exactly to (phonon) displacement in crystals.

Displacements where only the perpendicular component $\mathbf{u}^{\perp} \neq 0$ have a different effect. They are called *phason displacements*. In fig. 1.5 such a displacement is indicated by an arrow. If it is applied, certain points leave the strip S and are no longer projected. For every point that leaves the strip, another point enters through the opposite side and is projected (consider for example the points labeled 1 and 2). The result is a change in the tile sequence (from LS to SL as point 1 is replaced by point 2), a *phason flip*. This new degree of freedom is specific of quasicrystals. Its name resembles the close relation to phase shifts in a density-wave description of the free energy of quasicrystals [12].

An extension to the 2D and 3D case is straightforward. Phonon displacements distort the tiles while phason displacements cause rearrangements (phason flips) among them. In the Penrose tiling the flips occur in hexagonal arrangements of two thin rhombii and one thick rhomb. The central vertex changes its position and the same three tiles become rearranged. In the 3D-Penrose tiling the flips occur within the *rhombic dodecahedron*. This frequent structure element consists of two prolate and two oblate rhombohedra (lower part fig. 1.6). A flip changes the position of the central vertex and the four rhombohedra exchange their positions.

Hydrodynamic theory of quasicrystals predicts that, whereas the phonon strain $\nabla \mathbf{u}^{\parallel}$ relaxes rapidly, the phason strain $\nabla \mathbf{u}^{\perp}$ relaxes diffusively with extremely long relaxation times [28, 29]. Frozen-in phason strain has been observed in many quasicrystalline systems [10].

It has been suggested that phason flips have an influence on the

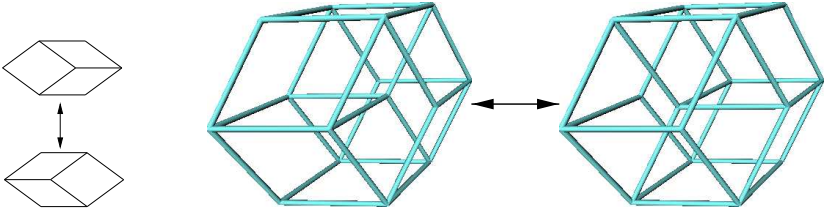


Figure 1.6: Flip in the Penrose tiling (left) and in the 3D Penrose tiling (right, see text).

transport properties of quasicrystals. In particular, a diffusion mechanism mediated by collective phason flips has been proposed [30] which should dominate the vacancy-mediated diffusion at low temperature. Indeed, in radiotracer experiments on samples of i-AlPdMn a crossover in the Arrhenius line was measured [31]. The authors proposed that at low temperatures diffusion was assisted by phason flips. Thermally fluctuating phasons have been observed *in situ* in decagonal AlCuCo [32].

1.4 The icosahedral binary tiling (IBT)

In our simulations we investigate an icosahedral model quasicrystal called the icosahedral binary tiling (IBT). It is a decoration of the 3D Penrose tiling with two types of atoms (denoted as small and large). The 3D Penrose tiling consists of a *prolate* and an *oblate* rhombohedron (left and middle part of fig. 1.4) whose edges are parallel to vectors pointing from the midpoint of an icosahedron to its vertices. They form angles of $\arccos(\tau/(2 + \tau)) \approx 63.4^\circ$ and $\arccos(-\tau/(2 + \tau)) \approx 116.6^\circ$. The unit length σ_0 used in this thesis is one half of the length of a rhombohedron edge. The vertices of the 3D Penrose tiling are aligned on families of parallel planes separated by a finite number of distances in a quasiperiodic sequence. The largest distances can be found along the two-fold directions.

The golden mean τ plays an important role in the description of the structure. For instance, in a Cartesian coordinate system spanned by

unit vectors parallel to two-fold directions the six different edges become

$$\mathbf{g}_{1/2} = c \begin{pmatrix} \tau \\ 0 \\ \pm 1 \end{pmatrix}, \quad \mathbf{g}_{3/4} = c \begin{pmatrix} \pm 1 \\ \tau \\ 0 \end{pmatrix}, \quad \mathbf{g}_{5/6} = c \begin{pmatrix} 0 \\ \pm 1 \\ \tau \end{pmatrix}. \quad (1.3)$$

where $c = 2/\sqrt{2+\tau}$. We construct approximants of the 3D Penrose tiling by replacing τ with a rational approximation F_{n+1}/F_n . This can be done with different values for each direction¹³. We denote an approximant by the three ratios of the F_n that have been used. We speak for example of a $(3/2-3/2-5/3)$ -approximant. Its length in a direction approximated by F_{n+1}/F_n is $L_n = (4/\sqrt{2+\tau})(\tau F_{n+1} + F_n)$.

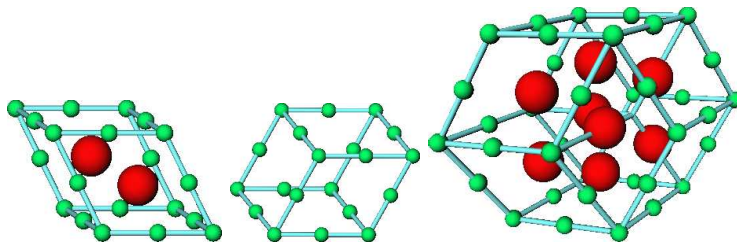


Figure 1.7: Decoration of the tiles (see text).

HENLEY AND ELSER [33] proposed a structure model for *i*-AlMgZn based on a decoration of the 3D-Penrose tiling. There exists a bcc structure with almost identical chemical composition which the authors considered as an approximant of lowest order to the icosahedral structure. From the unit cell of the bcc structure they could derive decoration rules. We present a simplified version of these rules: we do not distinguish between Al and Zn atoms.

- Small atoms (S) representing Al or Zn are placed on both the vertices and the midpoints of the edges of the oblate rhombohedron and prolate rhombohedron (fig. 1.7). Then the oblate rhombohedron is densely filled while a gap remains in the interior of the prolate rhombohedron.

¹³It is also possible to construct cuboid approximants where one edge is parallel to a three- or a five-fold axis.

- Two large atoms (L) representing Mg are placed on the long body diagonal of the prolate rhombohedron. They divide it in a ratio $\tau : 1 : \tau$.
- To better account for the stoichiometry of i-AlMgZn the decoration of the rhombic dodecahedron is modified: the atom at the central vertex is removed and its four nearest neighbors at the edge midpoints are replaced by large atoms (rightmost part of fig. 1.7)¹⁴.

The atoms are located on families of parallel planes which can be characterized by either the mean distance \bar{d} between adjacent planes or the occupation density ρ_{occ} . Large values of \bar{d} and ρ_{occ} are found normal to rotational axes. The largest values of $0.65\sigma_0$ and $0.50\sigma_0$ occur normal to a two-fold direction [34].

¹⁴Note that this modification makes the two possible configurations of an RD of fig. 1.6 indistinguishable.

Chapter 2

Dislocations

This chapter is a brief introduction to dislocation theory with the goal of understanding the specific properties of quasicrystalline dislocations. The treatment follows the monographs of HIRTH AND LOTHE [35], COTTRELL [36], and VLADIMIROV [37]. Further information on elementary dislocation theory can be found in [38, 39]. First, we define crystal dislocations and then investigate them in a continuum picture. Expressions for their long-range stress fields are derived which allow the calculation of their interaction with obstacles. Returning to an atomistic description, we present a model of the dislocation core. With its help the influence of the crystal structure on dislocation properties can be understood. Then the impact of dislocations on the plasticity of solids is discussed. In a final section all terms and properties are extended to the quasicrystalline case.

2.1 Overview

Already in the 19th century it was known that plastic deformation of metals proceeds by the formation of *slip bands*. This means that one half of a specimen *slips* with respect to the other. After the crystalline structure of metals was proven experimentally it was assumed that the slip occurred along a rational crystal plane, the *slip plane*. This assumption was corroborated by FRENKEL'S observation of steps at the

surfaces of deformed metals [40]. He estimated the *theoretical shear strength* σ_{th} of a rectangular lattice, i.e., its resistance to shear deformations to be approximately $\mu/6$ where μ is the shear modulus. In his calculation he assumed that above this stress all bonds across the slip plane would break **simultaneously**.

FRENKEL had used a sinusoidal dependence of the shear stress on the shear displacement. However, even the use of more realistic approximations of the interaction σ_{th} did not lead to values lower than $\mu/30$ which is still several orders of magnitude too large. Typical values measured in that time were in the range of 10^{-3} to $10^{-4}\mu$ ¹.

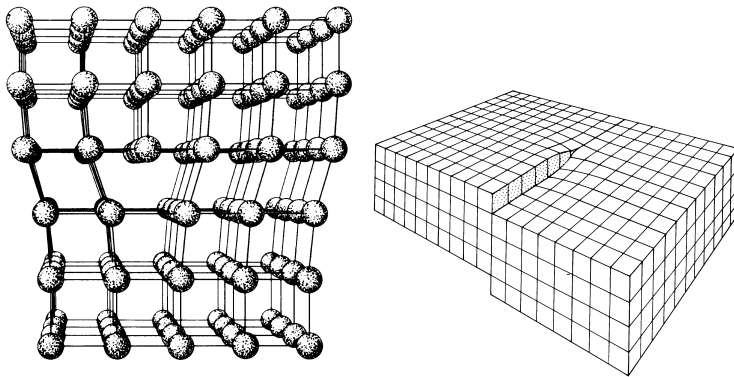


Figure 2.1: Edge and screw dislocation in a simple cubic lattice

To explain this discrepancy, several defects were proposed which can be viewed as precursors to dislocations². The *edge dislocation* (left part of fig. 2.1) was introduced independently by TAYLOR [41], OROWAN [42] and POLANYI [43] in 1934. Five years later, BURGERS [44, 45] described the *screw dislocation* (right part of fig. 2.1). Both edge and screw dislocation separate displaced from undisplaced material. They can be viewed as lines at which an extra half plane of atoms ends.

¹In the 1960s $10^{-9}\mu$ was measured in bulk copper and zinc.

²Indeed, defect-free materials like silicon wafers or thin whiskers crystals resist to slip almost up to σ_{th} .

The presence of an edge dislocation reduces the shear strength drastically (left part of fig. 2.2). By displacing only part of the upper half an edge dislocation is generated (denoted by the symbol \perp at atom b where the additional half plane ends). In the right part the dislocation and the additional half plane are located at atom c , one lattice constant to the right. To get there, **only one** bond between atoms c and f had to be replaced by another bond between atoms b and f . This is the elementary step of dislocation motion which is also called *glide motion*. It occurs already at stresses much lower than σ_{th} . When the dislocation reaches the right surface of the lattice the sample halves have slipped³ completely across the glide plane. Note that glide is a *conservative* process as it only involves the rearrangement of atoms. The term conservative means that the total number of atoms and lattice sites in the core is conserved.

Imagine now that the lowest atom row of the extra half plane in fig. 2.2 were removed. This would correspond to an edge dislocation located one lattice constant above the former. Alternatively, we could think of an associated dislocation motion **normal** to the glide plane. This motion is called *climb*. Because it involves the removal of matter it is *non-conservative*. In the atomistic picture the atoms at the end of the additional half plane would be removed, i.e., replaced by voids. This requires diffusion processes so that climb can only occur at high temperatures.

A dislocation is characterized by two vectors: the *dislocation line* ξ describing its line direction and the *Burgers vector* \mathbf{b} describing the associated displacement. Both vectors are perpendicular in the case of an edge dislocation while in the case of a screw dislocation they are parallel⁴. We define \mathbf{b} according to a procedure suggested by FRANK [46]. Consider the simple cubic lattice in the left part of fig. 2.3 spanned by the vectors \mathbf{e}_1 , \mathbf{e}_2 , and \mathbf{e}_3 (projection along $\xi \parallel \mathbf{e}_3$), the *reference configuration*. The same lattice containing an edge dislocation is shown in the right part. We divide it into a "good" region where the atoms were displaced only slightly with respect to the reference configuration

³We do not clearly distinguish between glide and slip. Normally, the term glide is reserved for the motion of a single dislocation, while slip is used in the case of multiple dislocations.

⁴In general, *mixed* dislocations occur whose Burgers vector can be decomposed into an edge and a screw component.

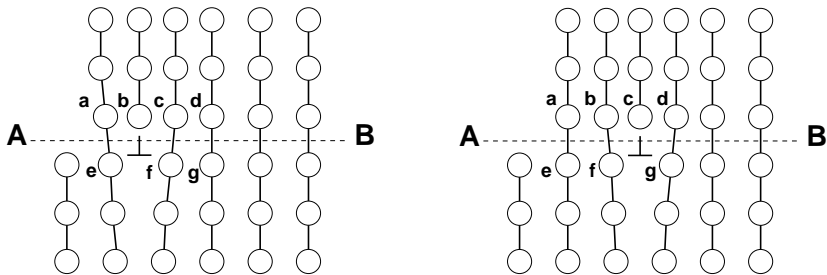


Figure 2.2: Glide motion of a dislocation leads to plastic deformation.

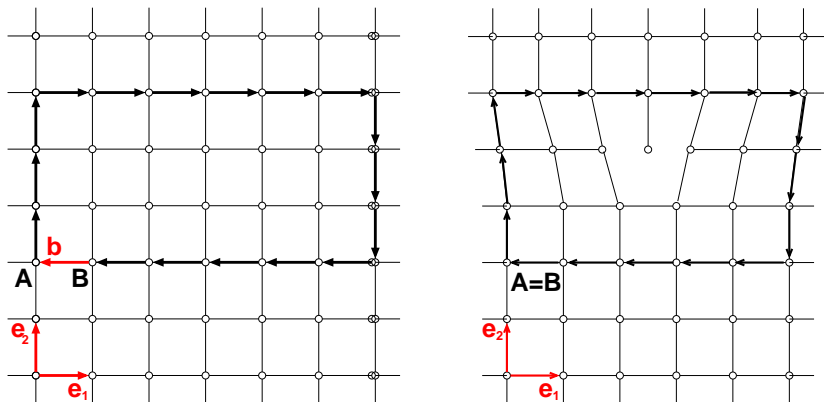


Figure 2.3: Definition of the true Burgers vector.

and a "bad" region near the dislocation line where the displacements are large.

We now perform a *Burgers circuit* around the dislocation. This is a closed path through the lattice starting at the atom labeled $A = B$ and moving step by step along the bonds. The circuit is oriented clockwise with respect to the positive \mathbf{e}_3 -direction which is equal to the $\boldsymbol{\xi}$ -direction. It encloses the dislocation and goes only through good regions. Then we draw the same circuit in the reference lattice. This means that the start atom is the same and there is a one-to-one correspondence between the bond directions in each step⁵. The new circuit ends at a different atom B . The closure failure $\mathbf{b} = -\mathbf{e}_1$, i.e., the vector necessary to close the circuit, is the *true Burgers vector*. It can also be calculated from the sum of the bond vectors of the closed circuit: $-3\mathbf{e}_2 - 6\mathbf{e}_1 + 3\mathbf{e}_2 + 5\mathbf{e}_1 = -\mathbf{e}_1$. Note that the sign of \mathbf{b} depends on the orientation of $\boldsymbol{\xi}$.

Alternatively, the closed circuit can be performed in the reference lattice to obtain the *local* Burgers vector as the closure failure in the distorted lattice. Generally, it will be different from the true Burgers vector as it includes lattice deformations. The difference can be made arbitrarily small if a circuit with large size is performed.

Note that dislocations in 2D are only characterized by their Burgers vector \mathbf{b} . The dislocation "line" degenerates to a point and it makes no sense to distinguish edge or screw dislocations. The glide plane becomes a line parallel to \mathbf{b} in which glide is possible. Climb occurs normal to this line.

2.2 Dislocations in a continuum picture

Like all defects, dislocations are sources of internal stresses. They are considerably large in the vicinity of the dislocation line and decay with distance r . A treatment by linear elasticity theory is possible if the strains are less than approximately 10%. This condition is fulfilled outside a cylinder with radius $2a$ around the dislocation line, where a is the lattice constant. The inside region is called *dislocation core*.

⁵To guarantee that this is possible we had to restrict the first circuit to good regions.

An analytical derivation of the core stresses is difficult and often atomistic calculations must be performed numerically. The long-range stress fields can be described analytically. They have an influence on large regions of the crystal because of their slow decay by $1/r$. In this section, we derive analytical expressions for them and explain various properties of dislocations, namely

- the elastic energy of dislocations,
- the forces acting on a dislocation on length scales not too small,
- the line tension approximation.

A short introduction to linear elasticity theory can be found in app. A.

A Burgers circuit in the continuum picture is done by integration along a closed contour C of arbitrary shape enclosing the dislocation line. From the displacement field $\mathbf{u}(\mathbf{x})$ the Burgers vector is calculated by contour integration

$$\mathbf{b} = \oint_C \frac{\partial \mathbf{u}}{\partial \mathbf{r}} d\mathbf{r} . \quad (2.1)$$

For example, the displacement field of a screw dislocation with $\mathbf{b} = b\mathbf{e}_z$ becomes

$$u_z(r, \theta) = b \frac{\theta}{2\pi} . \quad (2.2)$$

As a dislocation separates displaced from undisplaced regions in a material, it must not end within an otherwise perfect region. It can only end at a free surface, or at some other defect like a grain boundary, or another dislocation line. In the latter case, a **dislocation node** is formed (point O in fig. 2.4). The two Burgers circuits can be continuously deformed into one another without crossing any defects (especially no other dislocation line). From that follows $\mathbf{b} = \mathbf{b}_1 + \mathbf{b}_2$, so that the total Burgers vector is conserved. The analogy to Kirchhoff's law for electric currents is obvious. Often, this is interpreted as a *dislocation reaction* or *splitting*

$$\mathbf{b} \longrightarrow \mathbf{b}_1 + \mathbf{b}_2 . \quad (2.3)$$

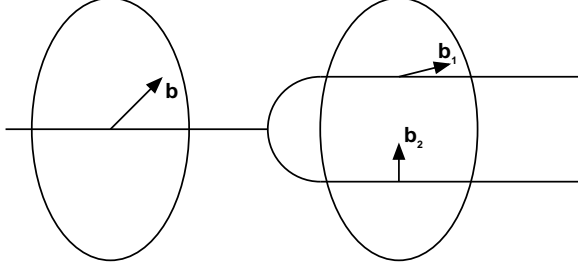


Figure 2.4: Dislocation reaction at a dislocation node. The total Burgers vector is conserved as shown by the two Burgers circuits.

2.2.1 Stress field of a dislocation

We calculate the stress field of a screw dislocation from its displacement field (eq. 2.2). With eqs. (A.3) and (A.14) and the use of polar coordinates they are

$$\sigma_{\theta z} = \frac{\mu b}{2\pi r} \quad (2.4)$$

$$\sigma_{rr} = \sigma_{\theta\theta} = \sigma_{zz} = \sigma_{rz} = \sigma_{r\theta} = 0 . \quad (2.5)$$

The calculation for an edge dislocation is similar. With a Burgers vector $\mathbf{b} = b\mathbf{e}_x$, we obtain in Cartesian coordinates (ν is Poisson's ratio)

$$\sigma_{xx} = -\frac{\mu b}{2\pi(1-\nu)} \frac{y(3x^2 + y^2)}{(x^2 + y^2)^2} \quad (2.6)$$

$$\sigma_{yy} = -\frac{\mu b}{2\pi(1-\nu)} \frac{y(x^2 - y^2)}{(x^2 + y^2)^2} \quad (2.7)$$

$$\sigma_{xy} = -\frac{\mu b}{2\pi(1-\nu)} \frac{x(x^2 - y^2)}{(x^2 + y^2)^2} \quad (2.8)$$

$$\sigma_{zz} = -\frac{\mu b}{\pi(1-\nu)} \frac{y}{(x^2 + y^2)^2} \quad (2.9)$$

$$\sigma_{xz} = \sigma_{yz} = 0 . \quad (2.10)$$

A characteristic feature is the decay of the stresses by $1/r$. From eq. (A.7) we determine the elastic energy. The integration can only be

performed between the surfaces of two cylinders with radii r_0 and R_0 , respectively. The elastic energy per unit length L becomes

$$W/L = \frac{\mu b^2}{4\pi C} \ln \frac{R_0}{r_0} \quad (2.11)$$

with $C = 1$ for a screw and $C = 1 - \nu$ for an edge dislocation.

The smaller cylinder of radius r_0 marks the limit of applicability of elasticity theory and corresponds to the dislocation core. The divergence with the upper boundary radius R_0 shows that it is not possible to assign an absolute energy to a dislocation. Instead, W depends on the choice of R_0 which is typically the distance to the next free surface where image stresses largely cancel the elastic stresses. In the case of multiple dislocations half the average distance between them is used.

Often the contribution of the logarithmic term is estimated in the following way: R_0 varies between a typical sample size like 1 cm and the minimum distance between two dislocations, $\rho^{-1/2} = 10^{-5}$ cm, with typical dislocation densities $\rho \approx 10^{10}$ cm⁻². With $r_0 = 5 \cdot 10^{-8}$ cm the logarithmic term varies between 5.3 and 17 and can be replaced by a constant. With the choice of $2\pi C$ we end up at

$$W = \frac{1}{2} \mu b^2 L . \quad (2.12)$$

2.2.2 The line tension approximation

A shear stress τ acting in the glide plane of a dislocation exerts a force F in glide direction. If the sample halves slip as a whole by b the required work is $W_1 = \tau L b$ where L is the sample length. The glide of a dislocation with Burgers vector $b\mathbf{e}_x$ through the whole sample requires work $W_2 = FL$. Because the final state is the same in both scenarios, W_1 and W_2 must be equal, yielding $F = \tau b$.

A general stress σ may also have tensile or twist components. The force in glide direction remains $F = \tau b$ where τ now is the *resolved shear stress*. It is related to σ by $\tau = m\sigma$, where m is the *Schmid factor* [47].

From the force calculated with the help *Peach-Koehler formula* $\mathbf{F} = (\boldsymbol{\sigma} \cdot \mathbf{b}) \times \boldsymbol{\xi}$ [48] where $\boldsymbol{\sigma}$ is the stress tensor follows that m is the product of the cosines of two angles, so that always $0 \leq m \leq 1$. In the case of tensile stress these are the angles between the tensile axis and the

Burgers vector direction, and between the tensile axis and the glide plane normal, respectively.

From eq. (2.12) follows that the dislocation can be viewed as a flexible string with a constant energy per unit length $W/L = \frac{1}{2}\mu b^2$. In analogy to the surface tension of a liquid W/L corresponds to a tangential force acting on the dislocation line. This force is called *line tension force*. To determine the shape of pinned dislocations under the action of a resolved shear stress τ we assume that the segments between the pinning points bulge out due to the force τb . This force is compensated by W/L and the radius of curvature becomes

$$R = \frac{W}{\tau b} . \quad (2.13)$$

This *line tension approximation* ignores contributions from other segments of the dislocation. It is a good approximation as long as the logarithmic term of the elastic energy varies only slowly, which is the case for dislocations which are bowed only slightly. *Frank-Read sources* [49], the most important sources of dislocations can be explained within this picture.

2.3 Dislocations in crystals

From its definition in sec. 2.1 the Burgers vector of a dislocation in a simple cubic lattice was related to a lattice vector. Generally, this is true in all crystalline lattices. The edge dislocation of fig. 2.2 has a Burgers vector which corresponds to a lattice vector. Because lattice vectors connect equivalent atomic sites the atoms are in perfect alignment across the glide plane except for the dislocation core. There is a finite misfit energy localized near the core. Such a dislocation is termed *perfect*.

If the Burgers vector were a fraction of a lattice vector a different type of configuration would result. In the whole displaced part on one side of the dislocation the atoms would be misaligned across the glide plane. In addition to the core energy this would lead to a long-range, divergent misfit energy contribution. Apart from partial dislocations to be discussed in sec. 2.3.4 crystal dislocation are in general perfect.

Perfect dislocations are stable if and only if they have the shortest possible Burgers vector. The reason is the elastic energy of a dislocation

which is proportional to b^2 (cf. eq. (2.11)). If $\mathbf{b} = \mathbf{b}_1 + \mathbf{b}_2$ is the sum of two lattice vectors the dislocation will split if and only if

$$b^2 > b_1^2 + b_2^2 . \quad (2.14)$$

because then the elastic energy is reduced [50]. Eq. (2.14) is fulfilled if the angle between \mathbf{b}_1 and \mathbf{b}_2 is acute. In particular, a perfect dislocation with a Burgers vector $n\mathbf{b}$ dissociates into n perfect dislocations with Burgers vector \mathbf{b} .

2.3.1 Structure of the dislocation core

Only a limited understanding of crystal dislocations can be gained from the investigation of their elastic fields. It is also necessary to study the dislocation core in an atomistic picture. Answers to the following questions can be found:

- What is the force necessary to move a dislocation through a crystalline lattice?
- What are the preferred slip systems?
- Why do some crystals show brittle behavior while others are ductile?

The dislocation core is the transition region between slipped and unslipped material in the glide plane. An important parameter is its *width* ζ which measures the sharpness of this transition (cf. fig. 2.5). A transition across an interval of, say, one or two atomic spacings leads to a *narrow* dislocation core, otherwise to a *wide* core. We define ζ more precisely in sec. 2.3.2. Obviously, $\zeta = 0$ for the continuum dislocations.

Two factors determine its value. In the case of the edge dislocation of fig. 2.5 the elastic energy of the crystal stored in the compressed upper atom row tends to increase ζ . Competing with this, the misfit energy due to the misalignment between the two atom rows decreases ζ . The mobility of a dislocation increases with increasing ζ . As the elastic energy is proportional to the elastic constants of the crystal, we expect wider dislocations in metals of simple crystal structure like fcc or hcp compared to homopolar crystals with strongly directed bonds like in diamond. This is the main reason for the ductility of many metals and the brittleness of most non-metallic crystals.

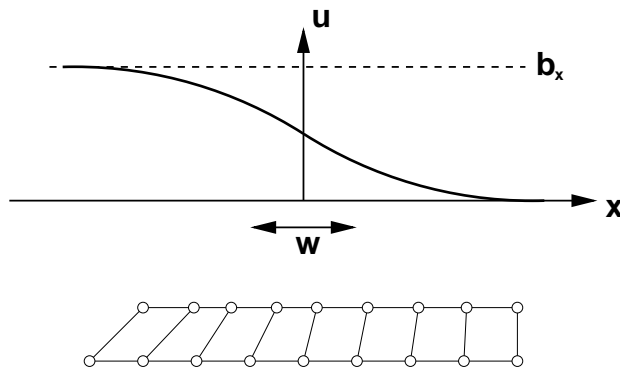


Figure 2.5: Width of a dislocation.

2.3.2 The Peierls-Nabarro model of a dislocation

Already in the 1930s, models of dislocation core structures were presented [51, 52]. In 1940, PEIERLS [53] presented an expression for the displacement field of a $[001]$ edge dislocation on a $\{010\}$ plane in a 3D simple cubic crystal. Its Burgers vector had a length of b , equal to the lattice constant. In addition, the critical stress for the motion of such a PEIERLS-NABARRO (PN) dislocation was estimated. Later, his work was extended by NABARRO [54]. In the following, we summarize their treatment.

The origin of the coordinates is at the dislocation core, the glide plane is given by $y = 0$ (fig. 2.6). An initial disregistry of $b/2$ (of $-b/2$) is imposed to the part above (below) the glide plane. Then a displacement $u(x)$ in x -direction is added above the glide plane, and, by symmetry, $-u(x)$ below. The y -component of the displacement shall be negligible. The **relative** displacement of two atoms facing each other across the glide plane $x = 0$ is

$$\phi(x) = 2u(x) \pm \frac{b}{2} \quad (\pm x > 0) \quad (2.15)$$

The necessity of perfect alignment at infinite distances on both sides of

the core ($\phi(\pm\infty) = 0$) forces the boundary conditions

$$u(\pm\infty) = \mp \frac{b}{4} . \quad (2.16)$$

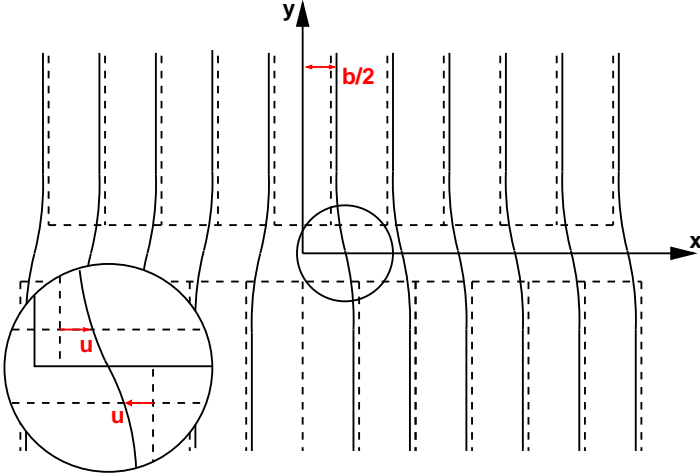


Figure 2.6: Initial disregistry and PN displacement field (see text).

The misalignment of the atoms across the glide plane leads to a stress σ_{xy} . We assume a sinusoidal dependence on the displacement u

$$\sigma_{xy}(u) = \frac{\mu d}{2\pi b} \sin \frac{2\pi u}{d} \quad (2.17)$$

where the constant is evaluated from Hooke's law in the limit of small u [40]. The competing stress caused by the elastic distortion of the crystal is described by a continuous distribution of infinitesimal dislocations along the x -axis with a Burgers vector density $b'(x') = -2(du/dx)dx'$. According to eq. (2.6) this distribution of dislocations produces a shear stress

$$\sigma_{xy} = -\frac{\mu}{2\pi(1-\nu)} \int_{-\infty}^{\infty} \frac{b'dx'}{x-x'} = -\frac{\mu}{\pi(1-\nu)} \int_{-\infty}^{\infty} \frac{\frac{du}{dx}|_{x=x'}dx'}{x-x'} . \quad (2.18)$$

in the glide plane where $y = 0$ ⁶. Equilibrium of the two stresses leads to the PN integro-differential equation

$$\int_{-\infty}^{\infty} \frac{du}{dx'} \Big|_{x=x'} dx' = \frac{b(1-\nu)}{2d} \sin \frac{4\pi u}{b} \quad (2.19)$$

whose solution (together with the boundary conditions of eq. (2.16))

$$u(x) = -\frac{b}{2\pi} \arctan \frac{x}{\zeta} \quad (2.20)$$

is the PN displacement field. The width $\zeta = d/2(1-\nu)$ is a rough measure of the extent of the core: within the region $|x| < \zeta$ the displacements are less than $b/8$, one-half of the values at infinity.

Note that the PN dislocation has a rather small width of about $1.5b$ so that the basic assumptions of the treatment can hardly be justified. Several attempts have been made to derive more general solutions. For example, FOREMAN ET AL. have used a function $u(x)$ with the correct periodicity and limiting behavior (i.e., satisfying Hooke's law at small strains) and obtained wider dislocation cores [55].

2.3.3 Force required to move a dislocation through a lattice

The energy of the PN dislocation consists of two parts: first there is an elastic strain energy stored in the two halves which has a constant value

$$W = \frac{\mu b^2}{4\pi(1-\nu)} \ln \frac{r}{2\zeta} \quad (2.21)$$

that can be obtained from an integration of eq. (2.18). The result is in agreement with eq. (2.11) if we set $r_0 = 2\zeta$. The second part corresponds to the misfit energy across the glide plane. An integration of eq. (2.17) yields an expression of the misfit energy per pair of atom rows

$$\tilde{W} = \frac{\mu b^2}{8\pi^2} \left(1 + \cos \frac{4\pi u}{b}\right). \quad (2.22)$$

⁶By symmetry, a dislocation produces no shear stress at its center so that eq. (2.18) can be evaluated using the Cauchy principal value of the integral.

We insert the PN displacement field $u(x + \alpha b)$ where α is a parameter whose increase from 0 to 1 describes an elementary step of glide motion. Summing over all pairs \tilde{W} leads to a series with solution [56]:

$$W(\alpha) = \frac{\mu b^2}{4\pi(1-\nu)} + \frac{W_P}{2} \cos 4\pi\alpha, \quad (2.23)$$

where

$$W_P = \frac{\mu b^2}{2\pi(1-\nu)} \exp -\frac{4\pi\zeta}{b} \quad (2.24)$$

is the *Peierls energy*. $W(\alpha)$ varies periodically with α . The *Peierls stress*

$$\sigma_P = \frac{1}{b^2} \max\left(\frac{\partial W(\alpha)}{\partial \alpha}\right) = \frac{2\mu}{1-\nu} \exp -\frac{4\pi\zeta}{b} \quad (2.25)$$

is the stress required to overcome the potential barrier. It is an estimate of the lattice resistance to dislocation-mediated plastic deformation at zero temperature.

σ_P increases monotonically with increasing b/d . As $d \propto \zeta$, wide dislocations are more mobile. Furthermore, we conclude that slip occurs preferably in close-packed crystal planes because between them d is maximal. The slip direction is determined by the lowest possible inter-atomic distances in the glide plane which make b minimal. An example is the preferred $\{111\}\frac{1}{2}\langle 110\rangle$ slip system in fcc crystals.

The Peierls stress is approximately $3.6 \cdot 10^{-4}\mu$ for $\nu = 0.3$. This is rather large compared to the critical shear stress of soft metal crystals ($\approx 10^{-5}\mu$). The reason is the small width of the PN dislocation and also the disregard of displacement components u_y which would also facilitate the core motion. FOREMAN ET AL.'s treatment lead to wider dislocations and also predicted a greater mobility in good agreement with experimental values.

The form of eq. (2.24) is not at all what would be expected. The period length should be equal to 1.0 (or to a displacement equal to the lattice constant b) but is only half as large. The symmetric dislocation configurations $\alpha = 0$ where the core is located in-between two atoms of the lower sample half is **not** a minimum energy configuration. Instead the non-symmetric configuration $\alpha = 1/4$ is minimal. A more recent treatment by WANG [57] who used a different summation method lead to an expression with both the correct periodicity and the correct positions

of the minima (replace $\cos 4\pi\alpha$ with $\sin 2\pi\alpha$ in eq. (2.23)). The Peierls stress is lower by a factor of 2.

The periodicity of the Peierls energy leads to a strong, temperature-dependent lattice friction stress. We attempt to understand the nature of this stress by investigating the motion of a dislocation through the Peierls energy landscape. In fig. 2.7 a dislocation is pinned at the points A and E within its glide plane. They might be point defects or the points of intersection with other dislocations. The solid lines represent minima of the Peierls energy, the *Peierls valleys*, separated by a . Between two Peierls valleys there is a maximum of the Peierls energy, a *Peierls hill*, represented by a dashed line. For geometrical reasons, there **must** be at least one configuration like that at B where the dislocation line lies across a Peierls hill. Such a configuration is called *kink*. Thermal fluctuations may lead to configurations such as the *kink pair* at C and D . At finite temperatures, dislocation segments glide by thermally assisted generation of kink pairs. The two kinks separate until they reach the ends of the segment so that the dislocation has moved to the next valley. This kind of motion is called *Peierls mechanism*. The two kinks attract each other with a force proportional to $1/L^2$, where L is their separation.

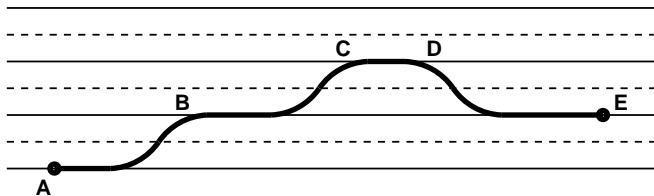


Figure 2.7: Peierls mechanism. Thermal activation leads to a kink-pair (configuration BCDE). The kinks separate and the dislocation moves to the next Peierls valley.

2.3.4 Partial dislocations and gamma surface

In some crystals there are glide systems in which stacking faults have a relatively low misfit energy compared to the core energy. An example is

the $\{111\}\frac{1}{2}\langle 110\rangle$ slip system in fcc. Such crystals contain imperfect, or *partial* dislocations with which a low-energy stacking fault is associated. This can be understood with the help of the *gamma surface* γ of the structure. $\gamma = \gamma(\mathbf{u})$ is defined as the generalized stacking fault as a function of rigid displacement \mathbf{u} of two halves of a crystal across a given glide plane [58]. After applying the displacement, the potential energy is computed from a suitable atomic interaction. The gamma surface of a $\{111\}$ plane of an fcc structure is displayed in fig. 2.8. The interaction was modeled with pair potentials of Lennard-Jones type (cf. sec. 3.3).

A rigid translation by a lattice vector leads to a configuration indistinguishable from the reference configuration. Both have the same potential energy which is a minimum of the gamma surface⁷. Hence, the gamma surface must reflect the periodicity of the lattice. The symmetry of the lattice plane and the nature of the atomic interactions also have an influence on its shape. The Burgers vector of the $\frac{1}{2}\langle 110\rangle$ -dislocation corresponds to the point denoted by (1) in fig. 2.8. It connects equivalent atoms denoted by A.

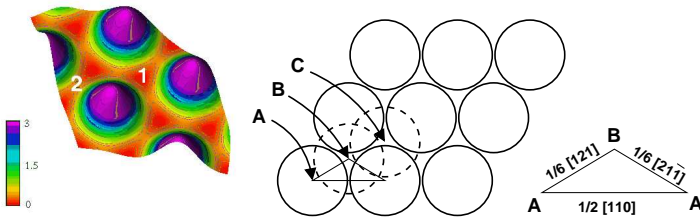


Figure 2.8: Gamma surface of the $\{111\}$ -plane of an fcc crystal. The numbers denote a $\frac{1}{2} [110]$ -displacement (1) connecting two A positions and a $\frac{1}{6} [121]$ -displacement (2) connecting A with B (see text).

This dislocation is not stable, however. It splits into two *Shockley partials* according to the reaction

$$\frac{1}{2} [110] \longrightarrow \frac{1}{6} [121] + \frac{1}{6} [21\bar{1}] \quad . \quad (2.26)$$

⁷This is just another formulation of the concept of perfect dislocations.

Besides the lower elastic energy (cf. eq. (2.14)) the large core energy is the reason for the splitting. It manifests itself in the large hill between the origin and position (1) in fig. 2.8. The first partial dislocation connects the origin where an atom of the layer A is located with position (2) which corresponds to position B of the layer above (see the middle part of fig. 2.8 for the arrangement of the layers). It produces a stacking fault with a low misfit energy corresponding to γ at position (2). The total misfit energy is finite because the stacking fault is terminated by the second partial as shown in the right part.

2.4 Plasticity

In this section we are going to discuss experimental results and theoretical models for crystal plasticity. We assume that plastic behavior is mediated by dislocations and explain the experimental observations with some of their properties. In the left part of fig. 2.9 a typical

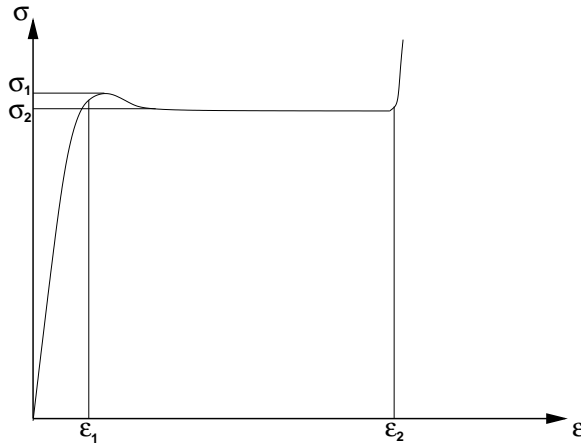


Figure 2.9: Idealized stress-strain curve.

stress-strain curve of a crystal deformed in a compression experiment is displayed. The sample is loaded by an external stress σ at a constant rate and the strain ϵ is measured. The curve consists of three regions:

- *elastic regime* ($\varepsilon < \varepsilon_1$): the sample is deformed elastically. In the limit of small ε Hooke's law (eq. (A.8)) is valid.
- *plastic flow regime* ($\varepsilon_1 < \varepsilon < \varepsilon_2$): dislocations start to move and enable a large increase of strain with almost no increase of the external stress. The dislocation density increases as dislocation sources become activated. The deformation is no longer reversible: if the stresses are removed there remains *plastic strain* ε_{pl} .
- *work hardening regime* ($\varepsilon > \varepsilon_2$): a further increase of strain requires a large increase of external stress. The dislocations become immobile due to their mutual interaction. This effect is called *work hardening*.

The stresses σ_1 and σ_2 are the *upper* resp. *lower yield stress*.

At elevated temperatures plastic deformation of crystals has been established as a thermally activated process. It depends upon temperature and strain rate. The *thermodynamic activation parameters* which provide insight into the microscopic deformation mechanism can be calculated from the temperature dependence of both stress and strain. Therefore, the plastic deformation experiments described above are performed at various temperatures. *Stress relaxation experiments* where the loading is stopped so that the total strain is constant turn out to be useful for the evaluation of the thermodynamic activation parameters. We describe the interpretation of such experiments following the outline of EVANS AND RAWLING [59].

The *plastic strain rate* $\dot{\varepsilon}_{\text{pl}}$ is related to dislocation velocity v by the *Orowan equation*

$$\dot{\varepsilon}_{\text{pl}} = \rho b v \quad (2.27)$$

where b is the modulus of the Burgers vector and ρ is the *dislocation density* per unit area. It depends on temperature according to

$$\dot{\varepsilon}_{\text{pl}} = \dot{\varepsilon}_0 \exp\left(-\frac{\Delta G(\sigma)}{k_B T}\right) \quad (2.28)$$

where k_B is Boltzmann's constant, T is the absolute temperature, and $\dot{\varepsilon}_0$ is a pre-exponential factor supposed to be constant. $\Delta G = \Delta H - T\Delta S$ is the activation Gibbs free enthalpy, ΔH is the activation enthalpy and ΔS the activation entropy. In general, $\dot{\varepsilon}_{\text{pl}}$ depends also on the resolved

shear stress $\tau = m\sigma$ where σ is the external shear stress (cf. sec. 2.2.2). The following thermodynamic relation connects ΔG and σ

$$\frac{\partial \Delta G}{\partial \sigma} \Big|_T = -mV \quad (2.29)$$

where V is the *activation volume*. Together with eq. (2.28) we obtain

$$\frac{\partial \ln \dot{\varepsilon}_{\text{pl}}}{\partial \sigma} \Big|_T = \frac{mV}{k_B T} . \quad (2.30)$$

In a stress relaxation experiment the total strain is constant:

$$0 = \dot{\varepsilon}_{\text{tot}} = \dot{\varepsilon}_{\text{pl}} + S\dot{\sigma} \quad (2.31)$$

where S is the elastic compliance. With eq. (2.30) the activation volume becomes

$$V = -\frac{k_B T}{m} \frac{\partial \ln(-\dot{\sigma})}{\partial \sigma} \Big|_T . \quad (2.32)$$

It can be determined from the slope of a $\ln(-\dot{\sigma})$ versus σ plot at constant temperature. The quantity $I := \partial \ln(-\dot{\sigma})/\partial \sigma$ is called *strain-rate sensitivity*.

The magnitude of the activation volume is related to the type of obstacles that controls the motion of the dislocation. The dislocation provides only one length scale, the modulus b of the Burgers vector. $A := V/b$ is the *activation area*. In the case of localized obstacles a geometrical interpretation of A is possible. For the Peierls mechanism (fig. 2.7) $A = ld$ is the area between the two kinks of a kink pair. l is their separation length and d is the spacing between the Peierls hills. Typically, V is of the order of a few b^3 . Larger values indicate that larger structure elements are the dominant obstacles.

2.5 Dislocations in quasicrystals

2.5.1 Extended elasticity theory of quasicrystalline dislocations

Classical elasticity theory can be extended to quasicrystals if the additional phason degree of freedom \mathbf{u}^\perp is included in the description.

BACHTLER AND TREBIN have investigated the fundamental equations of elasticity for icosahedral quasicrystals [60]. Group theory predicts five independent elastic constants, two of them describing the phonon part of the elastic energy, as in the isotropic case. Two others are related to the phason part and the remaining one is a coupling constant between the phonon and the phason part.

As in crystals, dislocations are viewed as singularities of the displacement field. However, the high-dimensional displacement field \mathbf{U} in the hyperspace must be taken into account. Burgers vectors are closure failures of circuits in hyperspace

$$\mathbf{B} = \oint_C d\mathbf{U} . \quad (2.33)$$

From the decomposition of the displacement field in phonon and phason parts follows a similar decomposition of \mathbf{B}

$$\mathbf{B} = \mathbf{b}^{\parallel} + \mathbf{b}^{\perp} = \oint_C d\mathbf{u}^{\parallel} + \oint_C d\mathbf{u}^{\perp} \quad (2.34)$$

into the phonon component \mathbf{b}^{\parallel} and the phason component \mathbf{b}^{\perp} .

In the case of icosahedral symmetry both components are 3D vectors which can be determined from Burgers circuits. Returning to a discrete description in terms of a quasilattice, we again define perfect quasicrystalline dislocations whose Burgers vectors are integer linear combinations of hyperlattice vectors. It can be shown that then both \mathbf{b}^{\parallel} and \mathbf{b}^{\perp} are non-zero.

The physical meaning of \mathbf{b}^{\parallel} is the same as in crystals. \mathbf{b}^{\perp} , however, is related to the stacking fault created by a moving dislocation due to the non-periodicity of the structure. We consider fig. 2.10 where two crystal halves (left part) resp. two quasicrystal halves (right part) are displaced with respect to each other along a glide plane. The atomic planes normal to the glide plane are sketched as lines. While the crystalline lattice is reconstructed perfectly a planar stacking fault appears in the quasicrystalline case: some planes are discontinuous across the glide plane. These discontinuities can be viewed as phason flips (cf. fig. 1.5) and the resulting stacking fault is called *phason wall*. The density of phason defects, and hence the energy of the phason wall, is parameterized by \mathbf{b}^{\perp} . It follows that dislocation glide is continuously

dissipative and must continuously introduce disorder in the glide plane.

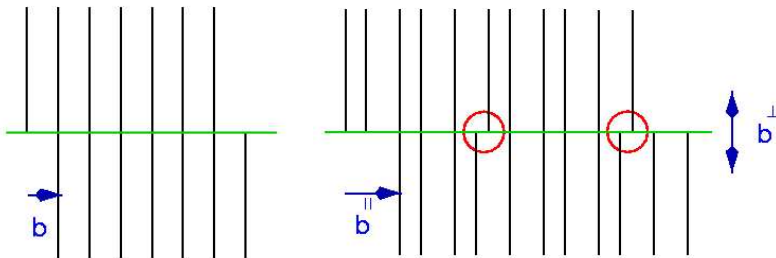


Figure 2.10: Phason wall. Left: a displacement of two crystal halves along a plane leaves behind a perfectly reconstructed lattice (the lines indicate atomic planes of atoms normal to the glide plane). In a quasicrystal (right) a stacking fault with phason flips appears as discontinuous lines. \mathbf{b}^\perp parameterizes their density and the misfit energy.

2.5.2 Experiments

While the concept of a dislocation in a quasicrystal was soon established, it took a long time until experimental data of plastic properties of quasicrystals became available⁸. Due to the polycrystalline character of the early samples only micromechanical investigations could be performed [62].

In deformation experiments on poly-grained samples of different alloys a characteristic *brittle-to-ductile transition* was observed [63, 64, 65, 66]. It always occurred at approximately 80% of the melting temperature. FRIEDEL [67] has pointed out that this behavior is not very different from that of metallic glasses below and above the glassy transition temperature T_g .

In 1990, the discovery of a stable icosahedral phase in the system $i\text{-AlPdMn}$ [16] allowed the production of centimeter-sized samples of

⁸We restrict ourselves to the description of icosahedral quasicrystals. Information on decagonal quasicrystals can be found in [61].

single quasicrystals. In fig. 2.11 the stress-strain curve measured in i-AlPdMn at 750° C (above the transition temperature) is displayed [68]. After a yield point at 370 MPa the sample deforms plastically. No work hardening can be observed. Instead the stress decreases with further deformation up to strains of 25%, an effect called *softening*⁹. In recent measurements up to very large strains a weak work-hardening stage was observed at a strain of 60% [70].

WOLLGARTEN ET AL. found strong evidence that a dislocation mechanism is responsible for the plastic deformation¹⁰. They measured the dislocation density before and after the deformation and found an increase by two orders of magnitude [72]. Later they observed a moving dislocation *in situ* in a deformation experiment performed in a transmission electron microscope (TEM) [73]. Frequently, splitting of the dislocations was observed. The partials then moved on parallel glide planes¹¹.

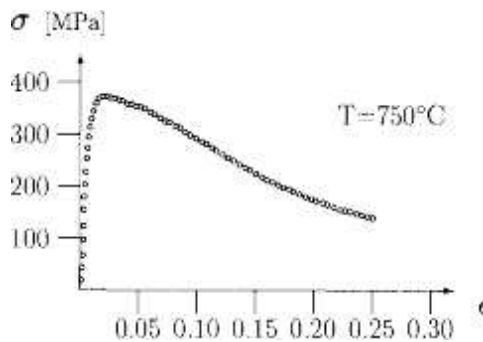


Figure 2.11: Stress strain curves in i-AlPdMn (from [68]).

⁹and often **incorrectly** referred to as *superplasticity*. This term is reserved to grain boundary sliding in polycrystalline alloys [69].

¹⁰In microstructural investigations at room temperature evidence was found that fragmentation processes rather than dislocations mediate plastic deformation [71].

¹¹Such a behavior is a prerequisite for several dislocation multiplication mechanisms like a Frank-Read source [49].

The two characteristic features of quasicrystal plasticity

1. Brittle-to-ductile transition
2. Softening

can be explained with the phason wall. Phason strain is supposed to relax slowly, i.e., comparable to diffusive processes [29] which makes the dislocations almost immobile at low temperatures. At temperatures above the brittle-to-ductile transition annealing of the phason wall leads to mobile dislocations. Additionally, the phason wall weakens the formerly perfect quasicrystal, thus facilitating the generation of mobile secondary dislocations. This effect leads to softening as it overcompensates the work hardening which also occurs due to the mutual interaction of the dislocations.

Quasicrystalline dislocations can be observed in TEM micrographs because their strain field produces a diffraction contrast. In crystals, the direction of the Burgers vector \mathbf{b} is determined by the *extinction condition* $\mathbf{g} \cdot \mathbf{b} = 0$, where \mathbf{g} is a diffraction vector used for imaging [74]. In quasicrystals, this condition must be evaluated in the hyperlattice and, hence, splits into a phonon and a phason part

$$\mathbf{G} \cdot \mathbf{B} = \mathbf{g}^{\parallel} \cdot \mathbf{b}^{\parallel} + \mathbf{g}^{\perp} \cdot \mathbf{b}^{\perp} = 0 . \quad (2.35)$$

Eq. (2.35) can be fulfilled in two different ways [75, 76]. The *strong extinction condition (SEC)*

$$\mathbf{g}^{\parallel} \cdot \mathbf{b}^{\parallel} = \mathbf{g}^{\perp} \cdot \mathbf{b}^{\perp} = 0 \quad (2.36)$$

is equal to the crystalline case. The *weak extinction condition (WEC)*

$$\mathbf{g}^{\parallel} \cdot \mathbf{b}^{\parallel} = -\mathbf{g}^{\perp} \cdot \mathbf{b}^{\perp} \quad (2.37)$$

is characteristic of dislocations in quasicrystals.

With *convergent-beam electron diffraction (CBED)* it is even possible to determine the magnitude of the Burgers vector [77]. ROSENFELD ET AL. [78] have performed a detailed analysis of dislocations in i-AlPdMn and found that about 90% of the dislocations were perfect dislocations with a Burgers vector parallel to a two-fold direction. The rest were

partial dislocations with Burgers vectors pointing along five-fold, three-fold, and pseudo-two-fold directions. The major slip planes were two-fold and three-fold planes. In deformed samples the same results were found.

The *strain accomodation parameter* $\zeta := |\mathbf{b}^{\parallel}|/|\mathbf{b}^{\perp}|$ is the ratio of the moduli of the Burgers vector components. While ζ did not depend on the temperature, its value decreased with increasing strain. A possible explanation is dislocation splitting which always leads to a lower value of ζ .

Phason walls, both caused by indentation [66] and by deformation of i-AIPdMn at various temperatures [79, 80] have also been observed in diffraction contrast. In these experiments also the broadening and disappearing of the phason wall due to intense diffusion could be observed.

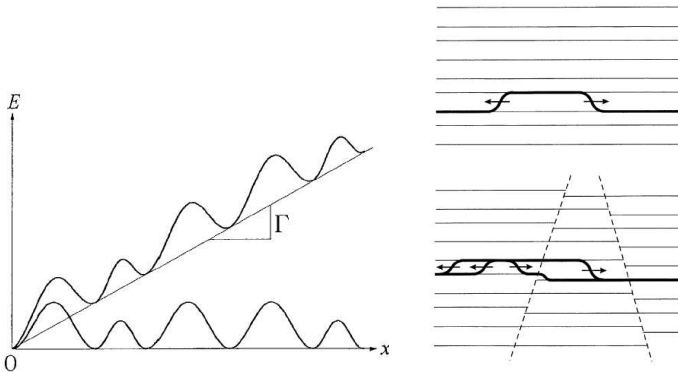


Figure 2.12: Peierls mechanism in a quasicrystal. Left: Peierls energy according to [66]. In addition to the quasiperiodic shape there is a linear contribution from the phason wall. The two scenarios correspond to different temperature (see text). Right: kink pair nucleation in a perfect (upper scenario) quasicrystalline lattice and in the presence of a phason wall (lower scenario) to explain the observed softening (see text).

The dislocations observed *in situ* moved in a viscous manner, keeping

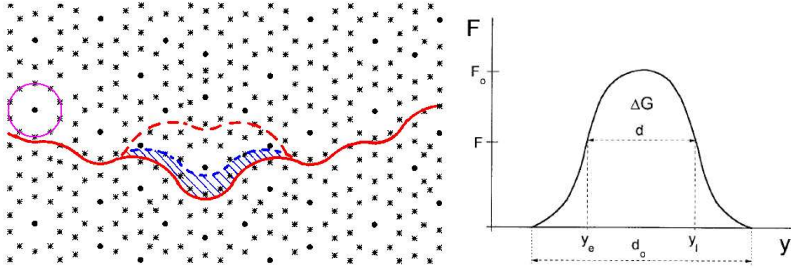


Figure 2.13: Cluster-friction mechanism [81]. Left: structure model of i-AlPdMn according to BOUDARD ET AL. [82] with a dislocation moving through an array of localized obstacles (see text). Right: force-distance profile of the interaction between the dislocation and an obstacle.

straight and parallel to the direction of a symmetry axis. This is reminiscent of observations in tetrahedrally coordinated covalent crystals and bcc metals, both of which are controlled by a Peierls mechanism. The nature of a Peierls mechanism in a quasicrystal has been discussed by TAKEUCHI ET AL. [66]. They proposed a Peierls potential like that of the upper curve in the left part of fig. 2.12. Similar to periodic lattices, the energy of a straight dislocation varies as a function of its position. However, this variation is quasiperiodic, with Peierls hills of various heights. In addition, the creation of the phason wall requires an additional dragging stress $\sigma_d = \Gamma/b$ manifesting in a positive slope of the energy curve. The critical stress required for dislocation motion becomes $\Gamma/b + \sigma_P$ where σ_P is the Peierls stress in the usual definition. The Peierls potential of a one-dimensional quasiperiodic chain was calculated in [83] and lead to a similar curve as in fig. 2.12.

At high temperatures, annealing of the phason wall should reduce the average slope of the Peierls potential to that of the lower curve in the left part of fig. 2.12. Hence, the internal stress is temperature-dependent, which has been confirmed by measurements in i-AlPdMn [66]. The measured activation enthalpy of 3-4 eV would then correspond to twice the kink formation energy like in a Peierls mechanism in a crystal.

In the picture of a Peierls mechanism the work softening is explained

in the following way [84]: before a phason wall is present dislocation motion occurs by kink-pair formation within the large Peierls valleys (right part of fig. 2.12, upper scenario) requiring a large activation enthalpy. The situation changes when phason walls have been created by moving dislocations. Then the kink-pair formation can always occur in the narrow spacings of the Peierls valleys and the necessary activation enthalpy is smaller (lower scenario). A quantitative discussion of this model can be found in [85].

A contrary mechanism is the *cluster friction mechanism* proposed by FEUERBACHER ET AL. [86] and MESSERSCHMIDT ET AL. [81]. From measurements of large activation enthalpies of 7 eV¹² or 80 $k_B T$ a diffusive nature of the deformation mechanism could be excluded¹³. More important, the activation volumes between $40b^3$ and $245b^3$ [88, 89] are too large for a Peierls mechanism.

FEUERBACHER ET AL. suggested that Mackay clusters, a frequent structure element in i-AlPdMn (according to BOUDARD ET AL.'s structure model [82]) would act as rate-controlling obstacles. Their extraordinary stability has been shown in STM investigations of cleavage surfaces [90]. The clusters were preserved because the cracks had circumvented them.

MESSERSCHMIDT ET AL. discussed the cluster-friction model in a more quantitative way by considering the clusters as weak obstacles [81]. In the left part of fig. 2.13 a dislocation moves through an array of obstacles in i-AlPdMn. We see a projection along a five-fold axis (the symbols * denote Al atoms, · denote Mn atoms). The clusters appear as circular arrangements of ten Mn atoms around a central Al atom. One of them is emphasized by a circle. The dislocation is first located in a stable position (solid line) around some clusters. One of them is overcome by thermal activation and the dislocation moves into a metastable position (dashed line). From there the dislocation moves to a second stable position behind the clusters (second solid line).

The overcoming can be viewed as a cutting of the obstacles near their equator hereby effectively reducing their density which explains the observed softening. MESSERSCHMIDT ET AL. estimated an upper bound for the activation area $V = ldb$ swept by the dislocation from

¹²In pure aluminum 1.5 eV is measured.

¹³Different values of 20 and 50 $k_B T$ were reported in [70, 87].

the stable to the metastable position. b is the modulus of the Burgers vector, d is the cluster diameter, and l the obstacle distance along the dislocations. b was obtained from [78], d and l can be determined from the structure. An upper bound of $0.16nm^3$ of V corresponding to $26b^3$ was calculated. The discrepancy to the measurements by one order of magnitude was explained by the assumption that always an array of obstacles would be overcome at a time. There is an analytic theory describing such a process [91] whose application made the estimation agree with the experimental observations.

d can also be found in the graph in the right part of fig. 2.13. Here, the force-distance profile of the interaction between the dislocation and the obstacle is displayed. y_e marks the stable equilibrium configuration in front of the obstacle and y_l the respective labile one behind. ΔG is the Gibbs free enthalpy of activation. Together with d it decreases with increasing shear stress.

In another paper [88] MESSERSCHMIDT ET AL. suggested a combination of the two competing models considering the arrangement of the clusters: a Peierls mechanism scaled up to the larger scale of the clusters.

At this point, we briefly summarize the properties of quasicrystal plasticity and dislocations:

- Quasicrystals are brittle at low temperatures and ductile at elevated temperatures. The brittle-to-ductile transition occurs at approximately 80% of the melting temperature.
- With increasing strain softening is observed. The strain accommodation parameter ζ decreases.
- Large values of both the activation enthalpy and the activation volume are observed.

2.5.3 Simulations

The first simulations of dislocations in quasicrystals have been performed by MIKULLA ET AL. [2, 3, 93, 94] in a 2D decagonal model system, the 2D binary tiling. It consists of the two Penrose rhombs but is not a Penrose tiling because it contains additional vertex configurations like the characteristic *ten-fold rings*. It is thermodynamically

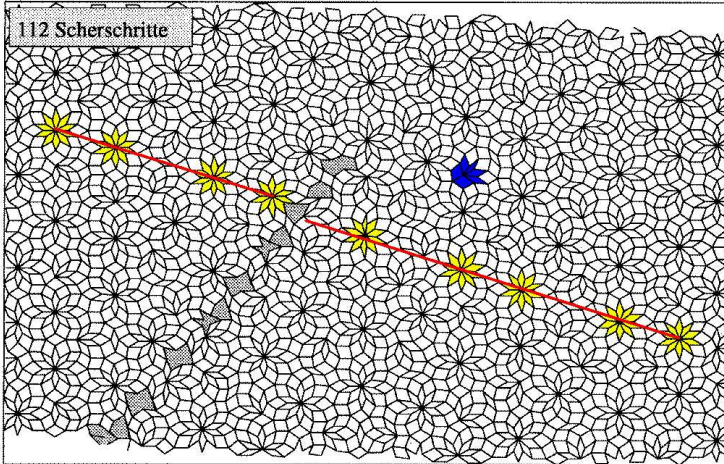


Figure 2.14: Dislocation in the 2D binary tiling [92].

stable with simple pair interactions [95, 96]. The extremely stable ten-fold rings are arranged on families of parallel lines.

In simulations at two temperatures (43% and 73% of the melting temperature, referred to as low- and high-temperature simulation) the nucleation of a dislocation dipole¹⁴ was observed. In the low temperature simulation the dislocations performed a glide motion along a close-packed direction (fig. 2.14) located between two lines with ten-fold rings. The associated slip can easily be identified from the discontinuity of these lines across the glide plane (red line). A phason wall is left behind manifesting itself by forbidden vertex configurations and (shaded) regions where no reconstruction of the tiles is possible. The glide motion was intermittent: incomplete ten-fold rings consisting of two thick and four thin rhombs acted as obstacles [97]. We denote them as *crowns*. One of them is drawn blue in fig. 2.14. A Burgers vector corresponding to the short diagonal of the thick rhomb was determined.

In the high temperature simulation also climb was observed. The dislocation avoided the crowns. As a consequence, a wider phason wall

¹⁴Because of the periodic boundary conditions that were applied.

was left behind which even broadened due to diffusion processes as the simulation continued. The ten-fold rings and the crowns can be viewed as analogues to the Mackay clusters in i-AlPdMn.

The Burgers vector corresponded to the short diagonal of the thick rhomb in the low temperature simulation and to the long diagonal of the thin rhomb in the high temperature case. This is at first surprising as it leads to a higher elastic energy $\propto b^{\parallel 2}$. The phason component b^\perp of the high-temperature Burgers vector is smaller, however. Due to the lower elastic constants at high temperatures, the dislocation can “afford” more elastic energy and benefit from a phason wall with lower energy. Both Burgers vectors are in accordance with minima of the Gamma surface [97].

In the course of both simulations the nucleation of secondary dislocations was observed. It always occurred on the phason wall. Dislocations were also observed in simulations of crack propagation at temperatures close to zero [93, 98]. They were emitted when the crack stopped in front of an obstacle due to stress concentrations at the crack tip.

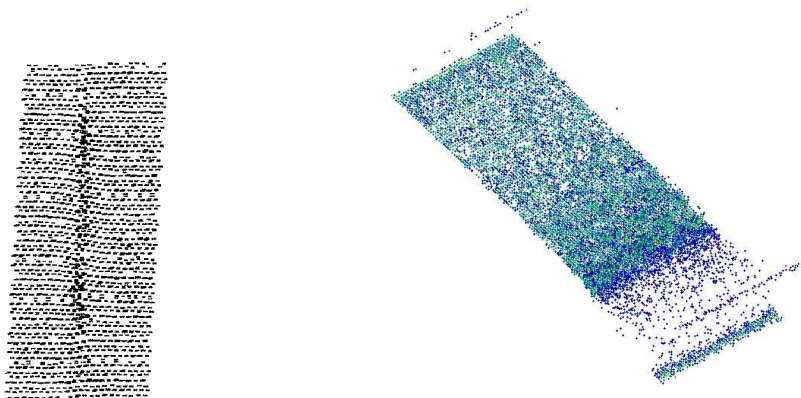


Figure 2.15: Simulations in the IBT at zero temperature. Left: projection parallel to the dislocation line (from [99]). Right: atoms with a large excess potential energy (color encoded) are plotted (from [100]).

DILGER ET AL. performed static shear simulations on an approximant of the IBT with 32,027 atoms at zero temperature [99]. They observed a dislocation dipole with Burgers vector parallel to a three-fold direction. The dislocations glided and left behind a phason wall where secondary dislocations nucleated in the course of the simulation. The left part of fig. 2.15 shows a projection of atoms parallel to the dislocation line ξ . The pair of dislocations can be seen.

SCHAAF ET AL. [100] observed a curved dislocation core. Their simulations of shear deformations at zero temperature were performed on a sample of 1.5 million atoms containing a partial edge dislocation constructed by applying a PN displacement field. The Burgers vector $\frac{1}{2}(\mathbf{g}_1 + \mathbf{g}_2)$ corresponded to a minimum of the Gamma surface of the structure.

In dislocation cores the bonds are severely distorted and every atom has a large potential energy E_{pot} . By only plotting atoms whose E_{pot} exceeds a given threshold, crystalline dislocation cores appear as narrow tubes [101] and bow-outs can be detected. In quasicrystals, this technique cannot be applied. The various local neighborhoods of the atoms lead to variations of the potential energy larger than the excess energy caused by the defect structures like a dislocation or a phason wall.

However, the excess energy of an atom can be calculated by comparison with the value from a defect-free reference configuration. *3D visualizations* (right part of fig. 2.15) of both the phason wall and the curved dislocation core are obtained. The authors concluded that the dislocation was pinned at obstacles in the sample [102].

We see that many experimental observations could be reproduced:

- At low temperatures the critical stresses for dislocation motion are very high and decrease with increasing temperature.
- The type of motion is different at low and high temperatures. Different Burgers vectors are observed.
- At high temperatures the phason wall broadens.
- Secondary dislocations nucleate much easier and always on the phason wall: the slip is localized.

The simulations also emphasize the important role of the phason wall.

Chapter 3

Molecular dynamics

Molecular dynamics (MD) is a method used to study a classical many-particle system. The particle trajectories¹ are integrated according to a specific law of interaction. From this microscopic information values for macroscopic thermodynamic observables are derived by means of statistical physics. For a detailed introduction to the field of MD see [103].

A classical system on which no external forces act is described by the *Hamiltonian equations of motion*

$$\dot{\mathbf{r}}^{(i)} = \frac{1}{m^{(i)}} \mathbf{p}^{(i)} \quad (3.1)$$

$$\dot{\mathbf{p}}^{(i)} = \mathbf{f}^{(i)} . \quad (3.2)$$

Its Hamiltonian is

$$H_0 = \sum_i \frac{\mathbf{p}^{(i)2}}{m^{(i)}} + \Phi(\mathbf{r}^{(1)}, \dots, \mathbf{r}^{(N)}) , \quad (3.3)$$

where Φ is the potential energy of the system. It depends on the coordinates $\mathbf{r}^{(i)}$, $i \in \{1, \dots, N\}$ of all N atoms. $\mathbf{p}^{(i)}$ is the momentum of the i -th atom.

¹In the following we are going to speak of atoms instead of particles. Of course, it is possible to simulate molecules, atom clusters, or even macromolecules like amino acids if only a suitable interaction law is used.

We have performed our MD simulations with the program IMD (ITAP molecular dynamics) [104, 105]². It was developed for the simulation of solids and was designed to run efficiently on both workstations and modern supercomputers (both with distributed and shared memory architecture).

This chapter starts with an introduction to statistical mechanics. Then we explain how to perform the numerical integration of the equations of motion. The force law we have used and its effective evaluation are presented in the following section. A discussion of boundary effects and a description of how various thermodynamical ensembles can be simulated conclude this chapter.

We will use the following abbreviations for sums:

$$\sum_i := \sum_{i=1}^N, \quad \sum_{i < j} := \sum_{i=1}^N \sum_{j=i+1}^N$$

For derivatives and tensor components we will use greek indices to avoid confusion with the latin indices used to denote the atom numbers.

3.1 Statistical Mechanics

In an MD simulation we calculate atom trajectories, i.e., the values of microscopical quantities, namely atom coordinates and momenta. In an experiment, however, only macroscopical observables (like temperature, pressure, etc.) can be measured. In order to compare the experimental and the MD results we need a bridge between the two pictures. This bridge is provided by the theory of *statistical mechanics*. It teaches us how to calculate macroscopic observables from microscopical quantities by a suitable averaging procedure.

The microscopical description of a many-atom system consisting of N atoms makes use of a $2dN$ -dimensional *phase space*. d is the dimension of the system. In the phase space the system corresponds to a point $\Gamma = (\mathbf{r}^{(1)}, \dots, \mathbf{r}^{(N)}, \mathbf{p}^{(1)}, \dots, \mathbf{p}^{(N)})$ and its evolution in time is described by $\Gamma(t)$. Every macroscopic variable has an instantaneous value

²See also www.itap.physik.uni-stuttgart.de/~imd

$A(t) = A(\Gamma(t))$ without physical relevance: every experiment takes a finite time, and only the *time average* $\langle A \rangle_{time}$ of a physical observable

$$\langle A \rangle_{time} = \langle A(\Gamma(t)) \rangle_{time} = \lim_{t_{obs} \rightarrow \infty} \frac{1}{t_{obs}} \int_0^{t_{obs}} A(\Gamma(t)) dt \quad (3.4)$$

is accessible. From an MD simulation we obtain an approximation A_{calc} of $\langle A \rangle_{time}$ by averaging over n_s time steps of a simulation:

$$A_{calc} = \frac{1}{n_s} \sum_{n=1}^{n_s} A(\Gamma(t)) \quad (3.5)$$

The evolution of the system corresponds to the motion of Γ with time. Often Γ is confined to a bounded region of the phase space specified by boundary conditions. These boundary conditions correspond to external macroscopic variables fixed to certain values. For example, in an isolated system the total energy is conserved to a value E_0 . The system then evolves on the hypersurface $E = E_0$.

We now define an *ensemble* as the set of all points in phase space compatible with the boundary conditions. The *phase space density* $\rho_{ens}(\Gamma)$ is defined such that $\rho_{ens}(\Gamma)d\Gamma$ is the probability of encountering the system within a phase space interval $[\Gamma, \Gamma + d\Gamma]$. Hence, $\rho_{ens}(\Gamma) > 0$ for all ensemble points, otherwise zero. Let us suppose that the system traverses all ensemble points during its time evolution in the thermodynamic limit corresponding to an infinitely long observation time. Such a system is called *ergodic*. We obtain the *ensemble average*

$$A_{ens} := \int \rho_{ens}(\Gamma) A(\Gamma) d\Gamma \quad (3.6)$$

where the integration extends over the whole phase space. This equation is the fundament of GIBBS' formulation of statistical mechanics. The above condition of ergodicity is equivalent to the statement that the time average and the ensemble average of a system are equal.

To make the difference of A_{calc} and A_{obs} as small as possible it is necessary that

- the simulation time is long enough to sample as many ensembles as possible

- the trajectories generate a correct $\rho_{ens}(\Gamma)$ ³
- the system does not evolve on orbits restricted to a finite region in phase space (for instance periodic orbits)

Calculation of thermodynamic observables

- The temperature T is derived with the help of the equipartition theorem [103]

$$\left\langle \sum_i \frac{\mathbf{p}^{(i)2}}{2m^{(i)}} \right\rangle = \frac{1}{2} k_B f T \quad (3.7)$$

where k_B is the Boltzmann constant and f is the number of degrees of freedom.

- The pressure can be calculated by making use of the virial theorem: The *virial*

$$W := \frac{1}{3} \sum_i \mathbf{r}^{(i)} \mathbf{f}^{(i)} = \frac{1}{3} \sum_{i < j} \mathbf{r}^{(ij)} \mathbf{f}^{(ij)} \quad (3.8)$$

describes the deviation of the function of state of a van-der-Waals gas from an ideal gas due to the interaction between the atoms. The rightmost expression follows from Newton's third law. It is independent of the choice of the origin and **must** be used in the case of periodic boundary conditions because there the origin is no longer defined. $\mathbf{r}^{(ij)} := \mathbf{r}^{(i)} - \mathbf{r}^{(j)}$ is the distance vector between the i -th and the j -th atom, $\mathbf{f}^{(ij)}$ is the force between them. To obtain the total pressure P its value in an ideal gas must be added:

$$P = \rho k_B T + \langle W \rangle \quad (3.9)$$

- The diffusion coefficient D can be calculated from

$$2dDt = \frac{1}{N} \langle (\mathbf{r}(t) - \mathbf{r}(0))^2 \rangle \quad (3.10)$$

³Errors in the trajectories itself are not significant if they disappear during the evaluation of eq. (3.5). Anyway, due to the chaotic nature of the system the concept of exact trajectories must be skipped.

where d is the dimension. It can be restricted to a direction parallel to the unit vector \mathbf{n} by calculating

$$2D_{\mathbf{n}}t = \frac{1}{N} \langle (\mathbf{n}(\mathbf{r}(t) - \mathbf{r}(0)))^2 \rangle \quad (3.11)$$

- According to [106] the stress tensor is

$$\sigma_{\alpha\beta} = \frac{1}{V} \left(\sum_i \frac{p_{\alpha}^{(i)} p_{\beta}^{(i)}}{m^{(i)}} + \sum_{i < j} \frac{\partial \Phi}{\partial r_{\alpha}^{(ij)}} r_{\beta}^{(ij)} \right) \quad (3.12)$$

where V is the system volume.

3.2 Integrators

Now we know how to calculate macroscopic observables from the atom trajectories. The latter are obtained from a numerical integration of the equations of motion (eqs. (3.1-3.2)) simultaneously for all atoms. The trajectories are calculated piecewise with a *time step* h . The values of $\mathbf{r}^{(i)}$ and $\mathbf{p}^{(i)}$ at $t + h$ only depend on the values at time t . An integration algorithm (*integrator* for short) describes how to perform the integration.

Any integrator can produce arbitrarily exact atom trajectories⁴ in the limit $h \rightarrow 0$. However, the simulation time $T = N_{steps}h$ with the number of time steps n_{steps} shall be as long as possible and a large h is preferred. Anyway, due to their chaotic nature there is no need for an exact determination of the trajectories. It is only important to sample the phase space as good as possible. In particular, the system should not be “caught” in a bounded region from which it cannot escape.

Our integrator shall allow a large time step h . It shall be time-centered (invariant under the transformation $t \rightarrow -t$) and symplectic⁵ because eqs. (3.1-3.2) have the same properties. Most important, it

⁴The total energy of a system following eqs. (3.1-3.2) is a conserved quantity except for numerical fluctuations. Hence, it can serve as a measure of the “exactness” of the trajectories.

⁵This means that the transformation $(\mathbf{r}, \mathbf{p})|_{(t)} \rightarrow (\mathbf{r}, \mathbf{p})|_{(t+h)}$ has a Jacobi determinant of one, i.e. that phase space is incompressible.

should be numerically efficient and easy to implement. In our simulations we have used a *leap-frog algorithm* [107]. It is derived from Taylor expansions of eqs. (3.1-3.2):

$$p^{(i)}(t + h/2) = p^{(i)}(t - h/2) + f^{(i)}(t)h \quad (3.13)$$

$$r^{(i)}(t + h) = r^{(i)}(t) + \frac{1}{m^{(i)}}p^{(i)}(t + h/2)h . \quad (3.14)$$

The coordinates $r^{(i)}$ are calculated at points in time $t, t + h, t + 2h, \dots$. The momenta are calculated at points in time shifted by $h/2$ which explains the name leap-frog algorithm.

3.3 Potential

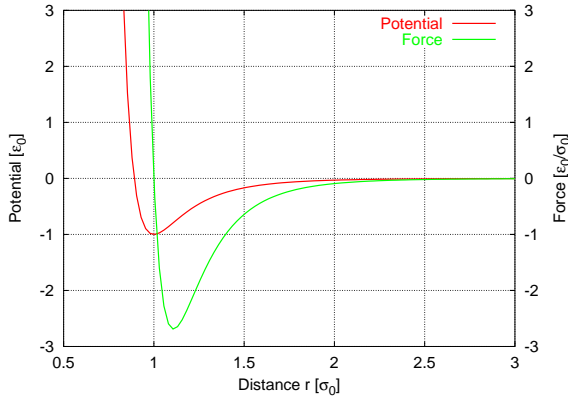


Figure 3.1: Lennard-Jones potential used in the simulation.

The physical properties of the simulated material are determined by the interaction between the atoms. Because we are mainly interested in a qualitative understanding of the reaction of our model quasicrystal to shear deformation we use a rather simple potential. For several materials there exist sophisticated potentials derived *ab initio*, i.e., without assumptions and parameters. This difficult task has not yet been undertaken for quasicrystals.

The potential energy of a system of N atoms can be expanded into a sum of pair, triplet, etc. interactions:

$$E_{pot} = \sum_i \phi_1(\mathbf{r}^{(i)}) + \sum_{i < j} \phi_2(\mathbf{r}^{(i)}, \mathbf{r}^{(j)}) \quad (3.15)$$

$$+ \sum_{i < j < k} \phi_3(\mathbf{r}^{(i)}, \mathbf{r}^{(j)}, \mathbf{r}^{(k)}) + \dots$$

In the following we only consider pair potentials $\phi^{(ij)} := \phi_2(\mathbf{r}^{(i)}, \mathbf{r}^{(j)})$. A spherically symmetric pair potential only depends on the interatomic distance $r^{(ij)} = |\mathbf{r}^{(ij)}|$. The potential energy becomes

$$E_{pot} = \sum_{i < j} \phi^{(ij)} \quad (3.16)$$

and the force acting on the i -th atom can be computed from the gradient

$$\mathbf{f}^{(i)} = -\nabla_{\mathbf{r}^{(i)}} E_{pot} \quad (3.17)$$

An example is the *Lennard-Jones potential* (fig. 3.1)

$$\phi_{LJ}(r) = e_0 \left(\left(\frac{s_0}{r} \right)^{12} - 2 \left(\frac{s_0}{r} \right)^6 \right) \quad (3.18)$$

which we have used in our simulations. It is most appropriate for spherically symmetric atoms without permanent dipoles like noble gases. The attractive term describes a van-der-Waals interaction due to induced dipoles. The repulsive term is derived empirically.

The potential has a minimum at $r = s_0$ of depth e_0 . These two parameters define a natural system of physical units which will be used in our simulations. The potential goes rapidly to zero for increasing r so that the potential can be truncated, i. e., set to zero for $r > r_{co}$. r_{co} is the *cut-off radius*. A typical choice is $r_{co} = 2.5s_0$. This reduces the computational effort which is proportional to r_{co}^3 (cf. sec. 3.4). To avoid a step at this point the whole potential is shifted by $\phi(r_{co})$.

3.4 Linked-cell method

From sec. 3.2 we know that for the calculation of the potential energy E_{pot} and the force $\mathbf{f}^{(i)}$ acting on the i -th atom the interaction $\mathbf{f}^{(ij)}$

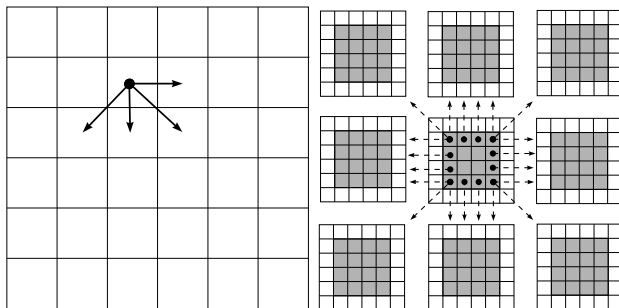


Figure 3.2: Left picture: Linked-cell method. The atoms are distributed into rectangular cells of diameter r_{co} . This allows an effective determination of neighbors (see text). Right picture: The linked-cell method can easily be parallelized by mapping the cell grid to a CPU grid (see text).

between the atoms must be computed. This has to be done in every time step and for every atom. An efficient method is desirable.

In principle, each of the N atoms interacts with every other atom, requiring a total number of $N(N - 1) = O(N^2)$ calculations in every time step. This is only tractable for very small systems. However, the Lennard-Jones potential of our simulations is zero for distances larger than the cut-off radius r_{co} . In other words, every atom only interacts with its *neighbors*, i.e., those atoms within a sphere of radius r_{co} . If we assume a constant average density of the atoms, the number of neighbors is also constant and the computational effort becomes linear in N . However, we have introduced a new problem: how can we find the neighbors of an atom? Unfortunately, the effort is quadratic in N , as well.

A neighbor search with an effort linear in N can be achieved with the implementation of a *linked-cell method* [108]. The simulation box is divided into cells of rectangular shape whose diameter is equal to r_{co} . The left part of fig. 3.2 illustrates this for the 2D case. The cell size guarantees that an atom only interacts with atoms in the same cell or in one the 8 (26 in 3D) neighboring cells. Furthermore, this number can

be reduced to 4 resp. 13 if Newton's third law *actio=reactio* is applied. The distribution of the atoms onto the cells must be updated after every time step because atoms might cross the cell boundaries.

A *parallelization* of this method is straightforward. The cell grid is mapped to a CPU grid (right part of fig. 3.2). Every CPU performs a simulation as described above. The only difference occurs in cells located at the boundaries between two CPUs. Two atoms on different CPUs can interact. To calculate their distance, their coordinates must be exchanged between the CPUs. Additionally, atom trajectories may cross CPU boundaries. In that case the atom must be moved from one CPU to another. The performance gain is considerable [104].

3.5 Boundaries

Contrary to a real material, in MD simulations a large portion of the atoms is located at the boundaries of the sample. These atoms have a different atomic neighborhood, for instance fewer nearest neighbors. As a consequence, a large ratio of boundary atoms to bulk atoms can drastically change the physical properties of a system. Although today (2002) the world record for MD simulations is $8.0 \cdot 10^9$ atoms [109], typical simulations are made with about 100,000 to one million atoms, corresponding to a ratio of about 3% to 6%.

Boundary effects can be suppressed by the implementation of specific *boundary conditions*. There are three main possibilities:

- *Free boundaries*: this simply means no special treatment of the boundaries. The sample corresponds to an atom cluster in vacuum which has the advantage of no artificial perturbation. However, the sample tends to expand due to the less repulsive forces acting on the boundary atoms. This leads to oscillations of the whole sample which may even lead to the evaporation of atoms from the boundary. It can also facilitate both the nucleation and motion of dislocations.
- *Fixed boundaries*: the motion of the atoms at the boundaries is restricted, either totally or only in some directions. A restriction to directions tangential to the boundaries avoids the oscillations described above. But this rather artificial boundary condition

has effects on the bulk properties as well, and they are hard to estimate⁶. Further problems arise from the inhomogeneous distribution of the system temperature⁷.

- *Periodic boundaries*: an infinitely extended sample containing no boundaries at all can be simulated. The simulation box is surrounded periodically by identical copies of itself as illustrated in fig. 3.3. It has the topology of a torus. An atom which leaves the central box re-enters through the opposite side. The distance between two atoms is no longer unique because of the copies. We always use the least possible distance (*minimum-image convention*). To avoid self-interaction the box diameter **must** be larger than $\frac{1}{2}r_{\text{co}}$. A disadvantage is the introduction of a new periodicity to the system, namely the box length L . The occurrence of long-wavelength fluctuations or long-wavelength phonons (greater than L) is inhibited. In the case of quasicrystals periodic approximants must be used. Due to the rational embedding of the strip phason defects appear (for example in the 3D Penrose tiling one finds adjacent rhombohedra of the same type and orientation). However, if the degree of the approximants is not too small, these effects should be negligible.

LEES AND EDWARDS [110] have modeled shear deformations with the help of periodic boundaries. The identical copies of the simulation box were displaced with respect to the central box (fig. 3.4) at a constant velocity γ . The origin is at the center of the central box. Because of the minimum image convention the atoms near the boundary of the central box are subject to shear forces from the atoms in the neighboring boxes.

⁶An example are elastic waves reflected at the fixed boundaries.

⁷In the case of a partial restriction a low-dimensional system is created where the temperature definition is different.

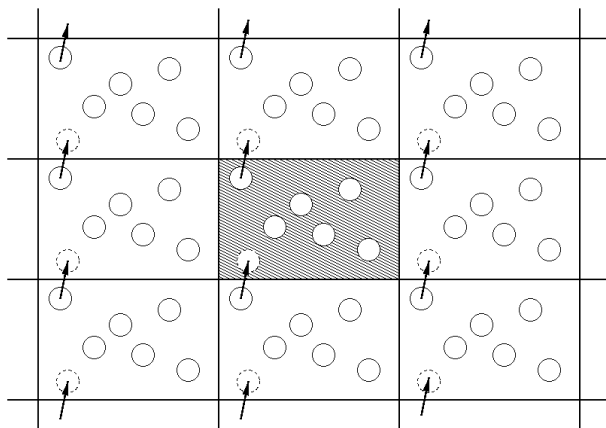


Figure 3.3: Periodic boundary conditions. The simulation box is surrounded by infinitely many copies of itself arranged periodically (see text).

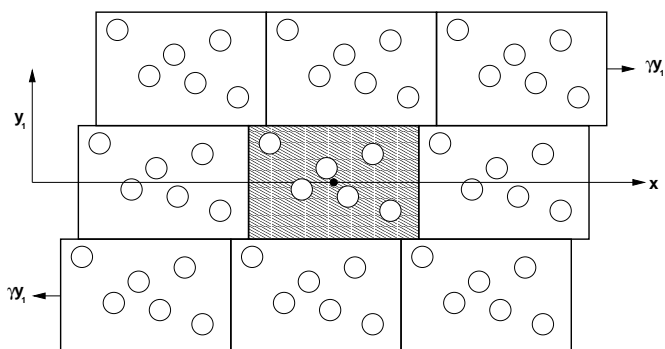


Figure 3.4: Lees-Edwards boundary conditions. By displacing the copies at a constant velocity γ a shear deformation can be simulated.

3.6 Ensembles

3.6.1 Microcanonical (NVE) ensemble

The integration described in sec. 3.2 conserves the total energy E , the number of atoms N and the volume V of the system. In statistical mechanics one speaks of a *microcanonical* or NVE ensemble. It corresponds to an experiment where these three values are fixed. In real experiments this situation occurs only seldom. Normally, the temperature T and the pressure P are given. To simulate such an experiment, a canonical or an isothermic-isobaric ensemble must be formulated. This is done by implementing a thermostat and a barostat. The corresponding algorithms are presented in the following sections. Two requirements are important:

- The algorithm shall not only provide the correct boundary conditions but also generate realistic trajectories.
- The algorithm should bring non-equilibrium systems back to an equilibrium state.

3.6.2 Canonical (NVT) ensemble

The second of the above conditions describes how a thermostat works. It exerts a generalized force to the system to drive its temperature T to the desired value T_0 . This force is proportional to the temperature difference $T - T_0$ so that an oscillator is obtained. The first of the above conditions states that the oscillations should not be too large. On the other hand they should also not be too small but rather correspond to the thermodynamical fluctuations of T .

In our simulations we have used a *Nosé-Hoover thermostat* [111, 112, 113, 114]. Like in the definition of a canonical ensemble in statistical mechanics a heat bath of infinite extension is coupled to the system. In

the equations of motion

$$\dot{\mathbf{r}}^{(i)} = \frac{1}{m^{(i)}} \mathbf{p}^{(i)}. \quad (3.19)$$

$$\dot{\mathbf{p}}^{(i)} = \mathbf{f}^{(i)} - \eta \mathbf{p}^{(i)} \quad (3.20)$$

$$\dot{\eta} = \frac{1}{Q} \left[\sum_i \frac{\mathbf{p}^{(i)2}}{m} - f N k_B T \right]. \quad (3.21)$$

the infinitely many degrees of freedom of the bath are expressed by one new variable η . The canonical phase space density is reproduced by eqs. (3.19 - 3.21).

η is proportional to the difference between current and desired temperature. The constant Q is the relaxation time of the heat bath. Its choice is crucial for the simulation. A value too small for Q leads to large, increasing oscillations and to numerical explosion of the system variables. A value too large, however, has the consequence that the system “creeps” very slowly to its equilibrium state which becomes almost unreachable. Q is determined empirically. As a first guess we can set $Q = \frac{1}{\omega_E}$, where ω_E is the *Einstein frequency* [103].

3.6.3 NPT ensemble

ANDERSEN [115] proposed a method to simulate an *isothermal-isobaric* NPT ensemble. His barostat to regulate the pressure P works quite similar to the Nosé-Hoover thermostat. Instead of the velocities the lengths are scaled to control the pressure, similar to a piston moving in a box. However, the scaling is done isotropically. The barostat is described by the following equations of motion follows (P_0 is the desired pressure and ζ the scaling variable):

$$\dot{\mathbf{r}}^{(i)} = \frac{1}{m^{(i)}} \mathbf{p}^{(i)} + \zeta \mathbf{r}^{(i)} \quad (3.22)$$

$$\dot{\mathbf{p}}^{(i)} = \mathbf{f}^{(i)} - (\zeta + \eta) \mathbf{p}^{(i)} \quad (3.23)$$

$$\dot{\eta} = \frac{1}{Q} \left[\sum_i \frac{\mathbf{p}^{(i)2}}{m} - f N k_B T \right] \quad (3.24)$$

$$\dot{\zeta} = \frac{1}{N k_B T W} (P - P_0) V. \quad (3.25)$$

The time constant W of the barostat can again be derived empirically and checked with the help of the pressure spectrum. While a wrong choice of Q "only" leads to a non-ergodic sampling of the phase space, a wrong choice of W has more drastic consequences. The sample as a whole starts to oscillate with increasing amplitude and finally "explodes".

3.6.4 MIC and GLOC relaxation algorithms

We now present two *relaxation algorithms* which do not correspond to a thermodynamical ensemble. Nevertheless, they are very useful if a state with a minimum potential energy is sought. For both methods the NVE integrator is modified and the potential energy converges to a minimum. Such a process is called *relaxation*.

For the *microconvergence (MIC)* algorithm [116] a Maxwell distribution of initial velocities is applied to the start configuration. Before an integration step is performed on a specific atom the scalar product $\mathbf{f}^{(i)} \cdot \mathbf{p}^{(i)}$ of its momentum vector and its force vector is calculated. If it is negative the motion is "out of the minimum" and $\mathbf{p}^{(i)}$ is set to zero. Otherwise the integration is performed as usual. As a consequence, kinetic energy that an atom has gained at the expense of a reduced potential energy is removed from the system. Both the total kinetic energy and the total potential energy decrease.

The MIC algorithm bears its name from the fact that the scalar product is evaluated on a microscopic level, i.e., for each atom individually. In the *global convergence (GLOC)* algorithm it is evaluated for all atoms together. A force and a momentum vector with all $3N$ entries of every atom are constructed. The sign of the generalized scalar product of those two vectors decides whether *all* momenta are set to zero or not. In most cases the GLOC algorithm brings the system to a "better" minimum than the MIC algorithm in the sense that the latter tends to freeze the system in a metastable state.

3.7 Non-equilibrium molecular dynamics

Equilibrium statistical mechanics is a well developed theory. The fundamental rules have been known since the beginning of the 20th century.

In the 1950s computer simulations of liquids began to have an impact on this field. MD simulations were used to simulate transport processes like diffusion, heat transfer, or shear flow. In these equilibrium simulations the fluctuations of a generalized flux (in the above examples flow of matter, heat, or shear stress) were measured. KUBO showed that from the knowledge of these *equilibrium fluctuations* the corresponding transport coefficients (diffusion constant, heat conductivity, shear viscosity) could be calculated [117]. We consider the example of the shear viscosity $\eta := -P_{xy}/\gamma$ where P_{xy} is the shear stress and γ is the (shear) strain rate. In the limit of small γ it can be calculated from the *Kubo relation*

$$\eta = \frac{V}{k_B T} \int_0^\infty ds \langle P_{xy}(0) P_{xy}(s) \rangle \quad (3.26)$$

where T is the absolute temperature, k_B is Boltzmann's constant and V the system volume. The angular brackets denote an **equilibrium** ensemble average. Eq. (3.26) was first applied by ALDER AND WAINWRIGHT [118].

The determination of transport coefficients from equilibrium MD simulations is computationally expensive and leads to poor signal-to-noise ratios. Furthermore, it is restricted to linear transport coefficients. HOOVER AND ASHURST [119] presented an alternative approach which simulates the transport process directly. This inevitably leads to a non-equilibrium system and the simulation method is called *non-equilibrium molecular dynamics (NEMD)*. Such a system can be modeled as an equilibrium system perturbed by an external field F_e appearing **explicitly** in the equations of motions. The field performs work on the system and prevents it from returning to equilibrium. With this work a dissipative flux is associated. It can be shown that the adiabatic response of an arbitrary phase variable B is a linear function of the external field. In the frame of this *linear response theory* one obtains a linear constitutive relation

$$L = \lim_{F_e \rightarrow 0} \lim_{t \rightarrow \infty} \frac{\langle B(t) \rangle}{F_e} \quad (3.27)$$

where L is the transport coefficient.

The use of a thermostat is necessary because otherwise the work done on the system would be continuously transformed into heat and no steady state could be achieved (in eq. (3.27) the limit $t \rightarrow \infty$ would not exist).

In the case of shear viscosity a Couette flow is modeled. Such a simulation must be performed with periodic boundary conditions, in particular Lees-Edwards boundary conditions. We have already seen that with their help a *boundary-driven shear* or *Couette flow* can be modeled. This method has certain drawbacks, however. For instance, as the shear rate does not occur in the equations of motions, linear response theory cannot be applied to connect the simulation results to, for instance, the Kubo relation.

It is better to modify the equations of motions to model a shear flow. The following algorithm has first been proposed by HOOVER [120, 121]. His algorithm is called *synthetic* because of the artificial modification of Newton's equation of motion. Similar to the expression for the stress tensor (eq. (3.12)) we model shear flow with a deformation. Instead of the strain $\varepsilon_{\alpha\beta}$ we use the non-symmetric deformation tensor $\partial_\alpha u_\beta$. The change in the system energy is

$$\delta E_{\text{tot}} = \sigma_{\alpha\beta} \delta \partial_\alpha u_\beta \quad (3.28)$$

which yields an expression for the energy dissipation rate

$$\dot{E}_{\text{tot}} = \sigma_{\alpha\beta} \delta \partial_\alpha \dot{u}_\beta = \frac{d}{dt} \left(\sum_i r_\alpha^{(i)} p_\beta^{(i)} \partial_\alpha u_\beta \right) . \quad (3.29)$$

HOOVER called the expression $\sigma_{\alpha\beta} \delta \partial_\alpha u_\beta$ *Doll's tensor*, a fantasy name. For small Reynolds numbers a replacement of the deformation gradient with the velocity gradient leads to the same descriptions. From now on we will describe the velocity gradient with $\sigma_{\alpha\beta} \delta \partial_\alpha u_\beta$. From that follows the *Doll's Hamiltonian*

$$H_{\text{Doll's}} = H_0 + \sum_i r_\alpha^{(i)} p_\beta^{(i)} \partial_\alpha \dot{u}_\beta \quad (3.30)$$

with H_0 from eq. (3.3). The corresponding Hamiltonian equations lead to results in agreement with linear response theory after a transposition of indices [122, 123]. Because of this transposition they are called *SLLOD* (the reverse of "DOLL's") equations⁸:

$$\dot{\mathbf{r}}^{(i)} = \frac{1}{m^{(i)}} \mathbf{p}^{(i)} + r_\beta^{(i)} \partial_\beta \dot{u}_\alpha \quad (3.31)$$

$$\dot{\mathbf{p}}^{(i)} = \mathbf{f}^{(i)} - p_\beta^{(i)} \partial_\beta \dot{u}_\alpha . \quad (3.32)$$

⁸They can no longer be derived from a Hamiltonian.

In the case of a constant velocity they reduce to Newton's equations of motion. The SLLOD equations must be solved together with Lees-Edwards boundary conditions. The neighboring cells must be sheared at the same rate.

A shear deformation is modeled with a spatially linear velocity gradient. The algorithm developed so far is suitable for the simulation of both fluids and solids. In solids one hardly expects deviations from a spatially linear velocity gradient, except at the onset of plastic deformation. Also, the use of a Nosé-Hoover thermostat can be justified because at elevated temperature the atoms vibrate around their equilibrium position even in the presence of external stresses. The purpose of the thermostat is two-fold: besides simulating a canonical ensemble it must remove the dissipated heat from the system. The temperature must be calculated from the atom momenta relative to the shear flow.

MIKULLA ET AL. have used the SLLOD equations in combination with a Nosé-Hoover thermostat and Lees-Edwards boundaries to simulate shear deformation on 2D model quasicrystals together with periodic boundaries. We have applied the same technique for simulations on a 3D model quasicrystal.

Chapter 4

Visualization

The MD simulations described in this thesis were performed on samples containing 10^5 - 10^6 atoms. It is impossible to analyze the particle trajectories to detect defects in the structure. Instead, suitable methods for their visualization are required. These methods are applied to a simulation snapshot which has been written to a hard disk. Such a snapshot contains all particle coordinates and velocities.

In a 2D system the dislocations can be identified by vision in a simple plot of all the atoms (cf. fig. 2.14). In 3D systems we encounter difficulties. If the atoms are projected onto a plane, they always obscure each other so that dislocations in the bulk either cannot be seen or information about their shape is lost due to the projection.

Displacement field

An easy method to investigate defect structures is the displacement field $\mathbf{u}(\mathbf{x})$, defined in eq. (A.2). It describes the deviation of the atom positions with respect to the perfect reference configuration without defects. It is useful to visualize the component of \mathbf{u} parallel to the Burgers vector as a function of the two coordinates which span the glide plane.

The displacement field of a PN dislocation with Burgers vector $\mathbf{b} = \mathbf{e}_x$ and line direction $\boldsymbol{\xi} = \mathbf{e}_y$ is $u_x = b/2 + b/\pi \arctan((x - x_0)/\zeta)$, and $u_y = u_z = 0$. $u_x(x, y)$ is visualized in the left part of fig. 4.1. The

surface has an arcus tangent shape translated parallel to the y -direction. The position of the dislocation core is $x_0 = u_x^{-1}(b/2)$, indicated by the blue line. In the general case of a curved dislocation it depends on y : $x_0 = x_0(y)$. The phason wall accompanying each quasicrystalline dislocation would correspond to the region where $u_x = \text{const} = b$. In our simulations we have always observed thermal vibration of the atoms. It becomes difficult to determine the exact core position, especially at high temperatures.

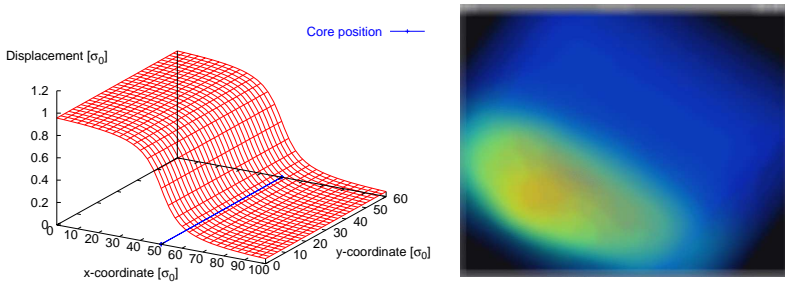


Figure 4.1: Visualization of the displacement field and the kinetic energy. Left: displacement field of a PN dislocation and position of the dislocation core (see text). Right: volume visualization of a dislocation loop and the phason wall inside. Blue colors denote low, red colors denote high kinetic energy.

Potential and kinetic energy

To visualize defect structures in the bulk directly it is sensible to only visualize selected atoms, namely those belonging to the defect. The distortion of the bonds of such atoms¹ increases their potential energy so that they can be identified and plotted (cf. the discussion of fig. 2.15 in sec. 2.5.3). This technique has proven useful at low temperatures. At higher temperatures however, thermal vibration also leads to bond distortions so that many other atoms also become plotted.

¹Again, these bonds connect nearest neighbors and must be distinguished from bonds in a chemical definition.

Defect structures can alternatively be detected by their large kinetic energy. With the help of a volume visualization software developed by SCHULZE-DÖBOLD [124] pictures like the right part of fig. 4.1 were obtained from a simulation at zero temperature. The phason wall and the pair of dislocations appear as diffuse regions. In an animation made from a series of snapshots the emission of sound waves could be observed. Again, this technique cannot be applied in the case of elevated temperatures. The kinetic energy of the atoms is too large to resolve the defect structures.

Retiling visualization

We have developed a visualization method based directly on the distortion of the bonds within the dislocation core and the phason wall. This distortion is analyzed for every bond and for every tile. The structure is being *retiled* from a snapshot, i.e. the bonds resp. the tiles are redrawn everywhere except for regions where they have been distorted too much.

The bonds between the atoms at the corners of the tiles correspond to the tile edges and are described by a vector² of length $2.0\sigma_0$. It is oriented parallel to one of the vectors pointing from the center of an icosahedron to its vertices (eq. (1.3)). The geometrically constructed start configuration without any defects like dislocations serves as a *reference configuration*. From it we obtain a list of all bonds in the structure. In this bond list the following information is stored for every bond: the numbers of the two atoms it connects and its orientation with respect to a fixed coordinate system. It is sorted according to the tiles. This means that the first twelve bonds of the list correspond to the first prolate atom and so forth, then follow the oblate rhombohedra, and finally the rhombic dodecahedra which have twenty-four bonds.

We calculate the current bond vector from the spatial coordinates of the corner atoms in a given snapshot of the simulation. Then we compare it to the original bond vector and determine the status of the bond. A bond is *broken* if either its length l differs largely from the ideal value of 2.0 or the angular deviation ϕ from the particular orientation is too large. Otherwise it is *intact*. The decision is made with two threshold values l_{max} and ϕ_{max} . Fig. 4.2 (left part) exemplifies this

²Its arbitrary orientation has no physical meaning.

visualization technique in a sample containing a dislocation dipole. The intact bonds are drawn black and an almost planar region without such bonds corresponds to the phason wall. It is bounded by the pair of dislocations. In a second step we have determined new bonds across the phason wall (red). Therefore, **only** the spatial coordinates of the atoms in the vicinity of the phason wall were used. Burgers circuits are now possible.

The threshold values l_{max} and ϕ_{max} must be chosen with care. If they are too small, too many bonds are detected as broken, especially in simulations at high temperature. There, elastic excitations like sound waves lead to temporarily broken bonds whose visualization might obscure the defect structures. On the other hand, a value too small might lead to too many intact bonds so that we would underestimate the extension of the phason wall. Reasonable threshold values follow from geometrical considerations: for instance should bonds be considered broken as soon as the value of their displacement exceeds half of the Burgers vector modulus.

An intuitive visualization is obtained by plotting the tiles instead of the bonds. Broken and intact tiles are defined rather similar as in the case of bonds. Every tile contains a certain number of bonds. We define that it is broken if the ratio of its broken to its intact bonds exceeds a threshold number. Otherwise it is intact. Plots of the broken tiles like the right part of fig. 4.2 show the phason wall and the dislocation core at its right end. Different colors denote different types of tiles: the prolate and oblate rhombohedra are blue resp. green while the rhombic dodecahedra are red.

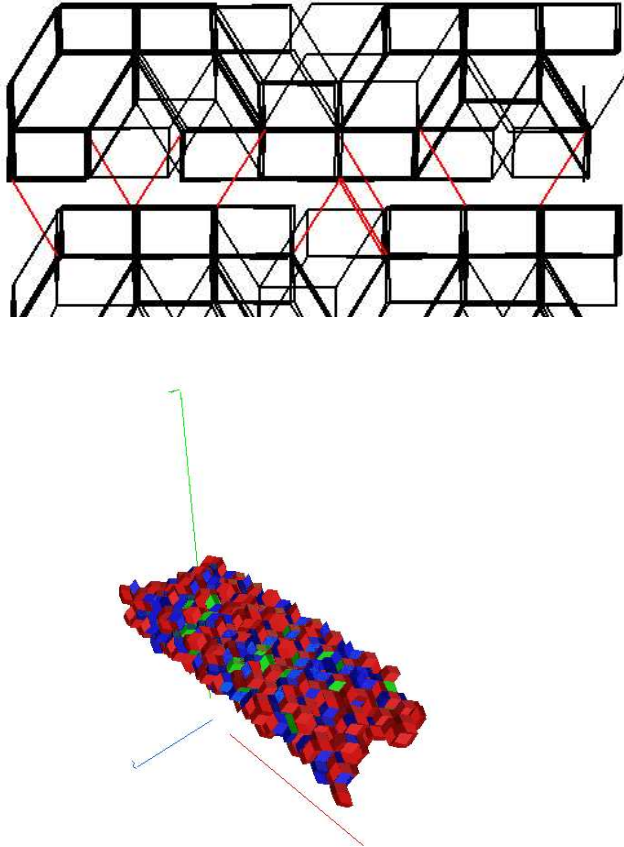


Figure 4.2: Tile and bond visualization. Top: intact bonds (black) are plotted. The phason wall appears as a region without bonds. In a second step, new bonds across the phason wall are determined (red). Bottom: the broken tiles form the phason wall and the dislocation core at its right end.

Chapter 5

Results of the simulations

5.1 Overview

5.1.1 Configurations used in the simulations

We have simulated shear experiments on samples of the IBT. Approximants were used whose edges were parallel to two-fold directions and spanned a Cartesian coordinate system. The approximants also served as reference configurations for the visualization.

We constructed a 7/6-7/6-4/3- and a 7/6-7/6-6/5-approximant with 222,160, resp. 581,612 atoms. We refer to them as the **small** and the **large** sample. In both samples the lengths in x - and z -direction were $L_x = L_z = 98.80\sigma_0$. The length in y -direction was $L_y = 23.32\sigma_0$ in the small sample and $L_y = 61.06\sigma_0$ in the large sample.

For the atomic interactions a Lennard-Jones potential (eq. (3.18)) was used. There are three different interactions: between two small atoms (SS), two large atoms (LL), and one small and one large atom (SL). Different potential parameters were used for them, as listed in tab. 5.1 (they are the same as in [99, 100, 102]). The minimum positions were chosen to lead to the lowest possible potential energy of the structure and roughly correspond to average nearest-neighbor distances [125].

σ_0 is the unit length and corresponds to one half of the edge length of a rhombohedron. ε_0 is the unit energy. We measure all physical quantities in units of σ_0 and ε_0 . For example the temperature unit is ε_0 and the pressure unit is ε_0/σ_0^3 , etc. Our time unit will be denoted by t_{MD} (MD time). It is related to "real" time t by $t_{MD} = (\varepsilon_0/m\sigma_0^2)^{1/2} t$ where m is the mass of an atom. We set $m = 1$ for both small and large atoms.

Atom pair	Pos. of minimum s_0	Depth of minimum e_0
SS	1.054 σ_0	1.0 ε_0
SL	1.230 σ_0	2.0 ε_0
LL	1.204 σ_0	1.0 ε_0

Table 5.1: Lennard-Jones potential parameters for the interactions between the two types of atoms.

5.1.2 Schedule of a shear simulation

Before the actual shear simulation the sample had to be prepared, i.e., relaxed and then equilibrated to the simulation pressure and temperature. This involved the following steps:

1. **Equilibration in the NPT ensemble:** the sample was relaxed several 10^3 time steps with the GLOC method. Then an equilibration in the NPT ensemble was performed to bring the system volume V and its temperature T to the desired values. V was chosen such that the simulation pressure became $p = 1.04\varepsilon_0/\sigma_0^3$. This equilibration typically took several 10^4 time steps. To guarantee the stability of the sample with the used values of p and T their fluctuations were observed over a much longer time¹. In the case of melting these fluctuations would diverge.
2. **Equilibration in the NVT ensemble:** the purpose of this equilibration was to get rid of the volume oscillations originating from the NPT equilibration. It usually took 10^4 time steps.

¹To reduce computational costs this was done on a small test system.

3. **Shear simulation in the SLLOD ensemble:** a homogeneous shear deformation with constant shear rate $\dot{\epsilon}$ was applied to the sample. It corresponded to a displacement velocity field $\dot{\mathbf{u}} = (\dot{\epsilon}y, 0, 0)$. Snapshots² were written to disk every 10^4 time steps. When plastic deformation was observed the simulation was restarted from the latest snapshot and further snapshots were written at much shorter intervals. They were used for a detailed microscopical analysis.

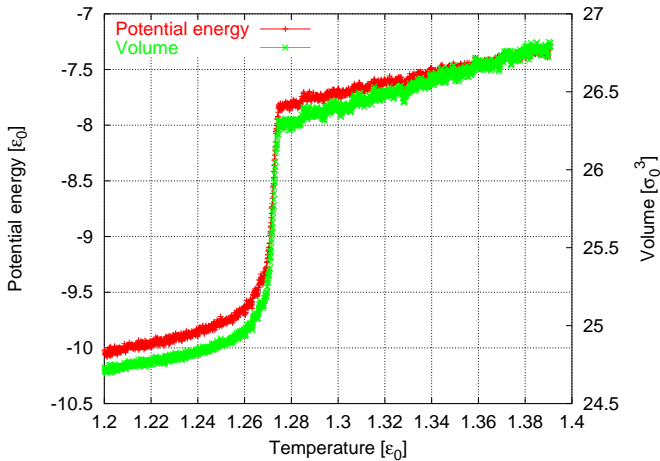


Figure 5.1: Heating simulation at constant pressure $1.04 \epsilon_0/\sigma_0^3$. The increase of both potential energy (red) and volume (green) indicate a first-order phase transition to the liquid state at the melting temperature $T_m = 1.27\epsilon_0$.

Additionally, a heating simulation was performed to determine the melting temperature T_m . The result is displayed in fig. 5.1 where both the potential energy and the volume (red and green curve, resp.) are plotted as a function of temperature T . Their sudden increase at $T_m = 1.27\epsilon_0$ indicates a first-order phase transition to the liquid state which is confirmed from the pair distribution function of the sample at $T > T_m$.

²The size of a snapshot was approximately 50 MB.

5.2 Simulation of a perfect sample

In a first simulation series we started from a perfect quasicrystalline structure. It was sheared at a rate of $\dot{\epsilon} = 10^{-3}t_{\text{MD}}$ at various temperatures. The pressure was set to $p = 1.04\epsilon_0/\sigma_0^3$. Periodic boundary conditions were applied in all directions. Therefore we expected the nucleation of a dislocation loop at a critical shear strain ϵ_c , its expansion, and turning into a dislocation dipole. The corresponding shear stress should drive the two dislocations apart until they recombine with their images in the neighboring copy of the simulation cell. The temperature ranged from $0.01\epsilon_0$ to $1.05\epsilon_0$ with a step width of $0.15\epsilon_0$. This corresponds to values from 0.5% to 83% of the melting temperature T_m .

5.2.1 Macroscopic values

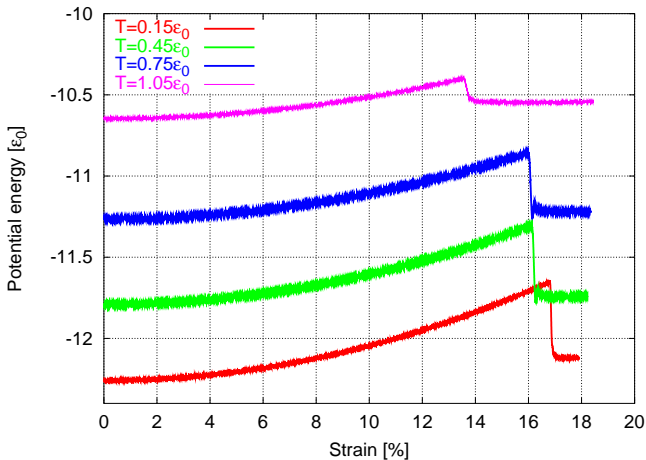


Figure 5.2: Potential energy as a function of strain at various temperatures (see text).

In fig. 5.2 the potential energies for $T = 0.15\epsilon_0$ (red curve), $T = 0.45\epsilon_0$ (green curve), $T = 0.75\epsilon_0$ (blue curve), and $T = 1.05\epsilon_0$ (magenta

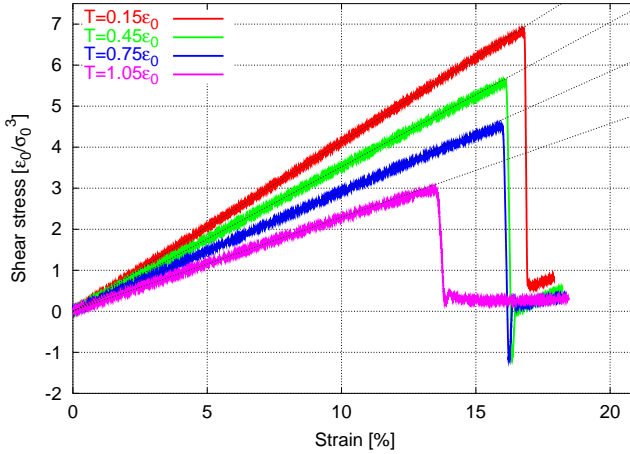


Figure 5.3: Stress-strain curves at various temperatures. The shear modulus μ was determined from a linear fit (dashed lines).

T [ε_0]	T/T_m [%]	μ [ε_0/σ_0^3]	ε_c [%]	σ_c [ε_0/σ_0^3]
0.01	0.7	43.0	16.9	7.1
0.15	12	42.5	16.8	7.1
0.3	24	39.3	16.7	6.6
0.45	35	37.1	16.6	6.1
0.6	47	34.4	16.3	5.7
0.75	59	28.1	16.1	5.3
0.9	71	25.2	15.4	4.9
1.05	83	23.4	13.9	4.5
Static sim. ($T = 0K$) [99]		33.3	14.8	4.7

Table 5.2: Elastic constants and critical strains and stresses as a function of temperature.

curve) are plotted as a function of strain³. The curves show at first a quadratic behavior corresponding to an elastic regime in the stress-strain curves up to a critical strain $\varepsilon_c = \varepsilon_c(T)$.

In fig. 5.3 the stress-strain curves for the same temperatures are displayed. For small strain the dependence of the stress was linear as indicated by the dashed lines. From their slope the shear modulus $\mu = \mu(T)$ was determined. For strains immediately below ε_c the material softens, i.e. the stresses are less than $\mu\varepsilon$. Such a behavior is caused by the increasing influence of second-nearest neighbors. The shear moduli $\mu(T)$ are listed in tab. 5.2. They decrease with increasing temperature.

Above ε_c a sudden drop of both the potential energies and the stresses indicates the onset of plastic deformation. $\varepsilon_c = \varepsilon_c(T)$ decreases with increasing temperature. Indeed, a dislocation loop has been created as we will see in sec. 5.2.2. The values of ε_c and of the critical stresses σ_c can also be found in tab. 5.2. σ_c ranges between approximately $\mu/7$ and $\mu/6$. These values are almost as large as the theoretical shear strength σ_{th} (cf. sec. 2.1). This can be justified with an estimation given in app. B. In [99] the critical stress was lower because the nucleation of the loop was facilitated by removing a row of atoms. In experiments where dislocation loops were created by nano-indentation in various materials comparable values of the critical stress have been observed [126].

After the onset of plastic deformation the stresses decrease to zero (and even to negative values). A decrease was expected because the moving dislocations introduced plastic strain reducing the total strain and stress. After their glide through the whole sample they recombined causing a slip of the two halves by b , the modulus of the Burgers vector \mathbf{b} . However, the total shear displacement at ε_c was much larger than b and we would expect that finite stress remained.

We attribute the decrease to zero to a failure of the sample along the glide plane after the recombination of the dislocations. After that, the two halves simply slipped as a whole, hereby removing all strain and stress from the sample. We explain the failure by a partial amorphization of the structure within a zone of small thickness parallel to the glide plane. Here, the structure was weakened by the phason wall

³Note that the strain is proportional to the simulation time due to the constant shear rate.

created by the moving dislocations.

Total amorphization of the sample can be excluded for two reasons. On the one hand, a continuation of the shear simulation to higher strains shows again a linear stress-strain dependence with almost the same slope as before. A totally amorphous sample would show a lower shear modulus. On the other hand the pair distribution function still consists of relatively narrow peaks⁴. In the case of an amorphous structures one would instead see very broad peaks. Indeed such a graph can be seen if we restrict the pair distribution function to a narrow region around the glide plane.

The hydrostatic pressure (fig. 5.4) also shows a quadratic increase with shear strain in the elastic regime and a drop at the onset of plastic deformation. This is caused by the non-symmetry of the distortion tensor ($\beta_{xy} > 0$, $\beta_{yx} = 0$) which would lead to a rotation of the sample. However, rotation is inhibited by the periodic boundaries. The result is a torque which leads to stresses normal to the glide plane and to the observed hydrostatic pressure.

5.2.2 Microscopic analysis

Retiling visualizations

For a microscopical analysis we turn to retiling visualizations of snapshots which were written to disk immediately after the drop of the stress-strain curves. Three of them are shown in the left column of fig. 5.5. We have plotted the broken tiles. In the right column the situation is sketched schematically. In the uppermost row we see an embryonal loop which encloses a phason wall. It has nucleated on a two-fold glide plane located between two atomic planes separated either by the largest or the second-largest possible distance. These distances are $0.65\sigma_0$ or $0.50\sigma_0$, respectively. Such a loop has a closed dislocation line of circular shape with a radius r . It contains edge- and screw-like components because the line direction ξ varies along the loop. r increases rapidly (middle row). As soon as it exceeds $L_y/2$ the screw-like segments annihilate. From the pictures in the lowest row we can see that indeed a dislocation dipole has been generated: the two remaining edge-like

⁴The peaks become more broadened with increasing temperature because of thermal vibration.

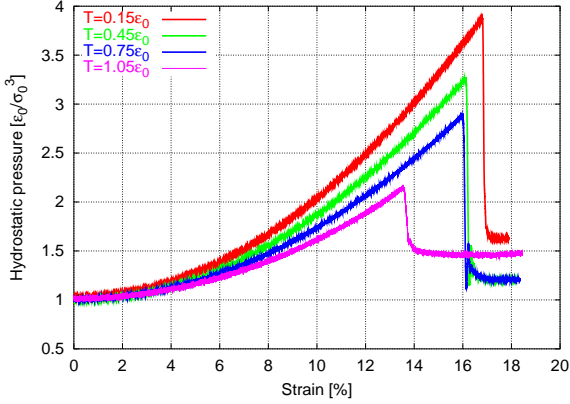


Figure 5.4: The hydrostatic pressure increases quadratically with shear strain. The reason is a torque as a result of the non-symmetric strain tensor (see text).

segments are no longer connected and have a straight shape⁵. There is a phason wall between the two dislocation which extends across the whole sample in y -direction.

The nucleation occurred at arbitrary locations on the glide planes described above because of the periodic boundaries applied in all directions. The nucleation was caused by a vibrational mode that had become unstable under the acting shear stress. The critical stresses for its creation were very large (cf. app. B) because they had to act against the line tension force. With the annihilation of the screw segments this force becomes zero and the two edge dislocations are accelerated. Depending on the temperature, their velocities are around 10 to 12 σ_0/t_{MD} . This corresponds to approximately 75% of the velocity of shear wave velocity $v_{sw} = \sqrt{\mu/\rho_m}$ where ρ_m is the mass density.

⁵We have drawn the loop as a closed contour along which \mathbf{b} is constant. From that follows that both dislocations have the same \mathbf{b} but $\boldsymbol{\xi}$ point into different directions. We use a more plausible description by assigning the same $\boldsymbol{\xi}$ to both dislocations but Burgers vectors of different sign.

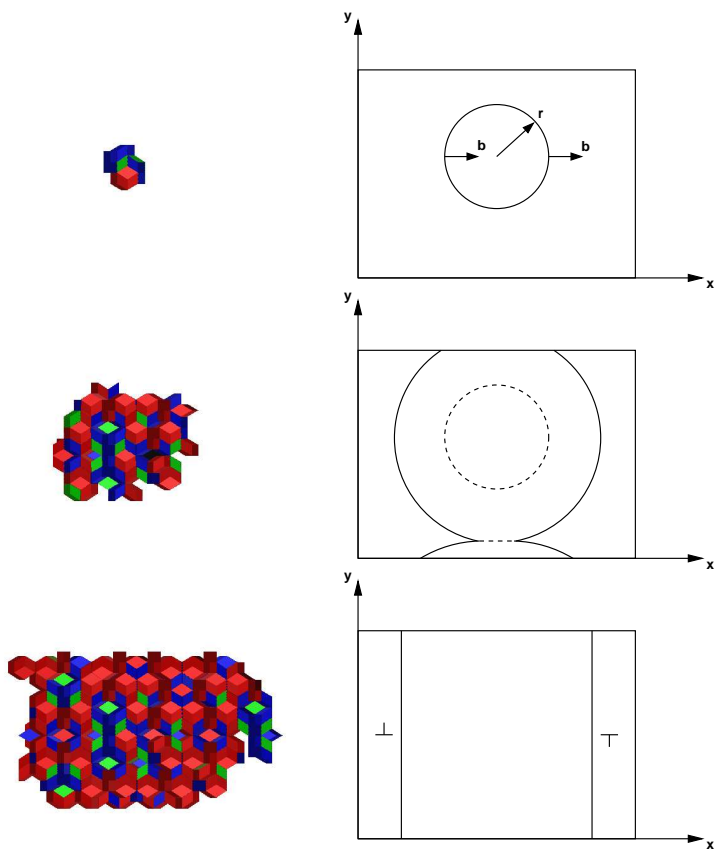


Figure 5.5: Nucleation of a dislocation loop. An embryonal loop can be seen (upper row) which rapidly increases (middle row). At a loop radius of $L_y/2$ the loop annihilates with itself and turns into two edge dislocations of opposite sign.

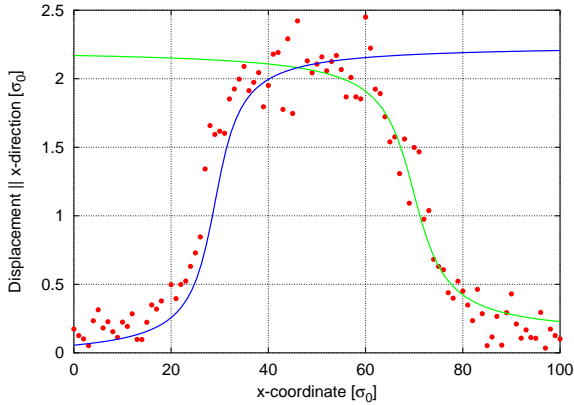


Figure 5.6: Displacement field of the dislocation dipole averaged into the dislocation line direction (red dots). Two arcs tangents have been fitted to the data (green and blue line).

Displacement field

Fig. 5.6 shows the displacement field calculated from a snapshot where the loop had already turned into a pair of edge dislocations. The values (red dots) are averaged along the y -direction. Two arcs tangents of different sign (green and blue line) can be fitted to the data: the dipole is a pair of two PN dislocations. We conclude a Burgers vector modulus $b \approx 2.1\sigma_0$. The widths are $\zeta = 4.9\sigma_0$ which is considerably larger than the value 1.5 for a PN dislocation.

Burgers circuits

Fig. 5.7 shows retiling visualizations of a snapshot where the dislocation dipole is already present. In the lower picture material coordinates are used so that all bonds were classified as intact. In the upper picture where we used spatial coordinates the phason wall appears as an empty region. Several new bonds which traverse the phason wall could be determined. Two closed Burgers circuits are shown (red lines, the yellow sphere indicates the atom at the start resp. at the end of the cir-

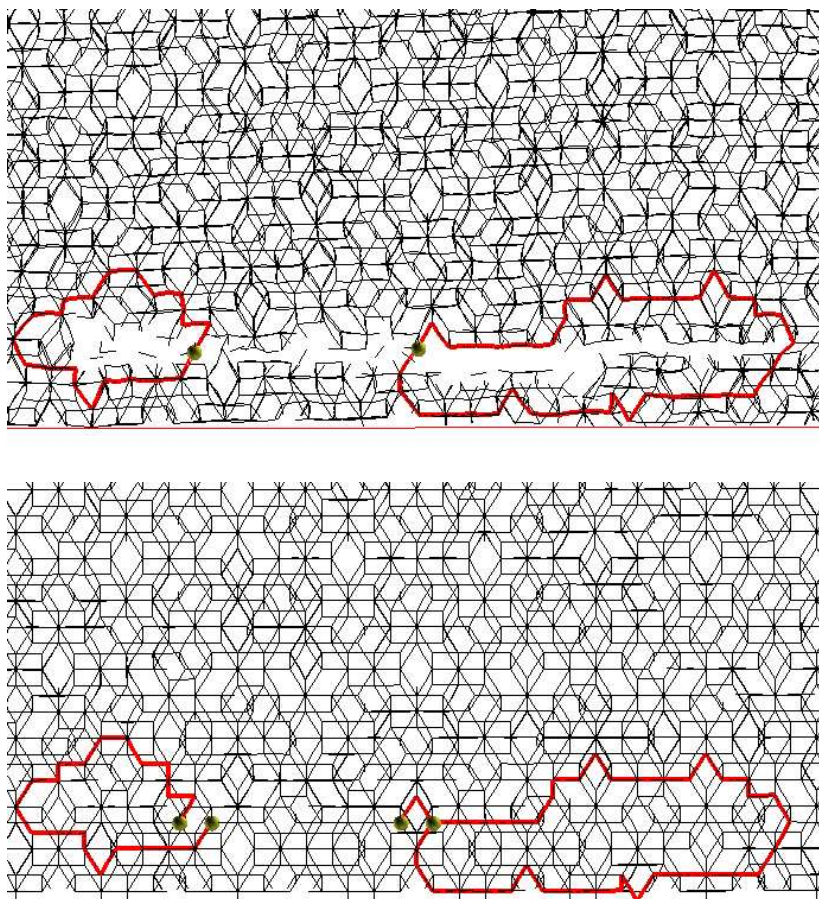


Figure 5.7: Retiled configurations (upper picture: spatial coordinates, lower picture: material coordinates) with the intact bonds drawn black. Burgers circuits were performed (see text).

cuit). They were mapped to the lower picture where they are open. The right circuit yields a Burgers vector $\mathbf{b} = (\mathbf{b}^{\parallel}, \mathbf{b}^{\perp})$ with $\mathbf{b}^{\parallel} = \mathbf{g}_3 - \mathbf{g}_4 = (4/\sqrt{2+\tau}, 0, 0)^T$. It corresponds to the short face diagonal of a rhombohedron. The phason component is $\mathbf{b}^{\perp} = \mathbf{g}_5 + \mathbf{g}_6 = (4\tau/\sqrt{2+\tau}, 0, 0)^T$ or the long face diagonal of a rhombohedron. From the left circuit we obtain a Burgers vector $-\mathbf{b}$. DILGER ET AL. had observed a Burgers vector with an additional screw component $b_y = 4(2-\tau)/\sqrt{2+\tau}$ [99].

Frequently, shortly before the recombination of the dipole, Burgers vectors with a parallel component $\mathbf{b}_l^{\parallel} = \mathbf{g}_1 - \mathbf{g}_2 = (4\tau/\sqrt{2+\tau}, 0, 0)^T$ were measured. We refer to it as the *long* Burgers vector, the other is the *short* Burgers vector. The phason component is $\mathbf{b}^{\perp} = \mathbf{g}_2 - \mathbf{g}_1 = (-4/\sqrt{2+\tau}, 0, 0)^T$. Again, they correspond to the two different face diagonals of a rhombohedron but this time the other way round.

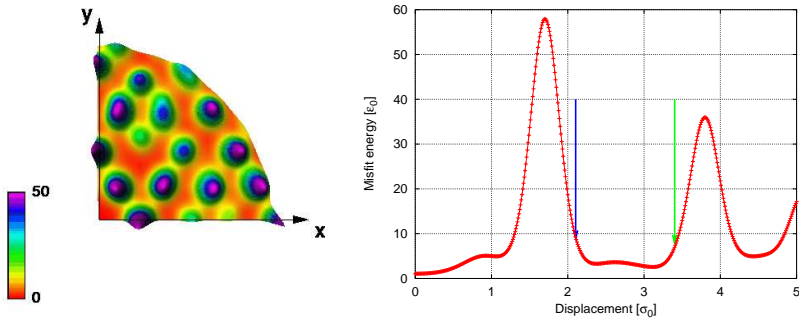


Figure 5.8: Gamma surface and Burgers vectors. Left: gamma surface of the observed glide plane. Right: cut through the gamma surface in Burgers vector direction (see text).

We can justify the Burgers vectors from the gamma surface of the structure. In the left part of fig. 5.8 the gamma surface for the observed glide plane is displayed⁶. The Burgers vector points into the x -direction.

A cut along this direction is displayed in the right part of fig. 5.8. There are two large maxima at $u = 1.71\sigma_0$ and $u = 3.11\sigma_0$. In-between

⁶The gamma surface corresponding to the second-largest separation distance $0.50\sigma_0$ is rather similar: the positions of the extrema are exactly the same while their values are slightly different.

there is a region with rather low misfit energy and two flat minima at $u = 2.37\sigma_0$ and $u = 3.14\sigma_0$ with $E_{misfit} = 2.28\varepsilon_0$ resp. $1.40\varepsilon_0$ per atom. This corresponds to 58%, resp. 34% of the average potential energy per atom in a perfect sample. A relaxation in the z -direction (normal to the glide plane) reduces those values by 20% but neither changes the overall shape nor the ratios of the values of the minima.

The blue arrow indicates the short Burgers vector described above. It does not exactly correspond to the first minimum but has a misfit energy 2.6 times larger. An explanation for this discrepancy can be found in the non-local character of quasicrystalline gamma surfaces: imagine a displacement which leads to a configuration where the alignment of the atoms is energetically favorable at most places in the glide plane. But there are always few other places where they lead to a large misfit energy. Total relaxation of the core structure and the phason wall might also favor the observed Burgers vector to the displacement read from the gamma surface. The long Burgers vector (green arrow) also does not correspond exactly to the second minimum. Here, the ratio of their energies is 2.1.

If in a configuration containing a dislocation dipole the shear was decreased to considerably lower values the two dislocations reversed their motion. They approached each other and annihilated. The structure was not perfectly reconstructed. Some point-like defects remained in the glide plane.

5.3 Simulations of a sample containing a dislocation

5.3.1 Construction of the dislocation

These simulations were performed on the large sample which contained 581,612 atoms. A PN dislocation with the short Burgers vector and the observed width $\zeta = 4.9$ was built into the sample (cf. fig. 5.3.1). The atoms within the step at the left edge of the sample were removed reducing the number of atoms to 575,199. The sample was prepared in the same way as described in sec. 5.1.2. We used periodic boundaries in y -direction (parallel to the dislocation line), and restricted boundary conditions in the other directions: only motion in y -

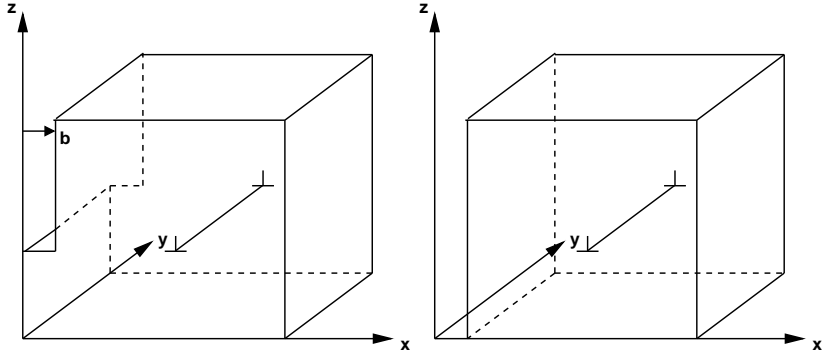


Figure 5.9: Sample with a built-in dislocation. A PN displacement field was applied. The step at the left side was removed (see text).

direction was allowed⁷. The simulations were performed at a pressure of $p = 1.04\varepsilon_0/\sigma_0^3$ at three different temperatures: at $T = 0.01\varepsilon_0$, referred to as the **zero-temperature simulation**, at $T = 0.6\varepsilon_0$, referred to as the **low-temperature simulation**, and at $T = 0.9\varepsilon_0$, referred to as the **high-temperature simulation**. The shear rate was reduced to $\dot{\varepsilon} = 10^{-4}t_{MD}^{-1}$.

5.3.2 Macroscopic analysis

Stress-strain curves

Like in the simulations of a perfect sample, there is a linear elastic regime in the stress-strain curves (fig. 5.10) with almost the same shear moduli $\mu = \mu(T)$. Again, a drop of the curves indicates the onset of plastic deformation: the built-in dislocation starts moving.

While the critical shear strain ε_c *increases* with temperature, the critical stress σ_c *decreases*. In the zero-temperature simulation σ_c has a value of $2.85 \varepsilon_0/\sigma_0^3$ which we consider as an estimate of the Peierls stress at zero temperature. At elevated temperatures the values are

⁷To allow a relaxation of the core region the atoms also could move in the x -direction during the GLOC relaxation.

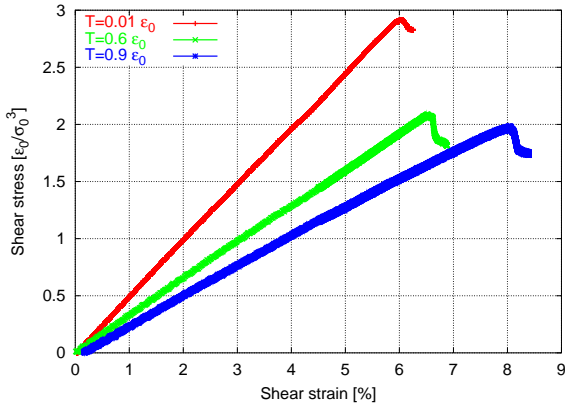


Figure 5.10: Stress-strain curves with a built-in dislocation for various temperatures.

significantly lower (2.13 resp. $1.97 \varepsilon_0/\sigma_0^3$ in the low- resp. in the high-temperature simulation). Compared to the measurements of the first simulation series they are lower by a factor of 2.5 on the average. The sample becomes more ductile with increasing temperature.

Mean square displacements

The mean square displacements

$$\Delta_{x/y/z}(t) = \frac{1}{N} \sum_i ((\mathbf{r}^{(i)}(t) - \mathbf{r}^{(i)}(t=0)) \cdot \mathbf{e}_{x/y/z})^2. \quad (5.1)$$

were calculated separately for each of the three directions $\mathbf{e}_x, \mathbf{e}_y$, and \mathbf{e}_z . Δ_x was corrected for the elastic strain. The results are displayed in fig. 5.11 where the red line always corresponds to the low temperature simulation and the green line to the high temperature simulation (in the zero-temperature simulation almost no diffusion was observed). The time scale is shifted so that at both temperatures the time step zero corresponds to the start of the motion.

In the low- and in the high-temperature simulation Δ_x remains constant until the dislocation starts moving. Then it increases linearly. The

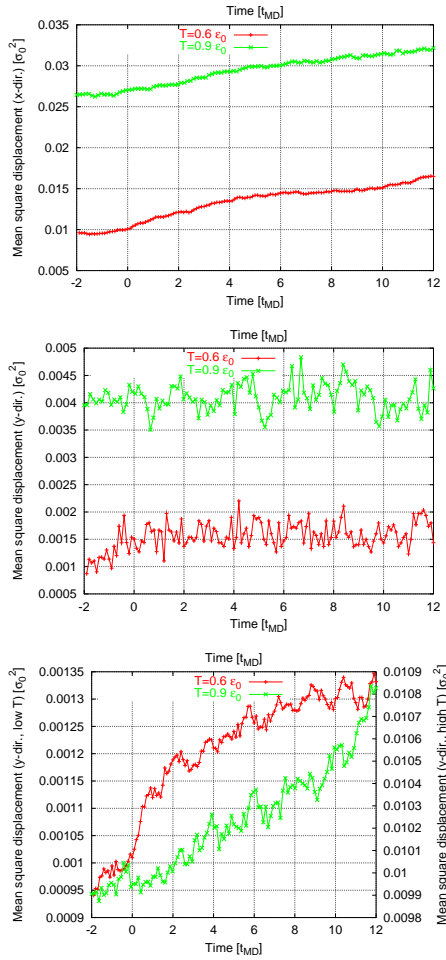


Figure 5.11: Mean square displacements for the various directions at $T = 0.6\epsilon_0$ (red line) and $T = 0.9\epsilon_0$ (green line). From top to bottom: x -, y -, and z -direction. Note the two scales differing by a factor of 10 for the mean square displacements in the bottom picture (otherwise the sudden increase of the red curve as soon as the dislocation starts moving would not become resolved).

observations can be explained by the motion of the dislocation which introduces displacements of b in the x -direction. There are no such displacements in the other two directions so that the corresponding components are smaller by one order of magnitude.

Δ_y remains constant for both the low- and the high-temperature simulations. Δ_z increases as soon as the dislocation starts moving. In the low temperature simulation this increase is rather pronounced. We attribute this to diffusion normal to the glide plane within the phason wall. This agrees with the assumption that at high temperatures the it can anneal diffusively.

Activation volume

We have also performed stress-relaxation experiments. Immediately after the dislocation started moving, the total strain was kept constant and the shear stress σ was measured as a function of time. When we plot $\ln \dot{\sigma}$ versus σ the strain-rate sensitivities (fig. 5.12) from a linear fit are $22.0\sigma_0^3/\varepsilon$ in the low-temperature and $67.7\sigma_0^3/\varepsilon$ in the high-temperature simulation. This yields activation volumes of $V_{\text{low}} = 13.2\sigma_0^3 = 1.4b^3$ and $V_{\text{high}} = 60.9\sigma_0^3 = 6.5b^3$. The first value is extremely small. The second is still rather small even if we assume a Peierls mechanism.

To explain the measured values we should first keep in mind that both the strain-rate sensitivity and the activation volume are thermodynamic variables. In a real stress-relaxation experiment there is a huge number of dislocations with a distribution of velocities. We observe only one single dislocation with one velocity. More important, the shear rate in our simulations is by orders of magnitude larger than in experiments. It follows that the obstacles are mainly overcome by the shear stress. In the microscopic analysis it will turn out however, that thermal activation indeed plays a role. The motion occurs by discrete jumps in the zero-temperature simulation but is more viscous at elevated temperatures.

Thermal activation involves a Boltzmann factor $\exp(-\Delta H/k_B T)$. It can be interpreted as the probability that the dislocation is able to overcome an obstacle. In the case of large stress the dislocation is dragged forward rather fast and rests only little time in front of an obstacle. Hence, thermally activated overcoming will only occur seldom. This situation corresponds to the case of both small distance d between

stable and metastable position and small Gibbs activation enthalpy ΔG in the right part of fig. 2.13. The large shear rate of our simulations leads to a systematic underestimation of the activation volumes. For more realistic results it should be reduced which is difficult to achieve as the simulation time increases accordingly.

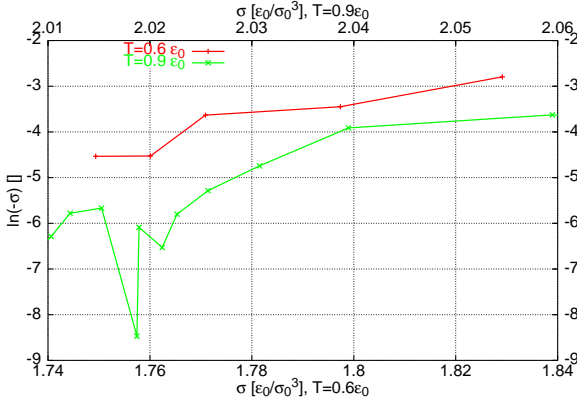


Figure 5.12: Strain-rate-sensitivity from a $\ln \dot{\sigma}$ versus σ plot at $T = 0.6\varepsilon_0$ (see text).

5.3.3 Microscopic analysis

Displacement field

For an analysis of the shape of the dislocation core we look at snapshots of the simulation after the onset of plastic deformation. Fig. 5.13 shows the displacement field immediately after the dislocation has started moving. It has preserved its arcus tangent shape. The position of the dislocation core varies with y , as indicated by the curved blue line. During the whole simulation we measure a core width of approximately $\zeta = 5\sigma_0$. This is almost the same value as in the first simulation series. However, the scattering of the displacement field data is rather large. For a precise analysis of the core shape we therefore turn to retiling visualizations.

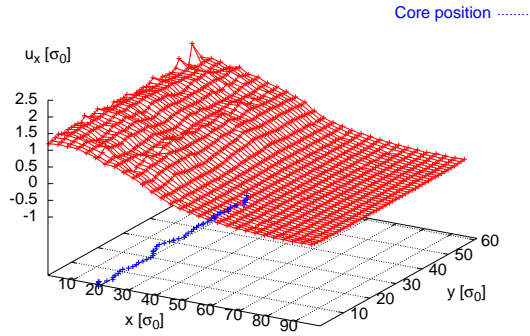


Figure 5.13: Displacement field of the moving dislocation. The arcus tangent shape is preserved but the core (blue line) is curved.

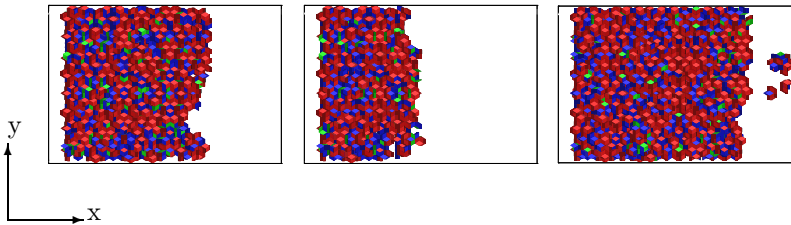


Figure 5.14: Retiling visualizations (I). The view direction is normal to the glide plane. From left to right: zero-, low-, and high-temperature simulation. The arrangements of tiles at the right edge of the high-temperature visualization are artefacts: there the elastic distortion of the bonds has become so large that they were detected as broken.

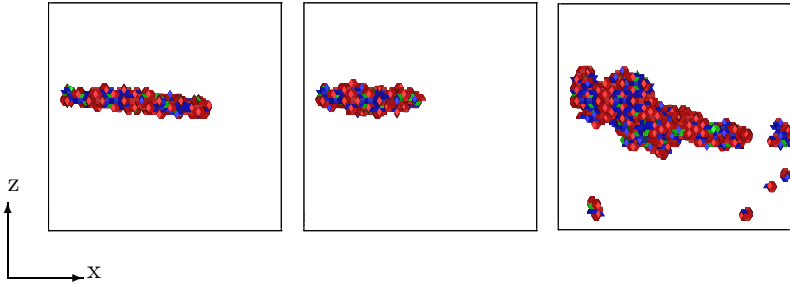


Figure 5.15: Retiling visualizations (II). The view direction is parallel to the y -direction. From left to right: zero-, low-, and high-temperature simulation. The thickness of the phason wall increases with temperature and at $T = 0.9\epsilon_0$ even climb can be observed (see text).

Retiling visualizations

In fig. 5.14 retiling visualizations are displayed where the view direction is normal to the glide plane (from left to right: zero-, low-, and high-temperature simulation). The dislocation core at the right end of the phason wall always has a curved shape. We attribute this observation to pinning at obstacles. The curvature is restrained by the line tension.

In fig. 5.15 the view direction is parallel to the line direction. From left to right: zero-, low-, and high-temperature simulation. Both the dislocation core and the phason wall become more extended in the direction normal to the glide plane (thicker for short) with increasing temperature. In the zero-temperature simulation the phason wall is as thick as the core which agrees with the observation that no diffusion occurs. At elevated temperatures the phason wall is thicker than the core due to diffusion processes. The increasing thickness of the core with temperature could be explained by the assumption that the dislocation performs a "slight climb" to avoid the obstacles it encounters in the glide plane, especially in the high temperature simulation. This has indeed been observed in simulations on the 2D binary tiling at high temperatures [93]. At lower temperatures the dislocation had to cut the obstacles. Unfortunately, the resolution of our visualization technique is not sufficient to investigate such fine details.

The cores of dislocations in fcc crystals are much more narrow, around two or three lattice constants. Obviously, quasicrystalline dislocations involve much larger rearrangement of the atoms of the perfect structure.

In a region left of the plane $x \approx 44\sigma_0$ the high-temperature phason wall is even thicker. However, this is due to a mixed climb and glide motion of the dislocation. Initially, it was located on a glide plane at $z = 54\sigma_0$. In the course of the simulation it has climbed to a glide plane below at approximately $z = 40\sigma_0$. Again, this glide plane is in-between two atomic planes separated by the largest possible distance $0.65\sigma_0$. Afterwards, the dislocation glides.

The climb motion can be explained from the geometry of the simulation box. Above the glide plane the particle density is enlarged especially within the core (remember that we have removed all particles with in the step at the left lower side of the sample). A climb motion downwards enlarges the core region and due to relaxation processes its density is reduced. However, this requires diffusion of atoms into the core and, hence, the creation of voids. We assume that they nucleate in the phason wall. This can only occur at high temperatures.

In fig. 5.16 we have extracted the current position of the core for various snapshots. In animations from a sequence of snapshots it turns out that the type of motion changes with temperature. In the zero-temperature simulation the dislocation moves unsteadily by large jumps. Between the jumps it rests for a long time in a stable configuration. There are only few such configurations that are assumed in the course of the simulation. Most of them are drawn in the left picture of fig. 5.16. The average separation between them is up to $15\sigma_0$. We conclude that there is no thermal activation. Instead, stress is accumulated until the dislocation breaks away from the most stable obstacle at which it is pinned. Once it has started to move it has enough inertia to overcome further obstacles dynamically. The dislocation proceeds **as a whole**. The motion stops as soon as an obstacle is encountered which is strong enough to pin the dislocation again.

At elevated temperatures the motion is rather viscous. One segment of the dislocation overcomes an obstacle and proceeds to the right while its neighboring segments are still pinned. The distance a segment moves in such a step is only few σ_0 . It is also smaller in the high-temperature case. In an animation created from a sequence of snapshots the high-

temperature motion appears more viscous than in the low-temperature case.

Velocity and plastic strain rate

Fig. 5.17 shows the average positions of the dislocation core as a function of time. They were determined from the area swept by the dislocation divided by L_y . To exclude artefacts from the process of inserting the dislocation we have restricted our analysis to snapshots where all segments of the dislocation had already moved by at least $5.0\sigma_0$. The low-temperature dislocation moves at a rather constant velocity of about $0.51 \sigma_0/t_{MD}$ (red curve). In the high-temperature simulation the dislocation ceases its climb motion at about $x = 55\sigma_0$ (green curve). We have determined the average velocity beyond this point to $0.85 \sigma_0/t_{MD}$ ⁸. The measured values correspond to 4% resp. 6% of the shear wave velocity. Together with the decreasing value of σ_c we conclude that the sample becomes more ductile with increasing temperature.

T [ε_0]	$v [\sigma_0/t_{MD}]$	$\dot{\varepsilon}_{pl}^{(1)} [10^{-4}/t_{MD}]$	$\dot{\varepsilon}_{pl}^{(2)} [10^{-4}/t_{MD}]$
0.6	0.51	1.11	1.45
0.9	0.85	1.79	2.38

Table 5.3: Velocities and plastic strain rates $\dot{\varepsilon}_{pl}^{(1,2)}$ of the built-in dislocations from the simulations at elevated temperatures. The numbers denote how the value has been derived: from Orowan's equation (1) resp. from the decrease of the shear stress (2).

With the help of the Orowan equation (eq. (2.27)) we can calculate the plastic strain rate $\dot{\varepsilon}_{pl}$. The modulus of the Burgers vector is $4/\sqrt{2 + \tau} \approx 2.103\sigma_0$ and the dislocation density is 1 (the number of dislocations) divided by the area of the xz -surface $L_x L_z \approx 10^4 \sigma_0^2$. The corresponding values are listed as $\varepsilon_{pl}^{(1)}$ in tab. 5.3.

⁸In the zero-temperature simulation there was no well defined dislocation velocity due to the jump-like motion.

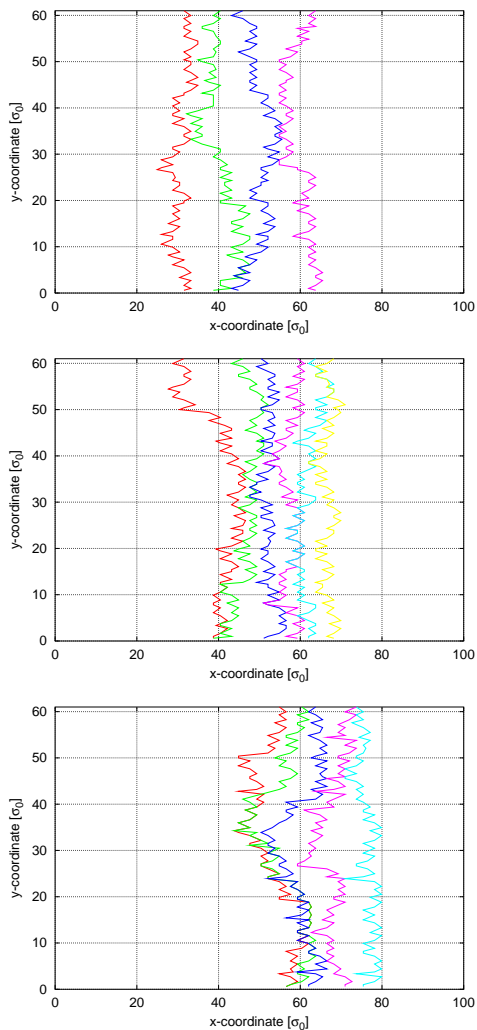


Figure 5.16: Dislocation core motion with time. From top to bottom: zero-, low-, and high-temperature simulation. The different colors denote different snapshots (see text). The rectangular grid corresponds to the glide plane.

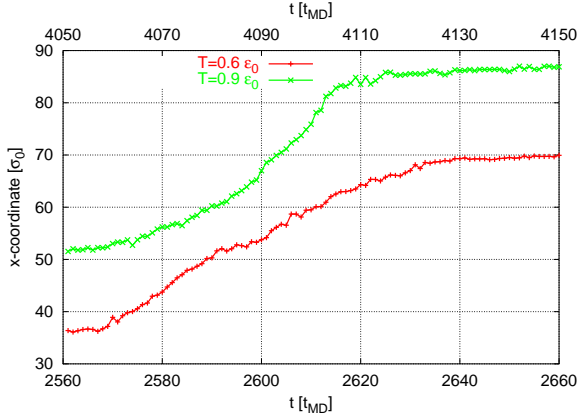


Figure 5.17: Position of the dislocation core as a function of time (see text).

There is an alternative possibility to determine $\dot{\epsilon}$. From our simulation of a stress relaxation experiment we can calculate the plastic strain rate from $\dot{\sigma}$ according to eq. (2.31) by $\dot{\epsilon}_{\text{pl}} = \dot{\sigma}/\mu$. We measure $\dot{\sigma} = -0.005 \frac{\epsilon_0}{t_{\text{MD}} \sigma_0^3}$ in the low-temperature simulation leading to $\dot{\epsilon} = 1.45 \cdot 10^{-4}$. In the high-temperature simulation a value of $\dot{\sigma} = -0.006 \frac{\epsilon_0}{t_{\text{MD}} \sigma_0^3}$ leads to $\dot{\epsilon} = 2.38 \cdot 10^{-4}$ at $T = 0.9\epsilon_0$ (tab. 5.3, denoted as $\epsilon_{\text{pl}}^{(2)}$).

The ratios of the plastic strain rates are almost equal. However, the values obtained from measurements of $\dot{\sigma}$ are larger by 33%. This discrepancy might be the result of the annealing of the phason wall by atomic rearrangements. They lead to an additional decrease of σ .

From the obtained values of the plastic strain rate $\dot{\epsilon}_{\text{pl}}$ as a function of time we could in principle have determined the strain-rate sensitivity by plotting $\ln \dot{\epsilon}_{\text{pl}}$ versus σ . However, the data scattered so much that no reasonable value could be obtained. This scattering can be understood from the graphs in fig. 5.17. They consist of segments whose slope varies considerably. They correspond to an alternating acceleration and deceleration of the dislocation. In real experiments where the average

velocity of a large ensemble of dislocation is measured this effect can never be observed.

5.4 Energy of a model dislocation

To further study the motion of the dislocation and to determine the relevant obstacles, we have performed a calculation of the energy of a model dislocation. A PN edge dislocation with a displacement

$$u_x(x) = -\frac{b}{2\pi} \arctan \frac{x - x_{\text{core}}}{\zeta} \quad (5.2)$$

was built into the sample. Here, x_{core} is the core position which was varied to move the dislocation through the sample. With the same pair interactions of Lennard-Jones type as in the MD simulations the unrelaxed dislocation energy E_{disl} was determined as a function of x_{core} . Only bonds between atoms in a small region parallel to the glide plane were taken into account. In the following we discuss how good E_{disl} agrees with the predictions of the PN model.

The bonds taken into account can be divided into two classes: bonds which cross the glide plane and others which do not. We assume that the energy from the latter bonds corresponds to the elastic energy E_{el} stored in the two halves in the PN model. E_{el} is constant because it was determined in a continuum picture. It will turn out that atomistic calculation leads to a non-constant expression.

We consider the energy from the bonds crossing the glide plane as an approximation of the misfit energy E_{mis} . Because in PN theory it is also calculated from a discrete summation we expect a rather good agreement of the values, at least in the case of a periodic structure. Especially, we expect that the periodicity in the lattice constant is correctly reproduced. To check the quality of our approximation we have first performed a test calculation in a 2D hexagonal lattice. We have also varied the width ζ to study its influence on the results.

In a quasicrystal $E_{\text{mis}}(x_{\text{core}})$ should not be a periodic function because of the lack of translational periodicity. We do not know *a priori* the influence on the results and have therefore performed a second test calculation in an approximant of the 2D binary tiling where the motion of the dislocation is well understood and the relevant obstacles are

known. We hoped to find a relation between the obstacles and extrema of our energy function.

Finally, we have studied the energy landscape of the IBT.

5.4.1 Test calculations in a hexagonal lattice

A first test calculation was performed in a 2D hexagonal lattice with lattice constant b . This value was also chosen as the position s_0 of the potential minimum. The sample length in Burgers vector direction was $100b$. Only the two neighboring atomic planes parallel to the glide plane were taken into account. In the upper part of fig. 5.18 the dislocation energy E_{disl} as a function of core position x_{core} is displayed. It is split into the elastic contribution E_{el} and the misfit contribution E_{mis} for various dislocation widths $\zeta = 0.5b$ (red=elastic contribution, green=misfit contribution) and $\zeta = b$ (blue=elastic contribution, magenta=misfit contribution). x_{core} was varied between $-10b$ and $110b$ so that both the entry of the dislocation into the sample and its exit could be observed.

The elastic energy E_{el} at $-10b$ corresponds to approximately $-1.0\epsilon_0$, the value measured in the perfect lattice. This is due to a zero displacement everywhere in the sample. As x_{core} approaches zero the dislocation enters the sample and the elastic energy increases. Then, instead of the constant value predicted by the PN model we observe an oscillation with period length b due to our atomistic calculation. The magnitude of both the increase and the amplitude of the oscillation decrease with increasing ζ . As x_{core} exceeds $100b$ the dislocation leaves the sample. E_{el} then assumes its initial value.

The misfit energies we observe an almost similar increase and a decrease at the sample boundaries⁹. This part of the energy can be compared to the constant part $\mu b^2/(4\pi(1-\nu))$ of the misfit energy in eq. (2.23). In our calculation it is **not** constant but increases with increasing dislocation width¹⁰. Again, this is a result of the atomistic treatment while eq. (2.23) was obtained by integration. We note that for reasonable values of the ζ (in-between $3b$ and $5b$) the elastic part can be neglected. It is at least two orders of magnitude lower than the misfit part.

⁹The reason for the different values at $-10b$ and $110b$ is the free surface at $x = 0$.

¹⁰A continuum dislocation with $\zeta = 0$ would have a constant misfit energy of zero.

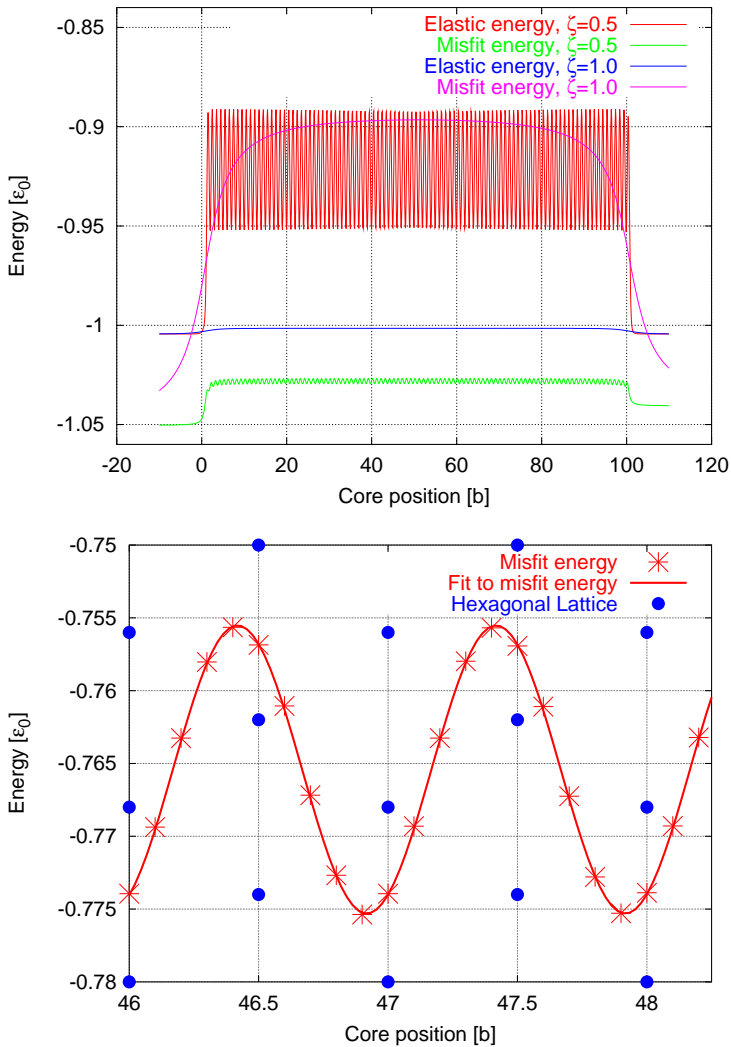


Figure 5.18: Dislocation energy in a hexagonal lattice. Top: elastic and misfit contribution for various ζ (see text). Bottom: the misfit energy (red asterisks) has a sinusoidal shape (red curve, sinusoidal fit) with a period length equal to the lattice constant. The blue dots denote the lattice atoms.

Note that both the increase and the decrease become more and more gradual as ζ increases: the core must be located far from the sample boundaries to guarantee a constant u there. To avoid this gradual increase the sample length must be chosen large.

The most interesting part of the misfit energy curves however, its variation with x_{core} , is independent of the sample size. In the green curve the **periodic** variation of E_{mis} is clearly visible. It does not become resolved in the magenta line corresponding to $\zeta = b$ because the Peierls energy decreases with increasing ζ :

$$W_P \propto \exp -4\pi\zeta/b . \quad (5.3)$$

The period length is b in accordance with WANG'S treatment [57].

In the lower part of fig. 5.18 we see that a sine function (red solid line) can be fitted well to the data (red asterisks). The positions of the minima are in agreement with [57] as can be seen from the positions of the lattice points (blue dots). From the fit parameters we can determine the value of the Peierls energy. In the right part of fig. 5.19 these values are plotted logarithmically as a function of ζ . A straight line can be fitted so that the relation of eq. (5.3) is fulfilled. From the slope of the line we determine $b = 1.7$ which deviates considerably from the Burgers vector modulus 1.0. From its value at $\zeta \rightarrow 0$ we read $\mu/(1 - \nu) = 22.6\varepsilon_0/b^3 \pm 18.8\varepsilon_0/b^3$ while deformation experiments suggest a value of $42.2\varepsilon_0/b^3$.

We conclude that our method of calculating the energy of a PN dislocation does not produce precise quantitative results. Furthermore, the parts of the energy predicted to be constant depend on the dislocation width. This is a result of our atomistic calculation while PEIERLS AND NABARRO had used different methods in a continuum picture. The periodic variation of the dislocation energy however, is reproduced well. Additionally, the dependence of the Peierls energy on the width is in good agreement with the theoretical description. If we restrict ourselves to qualitative conclusions we expect that the dislocation energy calculated according to our method provides interesting information about the stress exerted on a moving dislocation. We will use it to deduce the obstacles to dislocation motion in a quasicrystal.

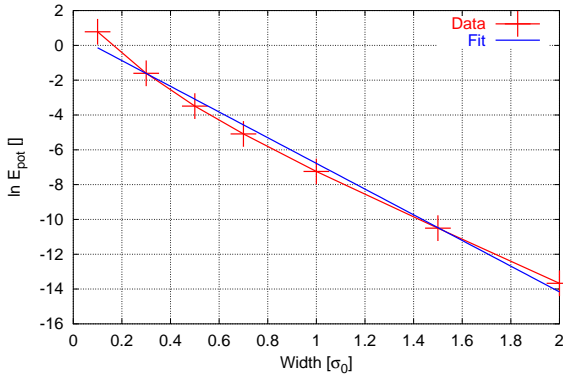


Figure 5.19: Peierls energy as a function of dislocation width. From the logarithmic plot we conclude that the relation $W_P \propto \exp(-4\pi\zeta/b)$ is fulfilled.

5.4.2 Calculations in the 2D binary tiling

To determine whether the dislocation energy from our calculations can serve as a tool to identify the obstacles to dislocation motion we have performed a similar calculation of $E_{\text{disl}}(x_{\text{core}})$ in the 2D binary tiling. We chose the potential parameters and the observed glide plane according to simulations [93]. Only the bonds between atoms in the three neighboring atom rows on both sides of the glide plane were taken into account. This choice is somewhat arbitrary but the results do not change substantially if more or less rows are included.

Let us first consider the upper part of fig. 5.20. The dislocation enters the sample at $x_{\text{core}} = 0$ and both the elastic energy and the misfit energy increase. Both curves then show a quasiperiodic oscillation. While the elastic energy oscillates around a constant value, there is an additional linear increase of the misfit energy with x_{core} . This is due to the phason wall introduced by the moving dislocation. The slope $2.36\varepsilon_0/\sigma_0$ corresponds to the unrelaxed stacking fault energy per unit length. The value agrees with the value read from the gamma surface.

We have also varied the dislocation width. The overall shape of the

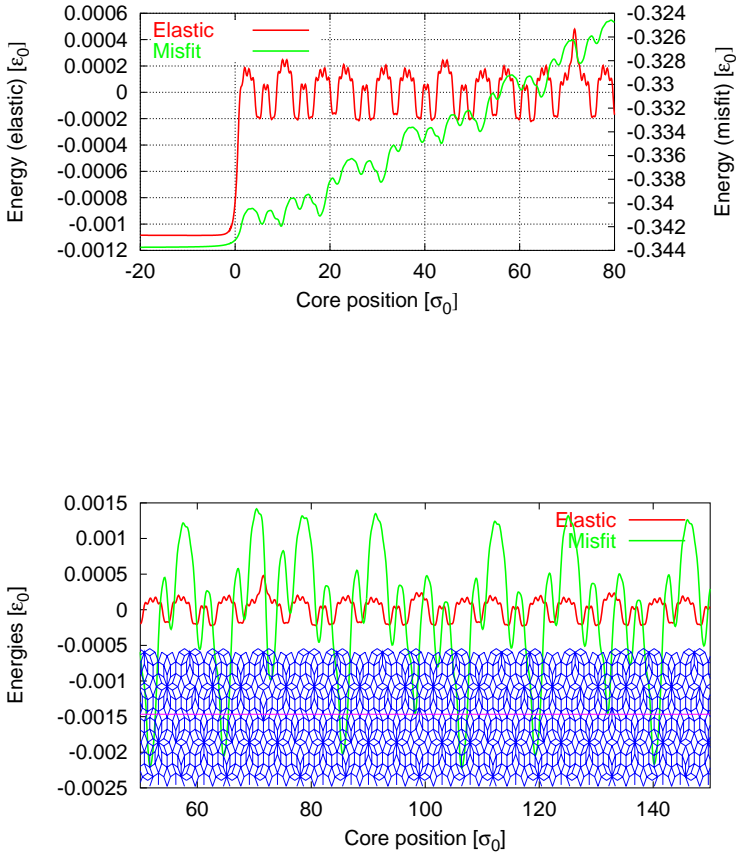


Figure 5.20: Dislocation energy in the 2D binary tiling. Upper picture: elastic energy (red) and misfit energy (green). The sample boundary is located at $x_{\text{core}} = 0$. Lower picture: elastic energy (red) and misfit energy (green, the linear contribution from the phason wall is subtracted) together with the tiling. The magenta line denotes the glide plane.

curves did not change, only less details were resolved with increasing ζ . But both the positions of the extrema and the ratio of their energies remained the same so that we restrict our discussion to the case of a rather narrow dislocation where $\zeta = 1.0\sigma_0$. Here, the elastic contribution is already smaller than the misfit contribution by two orders of magnitude. Especially for the widths observed in [93] ($\zeta \approx 6.0\sigma_0$) it is negligible.

In fig. 5.19 the elastic (red) and the misfit (green) contribution are plotted together with the tiling (the magenta line indicates the glide plane). The misfit energy has been corrected for the linear increase. Both curves are quasiperiodic functions as can be seen from their Fourier transform which has peaks at integer linear combinations of 1 and τ . The elastic energy becomes maximal at the crown-like structure elements which were proposed as most important obstacles to dislocation motion [93]. At these obstacles the misfit energy curve goes from a minimum to a maximum value if the „crown points upwards”. In the other case it goes from a maximum to a minimum. Extrema of large size are also observed at positions where a single thin rhomb lies in the glide plane. The type of extremum again depends on its orientation. This is in agreement with observations by RUDHART [127]. In simulations of crack propagation these rhombs served as obstacles as the crack tip circumvents them.

5.4.3 Calculations in the IBT

We have found that in the 2D binary tiling the dislocation energy is extremal whenever the core traverses an obstacle and therefore serve as an indicator for them. We assumed that this result also holds true in the IBT and performed a similar calculation. From the extrema of the obtained function we attempted to identify the dominant obstacles to dislocation motion.

Again, a dislocation was moved through the sample according to eq. (5.2). The sample, the glide plane, and the potential parameters were the same as in the simulations described above. However, the calculations were restricted to atoms located closer than $2.0\sigma_0$ to the glide plane. The displacement field (eq. (5.2)) corresponds to that of a straight dislocation. The energy was calculated separately for every atomic plane normal to the ξ - or y -direction so that a 2D energy land-

scape was obtained as a function of x_{core} and y . The elastic contribution was neglected.

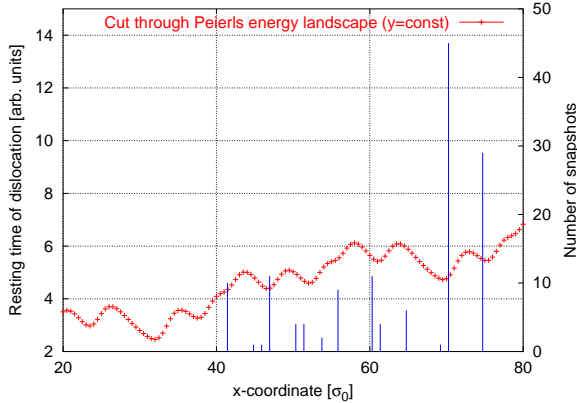


Figure 5.21: Cut through the dislocation energy landscape for fixed $y = \text{const}$. The blue bars indicate the number of observations of the dislocation core at the specific point (see text).

For every atomic plane a curve like the one displayed in fig. 5.21 was obtained. It can be viewed as a slice of the energy landscape for constant y . The curve is rather similar to the one in the upper part of fig. 5.20 as it contains an initial increase d and a slope α in addition to a quasiperiodic oscillation. Both d and α depended on y so that we can describe the obtained 2D energy landscape as a sequence of **1D energy functions** depending on x_{core} with different slopes α ¹¹ starting at different initial values d .

The initial value d corresponds to the constant part of the misfit energy. It has no influence on the variation of the stress encountered by the moving dislocation. We consider it as an integration constant from the integration of the stress as a function of x_{core} . We now calculated the stress function by differentiation with respect to x_{core} . Then an integration was performed where the new integration constant was chosen

¹¹These slopes could be read from a gamma surface where the same decomposition had been performed.

such that the new energy function had a value of zero at $x_{\text{core}} = 20.0\sigma_0$. This led to same energy functions as before except for a shift. The choice of $20.0\sigma_0$ guaranteed that the dislocation had already entered the sample completely.

Now all energy functions had a value of zero at $x_{\text{core}} = 20.0\sigma_0$. The slope of each of them was determined from a linear fit and subtracted. The remaining energy landscape only shows the energy variation with core position. It is displayed in the left part of fig. 5.22. We see a complex surface with minima and maxima of various shape and height. We now interpret the maxima as obstacles to the dislocation motion. The grey lines denote dislocation configurations from snapshots of the low-temperature simulation. They are preferably located in-between the maxima corresponding to a low dislocation energy. However, the line tension force restricts their curvature so that at several points the lines are located on the rise of a Peierls hill¹².

For a more quantitative investigation we return the energy function for a specific atomic plane ($y = \text{const}$) of fig. 5.21. The blue bars indicate observations of the dislocation from simulation snapshots at those positions. The height of the bar denotes the number of such observations. From the distribution of the bars and their heights we can again conclude that the dislocation lies favorably in the Peierls valleys and only seldom on the Peierls hills. We find similar results for all values of $y = \text{const}$.

We have found that the energy landscape provides an explanation for the observed dislocation configurations. It is interesting to compare it to the schematic drawing of TAKEUCHI ET AL. [85] which consists of long straight Peierls valleys (fig. 2.12) inspired by the observation of long, straight dislocations in i-AlPdMn. From this picture the authors could explain features of quasicrystalline plasticity. In the IBT we have not observed straight dislocations and consequently not such a simple energy landscape¹³. Instead we observe a much more complex structure with isolated hills of varying size. Some of them are located on parallel lines but they do not form well-defined valleys and hills so that the

¹²Of course the cores must travel across a Peierls hill in the course of the simulation. If the snapshot is taken at this moment the core will appear exactly on top of the maximum.

¹³Indeed, if we integrate the energy landscape with respect to y (corresponding to a straight dislocation) the result (fig. 5.22, lower picture) is similar to fig. 2.12.

quasicrystalline Peierls mechanism of [85] is not applicable to explain our simulation results. It would be interesting to perform the same simulations and energy calculations in BOUDARD ET AL.'s structure model of i-AIPdMn. Unfortunately, no suitable potential is available.

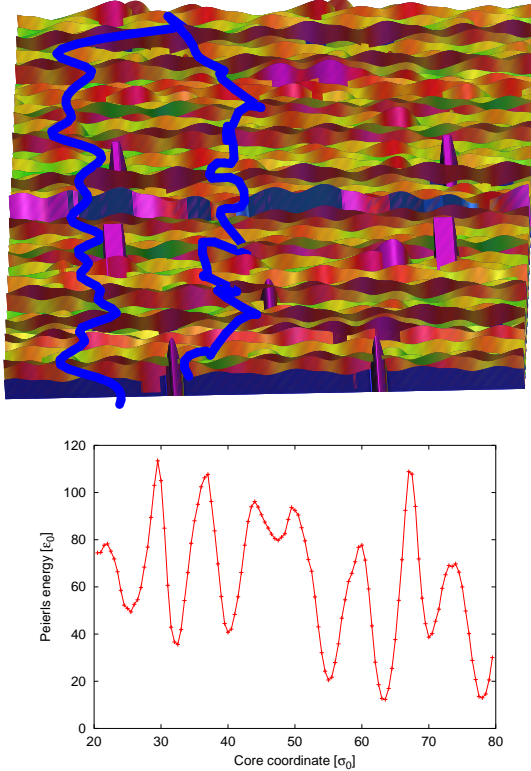


Figure 5.22: Top: dislocation energy landscape in the IBT. The height resp. the energy is color encoded. The landscape is a complex distribution of extrema of various heights. Dislocation configurations from the simulation have been embedded. They are preferably found in the Peierls valleys. Bottom: an integration of the landscape with respect to the line coordinate y yields the energy of a straight dislocation (see text).

A Peierls mechanism is even difficult to define in the energy landscape of fig. 5.22. The dislocations are curved so much that a kink can hardly be defined. We therefore attempted to find structural obstacles like clusters which might control dislocation motion. In the 2D binary tiling there are only few different atomic neighborhoods and there is a clear hierarchy among them according to their potential energy which serves as a criterion of their stability. The dominant obstacles could easily be identified. In the IBT the situation is much worse: there are a lot more atomic neighborhoods which also — depending on their internal symmetry — occur in up to 120 different orientations. Many of them have almost equal potential energies. It is *a priori* not at all clear that we may find "the" dominant obstacle.

We have performed an analysis based on the underlying 3D-Penrose tiling with the help of a configuration system for the vertices by HENLEY [128, 129]. He indexed every vertex by four numbers $(\alpha, \beta, \gamma, \bar{\beta})$ which denote the number of vertex neighbors of various types. α denotes their number along a rhombohedron edge, β along the short diagonal of a rhombohedron face, and γ along the short body diagonal of the oblate rhombohedron. $\bar{\beta}$ is the largest number of neighboring vertices grouped around any of the edges.

We have projected the most pronounced maxima of the energy landscape onto the glide plane together with all vertices of a specific type $(\alpha, \beta, \gamma, \bar{\beta})$ located closer to the glide plane than $1.0\sigma_0$ (see upper part of fig. 5.23). Most vertices did not have any correlation with the positions of the maxima with one exception. The vertices of type (5,6,1,4) are very likely to be found near the maxima.

This can be understood from the potential parameters used in our simulations. Bonds between small and large atoms are favored so that configurations where a corner atom has many large neighbor atoms should be more stable. The largest number of such bonds can be found in prolate rhombohedra at one of its six corners where the edges form one acute and two obtuse angles. Such a corner has been denoted *P3* by HENLEY because its solid angle is $3/20$ of 4π ¹⁴. The vertex of type (5,6,1,4) has four *P3* corners. Other vertices which have also four or more *P3* corners do not play an important role for one of the

¹⁴The solid angle of 4π is decomposed into twenty parts of $4\pi/20$ by the reference icosahedron. The prolate rhombohedron can be located at a vertex in a *P1* or a *P3* position, the oblate rhombohedra in an *O1* or an *O7* position.

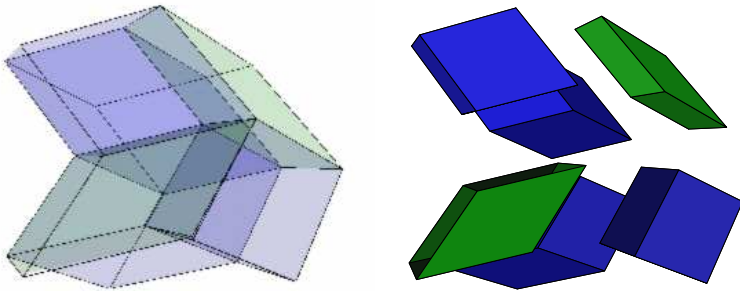
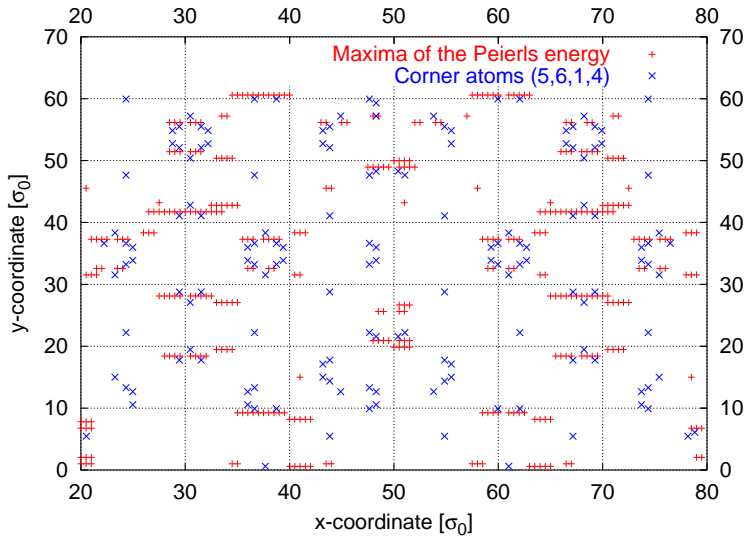


Figure 5.23: Identification of the dominant obstacles. Top: there is a correlation between the positions of the most pronounced maxima of the energy landscape and the corner atoms of type (5,6,1,4) (see text). The corresponding tile arrangement is displayed in the lower part. The faces are drawn transparent on the left. The right picture is an exploded view.

following two reasons. Some occur only seldom so that their role can be neglected. Other vertex configuration which occur as frequent as the vertex of type (5,6,1,4) get modified (cf. sec 1.4). Their prolate rhombohedra are always arranged in such a way that they belong to a rhombic dodecahedron which is centered at a neighboring vertex. The modification leads to a reduction of the number of bonds between small and large atoms. At the vertex of type (5,6,1,4) this modification does not occur.

We therefore postulate this structure element (see lower part of fig. 5.23) as an important obstacle to dislocation motion. We emphasize that not all corner atoms of type (5,6,1,4) can be related to extrema of the dislocation energy landscape and attribute this to their orientation: if many of the bonds are oriented normal to the glide plane they are strongly affected by the shear, otherwise not.

Chapter 6

Conclusions and outlook

In this thesis the reaction of an icosahedral model quasicrystal to shear deformation was analyzed with MD. The equations of motion were modified to simulate a shear flow at various temperatures. Relatively to the shear flow the atoms moved in a canonical ensemble. We intended to study the plastic behavior of the material, especially the generation and the motion of dislocations. The simulations had to be performed on large approximants of several 100,000 atoms. To analyze the simulation configurations a technique suitable for the visualization of defect structures in icosahedral quasicrystals was developed.

In a first simulation series we started from a perfect sample. We observed the nucleation of dislocation loops enclosing a phason wall. The nucleation was a result of phonon modes that became unstable under the influence of the applied shear stress. The shear stress required for the nucleation was very large. It corresponded almost to the theoretical shear strength and decreased with increasing temperature. Under its influence the loop increased and, after its screw segments annihilated due to the periodic boundary conditions, two edge dislocations remained.

They moved apart thereby enlarging the phason wall between them until they recombined with each other. After that we observed a partial amorphization on the glide plane so that the two halves slipped as a whole. It turns out that this simulation technique which was successfully applied in simulations on the 2D binary tiling is not appropriate for icosahedral quasicrystals, at least for numerically tractable sample sizes.

In 2D, the nucleation of a pair of dislocations does not require so much shear stress as the nucleation of a dislocation loop against which a large line tension force acts.

At least we could determine the preferred glide system of the IBT from those simulations. The dislocation loop nucleated always on a glide plane normal to a two-fold axis. The neighboring atomic planes always had the largest possible separation distance. The Burgers vectors pointed into a two-fold direction and corresponded to the face diagonal of a rhombohedron. It is in fairly good agreement with a minimum of the gamma surface of that glide plane. The dislocations have a displacement field similar to that of a PN dislocation. Their width was $\zeta = 4.9\sigma_0$.

In a second simulation series we constructed a sample containing an edge dislocation with the observed glide system. The sample was sheared at zero temperature, at a low temperature of 47% of the melting temperature, and at a high temperature of 71% of the melting temperature. The dislocation started moving at a critical stress which decreased with temperature. These stresses were lower by a factor of 2.5 compared to the first simulation series. The value of $2.85\varepsilon_0/\sigma_0^3$ is an estimate of the Peierls stress at zero temperature.

The dislocation core has a curved shape due to obstacles present in the structure. One segment of the dislocation is pinned and the neighboring segments have already advanced on both sides of the obstacle. The line tension force restrains the curvature. The observed dislocation configurations resemble the cluster-friction model of MESSERSCHMIDT ET AL. [81] rather than straight configurations with kink pairs.

At zero temperature and at low temperature the dislocations performed a pure glide motion. In the high temperature case they also climbed. The average glide velocity was in-between 4% and 6% of the shear-wave velocity. Together with the decreasing critical stress we conclude that the structure becomes more ductile with increasing temperature. Due to the relatively large shear rate their motion was mainly due to the shear stress as indicated by very small activation volumes.

However, thermal activation had an influence on the dislocation motion. At zero temperature the dislocation performed few large jumps between stable positions where it rested for a long time. Furthermore, the whole dislocation moved during such a jump. Its inertia made it move rather far (up to $15\sigma_0$) until it encountered obstacles strong enough to pin it again. The sample is rather brittle. Its behavior resembles the

observed deformation by fragmentation at room temperature [71]. The phason wall in the wake of the dislocation is almost perfectly planar. We conclude that the dislocation has cut the obstacles encountered in its glide plane.

At elevated temperatures the motion appeared rather viscous. Small segments overcame the obstacles at which they were pinned independently from their neighboring segments. The observation of both a broader core and a broader phason wall with increasing temperature is an indication that the dislocation swerves the obstacles by slight climb above or below them. This behavior has already been observed in simulations on the 2D binary tiling [93]. However, with our visualization method such fine details of the motion do not become resolved.

A static calculation of the energy of a straight PN dislocation was performed. Therefore, a PN displacement field was applied to the sample and the dislocation energy was determined as a function of the variable core position. The method was first tested on a 2D hexagonal lattice where the results were in good agreement with theoretical predictions. In a calculation on the 2D binary tiling the energy was a quasiperiodic function of the core position. The extrema could be related to obstacles in the structure which were already known from former simulation.

In the IBT a complex energy landscape was obtained. It did **not** consist of distinct Peierls valleys and hills. When we embedded dislocation configurations from the simulations they were located preferably around the maxima of the landscape so that it provides a good explanation for our observations of curved dislocations in the IBT. We conclude that their motion cannot be described by a Peierls mechanism. In real structures like i-AlPdMn the situation might be different. The dislocations observed there were rather straight which suggests a less complex energy landscape.

The observed curved dislocation configurations resemble those discussed in the cluster-friction model. We have attempted to find a dominant obstacle in the IBT corresponding to the Mackay clusters in i-AlPdMn by investigating whether certain atomic arrangements are correlated with the positions of the maxima. It turned out that a frequent atomic arrangement of the IBT occurs noticeably often in their vicinity while all other arrangements show no such correlation. In the underlying tiling it corresponds to an arrangement of three prolate and two

oblate rhombohedra. It contains the largest possible number of bonds between small and large atoms which are preferred because of our choice of the potential parameters. We suggest that it is the dominant obstacle to dislocation motion.

Future investigations of dislocation motion in icosahedral quasicrystals should concentrate on the process of overcoming the obstacles. Especially the open question whether the dislocation climbs around them or not should be dealt with. The visualization method described in this thesis could in principle be refined to provide a better resolution. To achieve this, the tiles could be decomposed into smaller units according to [125].

Even in the simulations with the built-in dislocation the critical stresses were rather high. Their initially straight shape might be an explanation for this effect. We propose that with the help of the dislocation energy landscape from the static calculation more suitable initial configurations could be derived. The relation between dislocation velocity and applied shear stress should be calculated.

In 2D simulations of crack propagations the nucleation of dislocations due to the stress concentrations at the tip was observed. Their motion at low stress could then be studied as well as the nucleation of secondary dislocations in the phason wall would become possible. Because of the boundary conditions of our simulation geometry we were not able to study them. 3D simulations of crack propagation are currently in progress as well as the simulation of shock waves. The latter lead to a variety of defect structures which have not all been identified yet.

Appendix A

Some remarks on continuum mechanics

In this appendix we introduce the basic concepts of continuum mechanics and classical elasticity theory. The concepts required to understand the continuum treatment of dislocations are presented. For a detailed introduction see for instance [130].

A.1 Fundamentals

Continuum mechanics is a phenomenological theory. Idealized mathematical models are derived to describe macroscopic phenomena. These models ignore the discrete atomistic structure of matter. Instead, matter is treated as a *continuum* in Euclidean space. Every point within the matter can be identified by *material* or *Lagrangian* or coordinates $\boldsymbol{\xi}$ or by the usual *spatial* or *Eulerian* or coordinates \mathbf{x} . A specific point in time is chosen, say, $t = 0$, at which the body is in its *reference state*. Then the material and spatial coordinates of any point in the matter are equal. The reference state should preferably be a state without stresses or strains, especially if its elastic or plastic properties are the subject studied.

The material coordinates are a unique identifier for a material point and **always** remain the same. The spatial coordinates of a point, how-

ever, change as it moves through space.

The *deformation* of a body is defined as the components of its motion which are not rigid, i.e., neither translation nor rotation. It can be described by the *configuration* D , a differentiable function which maps the material to the spatial coordinates:

$$\mathbf{x} = D(\boldsymbol{\xi}). \quad (\text{A.1})$$

We define the *displacement field* \mathbf{u}

$$\mathbf{u} := \mathbf{x} - \boldsymbol{\xi} \quad (\text{A.2})$$

as the difference between spatial and material coordinates. If the body is in the reference state then $D = \mathbf{1}$ and $\mathbf{u} = 0$.

Translations $\mathbf{u} = \text{const}$ do neither change the elastic state of the body nor its elastic energy. We must therefore consider the *distortion*, i.e., the gradient of the displacement $\beta_{ij} = \frac{\partial u_i}{\partial x_j}$. Its antisymmetric part $\beta_{ij}^A = \frac{1}{2}(\beta_{ij} - \beta_{ji})$ is a pure rotation which also does not change the elastic state. Only the symmetric part

$$\boldsymbol{\varepsilon} := \beta_{ij}^S = \frac{1}{2}(\beta_{ij} + \beta_{ji}) \quad (\text{A.3})$$

which we term *elastic strain* has an influence on it.

We define the *elastic stresses* acting on a body. If a body is cut along a plane each new surface tends to a new equilibrium state. This can be inhibited by a suitable force $\mathbf{t}(\mathbf{x})$ which acts on every point of the surface. This force depends linearly on $\mathbf{n}(\mathbf{x})$, the local normal vector:

$$\mathbf{t}(\mathbf{x}, \mathbf{n}) = \mathbf{t}(\mathbf{x}, \mathbf{e}_i)(\mathbf{e}_i \mathbf{n}) \quad (\text{A.4})$$

where \mathbf{e}_i are the base vectors. The elastic stress σ_{ij} becomes

$$\sigma_{ij} := t_i(\mathbf{x}, \mathbf{e}_i) \mathbf{e}_j. \quad (\text{A.5})$$

A.2 Classical theory of elasticity

The fundamental equation A.6 of elasticity theory states that a body is in mechanical equilibrium if and only if the external forces \mathbf{f} are equal to the internal stresses:

$$\frac{\partial \sigma_{ij}}{\partial x_j} + f_i = 0. \quad (\text{A.6})$$

We define the differential elastic energy stored in an infinitesimal volume element dV under an applied differential strain $d\varepsilon_{ij}$ as

$$dE := \sigma_{ij} d\varepsilon_{ij} dV. \quad (\text{A.7})$$

The relations described so far are valid in any material. They cannot describe the response of a body to loading. A law which describes this *stress-strain relationship* is required. Within elasticity theory several assumptions are made:

- **Locality in time:** the current elastic state does not depend on past states.
- **Locality in space:** the stresses at \mathbf{x} only depend on the strains at \mathbf{x} .
- **Homogeneity:** the law is the same everywhere in space.
- **Linearity:** The law is linear in both stress and strain.

From these assumptions follows *Hooke's law*:

$$\sigma_{ij} = C_{ijkl} \varepsilon_{kl} \quad (\text{A.8})$$

where C_{ijkl} is the *tensor of elastic constants*. Its inverse is

$$\varepsilon_{ij} = S_{ijkl} \sigma_{kl} \quad (\text{A.9})$$

with the *elastic compliance* $\mathbf{S} := \mathbf{C}^{-1}$.

C_{ijkl} has 81 components. However, this number is reduced because of the symmetries $\sigma_{ij} \leftrightarrow \sigma_{ji}$ and $\sigma_{ij} \leftrightarrow \sigma_{ji}$. They yield

$$C_{ijkl} = C_{ijlk} = C_{jikl} \quad (\text{A.10})$$

and 36 independent components remain. From the elastic energy expression

$$E = \int_0^\varepsilon \sigma_{ij}(\varepsilon'_{ij}) d\varepsilon'_{ij} = \frac{1}{2} C_{ijkl} \varepsilon_{ij} \varepsilon_{kl} \quad (\text{A.11})$$

and eq. (A.11) follows

$$\frac{\partial \sigma_{ij}}{\partial \varepsilon_{kl}} = \frac{\partial^2 E}{\partial \varepsilon_{ij} \partial \varepsilon_{kl}} = C_{ijkl}. \quad (\text{A.12})$$

According to Schwartz's theorem partial derivatives commute so that

$$C_{ijkl} = C_{klij} \quad (\text{A.13})$$

reduces the number once more to 21. This situation is indeed realized in triclinic crystals.

Crystalline symmetries (the symmetries of the underlying Bravais lattice) lead to even less elastic constants. An isotropic medium with the symmetry group $SO(3)$ has only 2 independent elastic constants, *Lamé's constants* λ and μ . Hooke's law takes the following simple form:

$$\sigma_{ij} = 2\mu\varepsilon_{ij} + \lambda\varepsilon_{kk}\delta_{ij} = 2\mu\varepsilon_{ij} + \left(K - \frac{2}{3}\mu\right)\varepsilon_{kk}\delta_{ij} \quad (\text{A.14})$$

where we have introduced the *compressibility* K . It describes the reaction of a body to isotropic expansion or compression: $\sigma_{ii} = 3K\varepsilon_{ii}$.

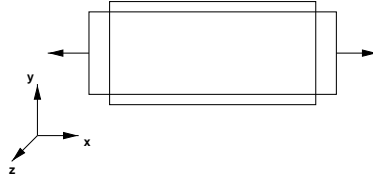


Figure A.1: Poisson's ratio ν is measured in an expansion experiment (see text).

For an illustration of eq. (A.14) we apply uniaxial stress σ_{zz} to an isotropic body (fig. A.2). It expands in z -direction: $\varepsilon_{zz} > 0$ and contracts in the other directions: $\varepsilon_{xx} = \varepsilon_{yy} < 0$. From eq. (A.14) follows

$$\sigma_{xx} = \sigma_{yy} = (\lambda + 2\mu)\varepsilon_{xx} + \lambda(\varepsilon_{yy} + \varepsilon_{zz}) = 0 \quad (\text{A.15})$$

$$\sigma_{zz} = (\lambda + 2\mu)\varepsilon_{zz} + \lambda(\varepsilon_{xx} + \varepsilon_{yy}). \quad (\text{A.16})$$

From eq. A.15 we calculate the ratio ν between expansion and contraction

$$\nu := -\frac{\varepsilon_{xx}}{\varepsilon_{zz}} = -\frac{\varepsilon_{yy}}{\varepsilon_{zz}} = \frac{\lambda}{2(\lambda + \mu)}. \quad (\text{A.17})$$

ν is called *Poisson's ratio*.

Appendix B

Estimation of the nucleation stress of a dislocation loop

The critical stress necessary for the nucleation of a dipole can be estimated the following way. The energy W of the dislocation loop consists of three contributions

$$W = W(r) = W_{loop}(r) + W_{\tau}(r) + W_{SF}(r), \quad (\text{B.1})$$

the elastic self energy of the loop W_{loop} , the energy W_{τ} caused by the external stress, and W_{SF} , the stacking fault energy.

The self energy can be calculated according to [35]

$$W_{loop} = \frac{\mu b^2 r}{4} \frac{2 - \nu}{1 - \nu} \left(\ln \frac{4r}{r_0} - 2 \right). \quad (\text{B.2})$$

The contribution from the resolved shear stress τ is according to eq. (2.13)

$$W_{\tau} = -\tau b \pi r^2. \quad (\text{B.3})$$

The circular stacking fault has an energy of

$$W_{SF}(r) = \gamma \pi r^2 \quad (\text{B.4})$$

where γ is the misfit energy per unit area. Minimizing eq. (B.1) with respect to r leads to

$$r_c = \frac{\mu b}{8\pi\tau} \frac{2-\nu}{1-\nu} \left(\ln \frac{4r}{r_0} - 1 \right). \quad (\text{B.5})$$

At r_c the value of the energy is

$$W_c = \frac{\mu b^2 r_c}{8} \frac{2-\nu}{1-\nu} \left(\ln \frac{4r}{r_0} - 3 \right). \quad (\text{B.6})$$

This expression must be compared with the thermal contribution which is usually a fraction of 1 eV. In the simplest case $T = 0$ the solution of the transcendental equation $W_c = 0$ is

$$r_c = \frac{e^3}{4} \approx 5r_0. \quad (\text{B.7})$$

Then the critical stress becomes

$$\tau_c = \tau(r_c) = \frac{\mu b}{\pi e^3 r_0} \frac{2-\nu}{1-\nu}. \quad (\text{B.8})$$

Inserting typical values like $r_0 = b/3$ and $\nu = 1/4$ leads to $\tau \approx \mu/9$. This value of τ is comparable the theoretical shear strength.

List of Figures

1.1	Diffraction patterns of $i\text{-Al}_{86}\text{Mn}_{14}$	14
1.2	Samples of quasicrystals.	15
1.3	Penrose tiling and diffraction pattern.	18
1.4	Prolate and oblate rhombohedron.	19
1.5	Cut and project method	20
1.6	Flip in the Penrose and the 3D Penrose tiling.	23
1.7	Decoration of the tiles.	24
2.1	Edge and screw dislocation	28
2.2	Glide motion of a dislocation.	30
2.3	True Burgers vector.	30
2.4	Dislocation reaction.	33
2.5	Width of a dislocation.	37
2.6	Initial disregistry and PN displacement field.	38
2.7	Peierls mechanism.	41
2.8	Gamma surface of the $\{111\}$ -plane of an fcc crystal.	42
2.9	Idealized stress-strain curve.	43
2.10	Phason wall.	47
2.11	Stress strain curve in $i\text{-AlPdMn}$	48
2.12	Peierls mechanism in a quasicrystal.	50
2.13	Cluster-friction mechanism.	51
2.14	Dislocation in the 2D binary tiling.	54
2.15	Simulations in the IBT.	55
3.1	Lennard-Jones potential.	62
3.2	Linked-cell method.	64
3.3	Periodic boundary conditions.	67

3.4	Lees-Edwards boundary conditions.	67
4.1	Visualization of the displacement field and the kinetic energy.	76
4.2	Tile and bond visualization.	79
5.1	Heating simulation of the IBT.	83
5.2	Potential energy versus strain.	84
5.3	Stress-strain curves at various temperatures.	85
5.4	Hydrostatic pressure.	88
5.5	Nucleation of a dislocation loop	89
5.6	Displacement field.	90
5.7	Retiled configurations with Burgers circuits	91
5.8	Gamma surface and Burgers vectors.	92
5.9	Sample with a built-in dislocation.	94
5.10	Stress-strain curves with a built-in dislocation.	95
5.11	Mean square displacements.	96
5.12	Strain-rate-sensitivity.	98
5.13	Displacement field of the moving dislocation.	99
5.14	Retiling visualizations (I).	99
5.15	Retiling visualizations (II).	100
5.16	Dislocation core motion with time.	103
5.17	Position of the dislocation core as a function of time.	104
5.18	Dislocation energy in a hexagonal lattice.	107
5.19	Peierls energy as a function of dislocation width.	109
5.20	Dislocation energy in the 2D binary tiling.	110
5.21	Cut through the dislocation energy landscape.	112
5.22	Dislocation energy landscape in the IBT.	114
5.23	Identification of the dominant obstacles.	116
A.1	Measurement of Poisson's ratio.	126

List of Tables

5.1	Lennard-Jones potential parameters.	82
5.2	Elastic constants and critical strains and stresses.	85
5.3	Velocities and plastic strain rates.	102

Bibliography

- [1] D. SHECHTMAN, I. BLECH, D. GRATIAS, and J. W. CAHN. Metallic Phase with Long-Range Orientational Order and No Translational Symmetry. *Phys. Rev. Lett.*, **53** (20): 1951–1953, 1984.
- [2] R. MIKULLA, J. ROTH, and H.-R. TREBIN. Simulation of shear stress in two-dimensional decagonal quasicrystals. *Phil. Mag. B*, **71** (5): 981–989, 1995.
- [3] R. MIKULLA, J. ROTH, and H.-R. TREBIN. Plastic behaviour of quasicrystals: Shearing a two-dimensional binary tiling model in a nonequilibrium–molecular–dynamics simulation. In Ch. Janot and R. Mosseri, editor, *Proceedings of the 5th International Conference on Quasicrystals*, pages 298–305. World Scientific, 1995.
- [4] L. PAULING. Apparent icosahedral symmetry is due to directed, multiple twinning of cubic crystals. *Nature*, **317** (5): 512–514, 1985.
- [5] D. LEVINE and P. J. STEINHARDT. Quasicrystals: a new class of ordered structures. *Phys. Rev. Lett.*, **53** (26): 2477–2480, 1984.
- [6] L. BENDERSKY. Quasicrystal with One-Dimensional Translational Symmetry and a Tenfold Rotation Axis. *Phys. Rev. Lett.*, **55** (14): 1461–1463, 1985.
- [7] N. WANG, H. CHEN, and K. H. KUO. Two-dimensional quasicrystal with eightfold rotational symmetry. *Phys. Rev. Lett.*, **59**: 1010–1013, 1987.

- [8] T. ISHIMASA, H.-U. NISSEN, and Y. FUKANO. New Ordered State Between Crystalline and Amorphous in Ni-Cr Particles. *Phys. Rev. Lett.*, **55** (5): 511–513, 1985.
- [9] L. X. HE, X. Z. LI, Z. ZHANG, and K. H. KUO. One-Dimensional Quasicrystal in Rapidly Solidified Alloys. *Phys. Rev. Lett.*, **61**: 1116–1118, 1988.
- [10] B. DUBOST, J. M. TANAKA, P. SAINFORT, and M. AUDIER. Large AlCuLi single quasicrystals with triacontahedral solidification morphology. *Nature*, **324**: 48–50, 1986.
- [11] T. C. LUBENSKY, J. E. S. SOCOLAR, P. J. STEINHARDT, P. A. BANCEL, and P. A. HEINEY. Distortion and Peak Broadening in Quasicrystal Diffraction Patterns. *Phys. Rev. Lett.*, **57** (12): 1440–1443, 1986.
- [12] JOSHUA E. S. SOCOLAR, T. C. LUBENSKY, and PAUL J. STEINHARDT. Phonons, phasons, and dislocations in quasicrystals. *Phys. Rev. B*, **34** (5): 3345–3360, 1986.
- [13] I. R. FISHER, M. J. KRAMER, Z. ISLAM, T. A. WIENER, A. KRACHER, A. R. ROSS, T. A. LOGRASSO, A. I. GOLDMAN, and P. C. CANFIELD. Growth of large single-grain quasicrystals from high-temperature metallic solutions. *Mater. Sci. Eng. A*, **294-296**: 10–16, 2000.
- [14] R. WITTMANN. *Elektronenmikroskopische, metallurgische und mechanische Untersuchungen der dekadonalen Phase im System Al-Co-Cu(-Si)*. PhD thesis, KFA Jülich, 1993.
- [15] A.-P. TSAI, A. INOUE, and T. MASUMOTO. A stable quasicrystal in Al-Cu-Fe system. *Jpn. J. Appl. Phys.*, **26**: L1505 L1507, 1987.
- [16] M. BOISSIEU, M. DURAND-CHARRE, P. BASTIE, A. CARABELLI, M. BOUDARD, M. BESIÈRE, S. LEFÈBVRE, and C. JANOT. Centimetre-size single grain of the perfect Al-Pd-Mn icosahedral phase. *Phil. Mag. Lett.*, **65** (3): 147–153, 1992.

- [17] A. P. TSAI, J. Q. GUO, E. ABE, H. TAKAKURA, and T. J. SATO. A stable binary quasicrystal. *Nature*, **408**: 537–538, 2000.
- [18] C. BERGER. Electronic properties of quasicrystals experimental. In *Lectures on Quasicrystals*. Les éditions de physique, Les Ulis, 1994.
- [19] J.-M. DUBOIS, S. S. KANG, and Y. MASSIANI. Application of quasicrystalline alloys to surface coating of soft metals. *J. Non-Cryst. Solids*, **153 & 154**: 443–445, 1993.
- [20] F. HIPPERT and D. GRATIAS, editor. *Lectures on Quasicrystals*. Les Editions de Physique, Les Ulis, 1994.
- [21] JEAN-MARIE DUBOIS. Quasicrystals. *J. Phys. Cond. Mat.*, **13** (34): 7753–7762, 2001.
- [22] R. PENROSE. The Rôle of Aesthetics in Pure and Applied Mathematical Research. *Bull. Inst. Math. and its Appl.*, **10**: 266–271, 1974.
- [23] P. KRAMER and R. NERI. Non-periodic central space filling with icosahedral symmetry using copies of seven elementary cells. *Acta Crystallogr. Sect. A*, **38**: 257–264, 1982.
- [24] P. KRAMER and R. NERI. On Periodic and Non-Periodic Space Fillings of \mathbb{E}^3 Obtained by Projection. *Acta Crystallogr. Sect. A*, **40**: 580–587, 1984.
- [25] J. P. POUGET, G. SHIRANE, J. M. HASTINGS, A. J. HEEGER, N. D. MIRO, and A. G. MACDIARMID. Elastic neutron scattering of the “phase ordering” phase transition in $\text{Hg}_{3-\delta}\text{AsF}_6$. *Phys. Rev. B*, **18** (7): 3645–3657, 1978.
- [26] M. DUNEAU and A. KATZ. Quasiperiodic patterns. *Phys. Rev. Lett.*, **54**: 2688–2691, 1985.
- [27] V. ELSER. Indexing problems in quasicrystal diffraction. *Phys. Rev. B*, **32** (8): 4892–4898, 1985.

- [28] D. LEVINE, T. C. LUBENSKY, S. OSTLUND, S. RAMASWAMY, P. J. STEINHARDT, and J. TONER. Elasticity and Dislocations in Pentagonal and Icosahedral Quasicrystals. *Phys. Rev. Lett.*, **54** (14): 1520–1523, 1985.
- [29] T. C. LUBENSKY, S. RAMASWAMY, and J. TONER. Hydrodynamics of icosahedral quasicrystals. *Phys. Rev. B*, **32** (11): 7444–7452, 1985.
- [30] P. A. KALUGIN and A. KATZ. A mechanism for self-diffusion in quasi-crystals. *Europhys. Lett.*, **21** (9): 921–926, 1993.
- [31] R. BLÜHER, P. SCHARWAECHTER, W. FRANK, and H. KRONMÜLLER. First Low-Temperature Radiotracer Studies of Diffusion in Icosahedral Quasicrystals. *Phys. Rev. Lett.*, **80** (5): 1014–1017, 1998.
- [32] K. EDAGAWA, K. SUZUKI, and S. TAKEUCHI. High Resolution Transmission Electron Microscopy Observation of Thermally Fluctuating Phasons in Decagonal Al-Cu-Co. *Phys. Rev. Lett.*, **85** (8): 1674–1677, 2000.
- [33] C. L. HENLEY and V. ELSER. Quasicrystal structure of $(\text{Al}, \text{Zn})_{49}\text{Mg}_{32}$. *Phil. Mag. B*, **53** (3): L59 L66, 1986.
- [34] T. KUPKE, H. R. TREBIN, and S. HOFFMANN. Planes and rows in quasilattices. *Journal Non-Cryst. Sol.*, **153,154**: 196–200, 1993.
- [35] J. P. HIRTH and J. LOTHE. *Theory of dislocations*. J. Wiley and Sons, New York, 1982.
- [36] A. H. COTTRELL. *Theory of Crystal Dislocations*. Blackie and Son Ltd., London, Glasgow, 1964.
- [37] V. I. VLADIMIROV. *Einführung in die physikalische Theorie der Plastizität und Festigkeit*. VEB Deutscher Verlag für Grundstoffindustrie, 1976.
- [38] J. FRIEDEL. *Dislocations*, volume 3 of *International Series of Monographs on Solid State Physics*. Pergamon Press, Oxford, 1964.

- [39] F. R. N. NABARRO. *Theory of Crystal Dislocations*. The international series of monographs on physics. Clarendon Press, Oxford, 1967.
- [40] J. FRENKEL. Zur Theorie der Elastizitätsgrenze und der Festigkeit kristallinischer Körper. *Z. Phys.*, **37**: 572–609, 1926.
- [41] G. I. TAYLOR. The Mechanism of Plastic Deformation of Crystals. Part I. — Theoretical. *Proc. R. Soc. London, Ser. A*, **145**: 362–415, 1934.
- [42] E. OROWAN. Zur Kristallplastizität. III. über den Mechanismus des Gleitvorganges. *Z. Phys.*, **89**: 636–659, 1934.
- [43] M. POLANYI. Über eine Art Gitterstörung, die einen Kristall plastisch machen könnte. *Z. Phys.*, **89**: 660–664, 1934.
- [44] J. M. BURGERS. Some considerations on the fields of stress connected with dislocations in a regular crystal lattice. I. *Proc. Kon. Ned. Akad. v. Wetensch*, **42** (4): 293–325, 1939. siehe Burgers1939b.
- [45] J. M. BURGERS. Some considerations on the fields of stress connected with dislocations in a regular crystal lattice. II. (Solutions of the equations of elasticity for a non-isotropic substance of regular crystalline symmetry.). *Proc. Kon. Ned. Akad. v. Wetensch*, **42** (5): 378–399, 4 1939. siehe Burgers1939a.
- [46] F. C. FRANK. Crystal Dislocations — Elementary Concepts and Definitions. *Phil. Mag.*, **51**: 809–819, 1951.
- [47] E. SCHMID. Beiträge zur Physik und Metallographie des Magnesiums. **37**: 447–459, 1931.
- [48] M. PEACH and J. S. KOEHLER. The Forces Exerted on Dislocations and the Stress Fields Produced by Them. *Phys. Rev.*, **80** (3): 436–439, 1950.
- [49] F. C. FRANK and W. T. READ. *Symposium on Plastic Deformation of Crystalline Solids*. , 1950.
- [50] F. C. FRANK. ? *Physica*, **15**: 131, 1949.

- [51] U. DEHLINGER and A. KOCHENDÖRFER. Eigenbewegungen in Kristallgittern. *Z. Phys.*, **116**: 576–585, 1940.
- [52] J. I. FRENKEL and T. A. KONTOROVA. On the theory of plastic deformation and twinning I. *Phys. Z. Sowjetunion*, **18**: 1–10, 1938.
- [53] R. PEIERLS. The Size of a Dislocation. *Proc. Phys. Soc. London*, **52**: 34–37, 1940.
- [54] F. R. N. NABARRO. Dislocations in a simple cubic lattice. *Proceedings of Phys. Society*, **59**: 256–272, 1947.
- [55] A. J. FOREMAN, M. A. JASWON, and J. K. WOOD. Factors controlling dislocation widths. *Proc. Phys. Soc. London, Sect. A*, **64**: 156–163, 1950.
- [56] A. H. COTTRELL and F. R. N. NABARRO. *Dislocations and Plastic Flow in Crystals*. The International Series of Monographs on Physics. Oxford Clarendon Press, IX edition, 1953.
- [57] JIAN N. WANG. A new modification of the formulation of Peierls stress. *Acta Mater.*, **44** (4): 1541–1546, 1996.
- [58] V. VÍTEK. Theory of the core structures of dislocations in body-centered-cubic metals. *Cryst. Latt. Def.*, **5**: 1–34, 1974.
- [59] A. G. EVANS and R. D. RAWLINGS. The Thermally Activated Deformation of Crystalline Materials. *Phys. Stat. Sol.*, **34**: 9–31, 1969.
- [60] J. BACHTELER and H.-R. TREBIN. Elastic Green's function of icosahedral quasicrystals. *Eur. Phys. J. B*, **4** (3): 299–306, 1998.
- [61] S. RANGANATHAN, KCHATTOPADHYAY, A. SINGH, and K. F. KELTON. Decagonal Quasicrystals. *Prog. Mat. Sci.*, **41** (4): 195–240, 1997.
- [62] U. KOESTER, W. LIU, H. LIEBERTZ, and M. MICHEL. Mechanical properties of quasicrystalline and crystalline phases in Al–Cu–Fe alloys. **153 & 154**: 446–452, 1993.

- [63] T. SHIBUYA, T. HASHIMOTO, and S. TAKEUCHI. Plastic Deformation of Al–Ru–Cu Icosahedral Quasicrystals. *Jpn. J. Appl. Phys.*, **29** (2): L 349 L 351, 1990.
- [64] S. S. KANG and J. M. DUBOIS. Compression testing of quasicrystalline materials. *Phil. Mag. A*, **66** (1): 151–163, 1992.
- [65] L. BRESSON and D. GRATIAS. Plastic deformation in AlCuFe icosahedral phase. *J. Non-Cryst. Solids*, **153** & **154**: 468–472, 1993.
- [66] S. TAKEUCHI and T. HASHIMOTO. Plastic Deformation of Al–Pd–Mn Icosahedral Quasicrystal. *Jpn. J. Appl. Phys., Pt. 1*, **32** (5A): 2063–2066, 1993.
- [67] J. FRIEDEL. Quasicrystals Introduction. In C. Janot and R. Mosseri, editor, *Proceedings of the 5th International Conference on Quasicrystals*, pages 5–11. 1995.
- [68] M. WOLLGARTEN, M. BEYSS, K. URBAN, H. LIEBERTZ, and U. KÖSTER. Direct Evidence for Plastic Deformation of Quasicrystals by Means of a Dislocation Mechanism. *Phys. Rev. Lett.*, **71** (4): 549–552, 1993.
- [69] T. H. COURTNEY. *Mechanical Behavior of Materials*. Mc Graw-Hill Series in Material Science and Engineering. Mc Graw-Hill, 1990.
- [70] E. KABUTOYA, K. EDAGAWA, R. TAMURA, S. TAKEUCHI, J. Q. GUO, and A.-P. TSAI. Plastic deformation of icosahedral Al–Pd–Mn single quasicrystals to large strains I. Experiments. *Phil. Mag. A*, **82** (2): 369–377, 2002.
- [71] M. WOLLGARTEN and H. SAKA. Microstructural investigation of the brittle-to-ductile transition in Al–Pd–Mn quasicrystals. *Phil. Mag. A*, **79** (9): 2195–2208, 1999.
- [72] M. WOLLGARTEN and K. URBAN. Comment on ‘convergent-beam electron diffraction study of the burgers vector of dislocations in icosahedral Al–Cu–Fe alloy’. *Phil. Mag. Lett.*, **68** (5): 273–277, 1993.

- [73] M. WOLLGARTEN, M. BARTSCH, U. MESSERSCHMIDT, M. FEUERBACHER, R. ROSENFELD, M. BEYSS, and K. URBAN. *In-situ* observation of dislocation motion in icosahedral Al-Pd-Mn single quasicrystals. *Phil. Mag. Lett.*, **71** (2): 99–105, 1995.
- [74] P. B. HIRSCH, A. HOWIE, and M. J. WHELAN. nachlesen. *Philos. Trans. R. Soc. London, Ser. A*, **252**: 499–529, 1960.
- [75] M. WOLLGARTEN, D. GRATIAS, Z. ZHANG, and K. URBAN. On the determination of the Burgers vector of quasicrystal dislocations by transmission electron microscopy. *Phil. Mag. A*, **64** (4): 819–833, 1991.
- [76] M. WOLLGARTEN, Z. ZHANG, and K. URBAN. Diffraction contrast of quasicrystalline dislocations in the transmission electron microscope. *Phil. Mag. Lett.*, **65** (1): 1–6, 1992.
- [77] M. TANAKA, K. UENO, and Y. HARADA. . *J. Electron Mic.*, **29**: 408, 1980.
- [78] R. ROSENFELD, M. FEUERBACHER, B. BAUFELD, M. BARTSCH, M. WOLLGARTEN, G. HANKE, M. BEYSS, U. MESSERSCHMIDT, and K. URBAN. Study of plastically deformed icosahedral Al-Pd-Mn single quasicrystals by transmission electron microscopy. *Phil. Mag. Lett.*, **72** (6): 375–384, 1995.
- [79] U. MESSERSCHMIDT, M. BARTSCH, B. GEYER, M. FEUERBACHER, and K. URBAN. Plastic deformation of icosahedral Al-Pd-Mn single quasicrystals II. Interpretation of the experimental results. *Phil. Mag. A*, **80** (5): 1165–1181, 2000.
- [80] R. WANG, M. FEUERBACHER, W. YANG, and K. URBAN. Stacking faults in high-temperature-deformed Al-Pd-Mn icosahedral quasicrystals. *Phil. Mag. A*, **78** (2): 273–284, 1998.
- [81] U. MESSERSCHMIDT, M. BARTSCH, M. FEUERBACHER, B. GEYER, and K. URBAN. Friction mechanism of dislocation motion in icosahedral Al-Pd-Mn quasicrystals. *Phil. Mag. A*, **79** (9): 2123–2135, 1999.

- [82] M. BOUDARD and ET.AL. Neutron and x-ray single-crystal study of the AlPdMn icosahedral phase. *J. Phys. Cond. Mat.*, **4**: 10149–10168, 1992.
- [83] R. TAMURA, S. TAKEUCHI, and K. EDAGAWA. Dislocation and shear strength of model quasiperiodic lattice. *Mater. Sci. Eng. A*, **309-310**: 552–556, 2001.
- [84] K. EDAGAWA. Dislocations in quasicrystals. *Mater. Sci. Eng. A*, **309-310**: 528–538, 2001.
- [85] S. TAKEUCHI, R. TAMURA, E. KABUTOYA, and K. EDAGAWA. Plastic deformation of icosahedral Al-Pd-Mn single quasicrystals to large strains II. Deformation mechanism. *Phil. Mag. A*, **82** (2): 379–385, 2002.
- [86] M. FEUERBACHER, C. METZMACHER, M. WOLLGARTEN, K. URBAN, B. BAUFELD, M. BARTSCH, and U. MESSERSCHMIDT. Dislocations and plastic deformation of quasicrystals. *Mater. Sci. Eng. A*, **226-228**: 943–949, 1997.
- [87] D. BRUNNER, D. PLACHKE, and H. D. CARSTANJEN. The temperature and strain-rate dependence of the flow stress of icosahedral AlPdMn single-quasicrystals. *Mater. Sci. Eng. A*, **234-236**: 310–313, 1997.
- [88] U. MESSERSCHMIDT, D. HÄUSSLER, M. BARTSCH, B. GEYER, M. FEUERBACHER, and K. URBAN. Microprocesses of the plastic deformation of icosahedral Al-Pd-Mn single quasicrystals. In F. Gähler, H.-R. Trebin, P. Kramer, and K. Urban, editor, *Proceedings of the 7th international conference on quasicrystals*, volume 294-296, pages 757–760. 2000.
- [89] D. PLACHKE. Files für die experimentellen rbs- und pixe-daten an dekadonalen $\text{Al}_{62}\text{Cu}_{20}\text{Co}_{15}\text{Si}_3$, 1998. Persönliche Mitteilung.
- [90] PH.EBERT, M. FEUERBACHER, N. TAMURA, M. WOLLGARTEN, and K. URBAN. Evidence for a Cluster-Based Structure of AlPdMn Single Quasicrystals. *Phys. Rev. Lett.*, **77** (18): 3827–3830, 1996.

- [91] R. LABUSCH and R. B. SCHWARZ. . In D. G. Brandon, R. Chaim, and A. Rosen, editor, *Strength of metals and alloys*, page 47. 1991.
- [92] RALF MIKULLA. *Atomistische Studien zur Versetzungsbewegung in zweidimensionalen Quasikristallen*. PhD thesis, Universität Stuttgart, 1996.
- [93] R. MIKULLA, F. KRUL, P. GUMBSCH, and H.-R. TREBIN. Numerical simulations of dislocation motion and crack propagation in quasicrystals. In A. I. Goldman, D. J. Sordelet, P. A. Thiel, and J. M. Dubois, editor, *New horizons in quasicrystals: Research and applications*, pages 200–207. World Scientific, 1997.
- [94] R. MIKULLA, J. STADLER, P. GUMBSCH, and H.-R. TREBIN. Molecular Dynamics Simulations of Crack Propagation in Quasicrystals. In S. Takeuchi and T. Fujiwara, editor, *Proceedings of the 6th International Conference on Quasicrystals*, pages 485–492. World Scientific, 1997.
- [95] F. LANÇON and L. BILLARD. Thermodynamical Properties of a Two-Dimensional Quasicrystal from Molecular Dynamics Calculations. *Europhys. Lett.*, **2** (8): 625–629, 1986.
- [96] F. LANÇON and L. BILLARD. Two-dimensional system with a quasi-crystalline ground state. *J. Phys. France*, **49**: 249–256, 1988.
- [97] R. MIKULLA, P. GUMBSCH, and H.-R. TREBIN. Dislocations in quasicrystals and their interaction with cluster-like obstacles. *Phil. Mag. Lett.*, **78** (5): 369–376, 1998.
- [98] R. MIKULLA, J. STADLER, F. KRUL, H.-R. TREBIN, and P. GUMBSCH. Crack Propagation in Quasicrystals. *Phys. Rev. Lett.*, **81** (15): 3163–3166, 1998.
- [99] C. DILGER, R. MIKULLA, J. ROTH, and H.-R. TREBIN. Simulation of shear stress in icosahedral quasicrystals. *Phil. Mag. A*, **75** (2): 425–441, 1997.
- [100] G. D. SCHAAF, J. ROTH, H.-R. TREBIN, and R. MIKULLA. Numerical simulation of dislocation motion in three-dimensional icosahedral quasicrystals. *Phil. Mag. A*, **80** (7): 1657–1668, 2000.

- [101] S. J. ZHOU, D. M. BEAZLEY, P. S. LOMDAHL, and B. L. HOLIAN. Large-Scale Molecular Dynamics Simulations of Three-Dimensional Ductile Failure. *Phys. Rev. Lett.*, **78** (3): 479–482, 1996.
- [102] G. D. SCHAAF, R. MIKULLA, J. ROTH, and H.-R. TREBIN. Numerical simulation of dislocation motion in an icosahedral quasicrystal. In F. Gähler, P. Kramer, H.-R. Trebin, and K. Urban, editor, *Proceedings of the 7th International Conference on Quasicrystals*, volume 294-296, pages 799–802. 2000.
- [103] M. P. ALLEN and D. J. TILDESLEY. *Computer Simulation of Liquids*. Oxford Science Publications, 1987.
- [104] J. STADLER, R. MIKULLA, and H.-R. TREBIN. IMD: a software package for molecular dynamics studies on parallel computers. *Int. J. Mod. Phys. C*, **8** (5): 1131–1140, 1997.
- [105] J. ROTH, J. STADLER, M. BRUNELLI, F. GÄHLER, J. HAHN, M. HOHL, C. HORN, R. MIKULLA, G. SCHAAF, and H.-R. TREBIN. *Molecular Dynamics Simulations with IMD*, volume XII, pages 169–173. Springer, 2000.
- [106] J. SCHIØTZ. *Molecular Dynamics of Mesoscopic Systems*. PhD thesis, Technical university of Denmark, Lyngby, January 1995.
- [107] L. VERLET. Computer "Experiments" on Classical Fluids. I. Thermodynamical Properties of Lennard-Jones Molecules. *Phys. Rev.*, **159** (1): 98–103, 1967.
- [108] B. QUENTREC. New Method for Searching of Neighbors in Molecular Dynamics Computations. *J. Comput. Phys.*, **13**: 430–432, 1973.
- [109] J. ROTH, F. GÄHLER, and H.-R. TREBIN. A molecular dynamics run with 5.180.116.000 particles. *Int. J. Mod. Phys. C*, **11** (2): 317–322, 2000.
- [110] A. W. LEES and S. F. EDWARDS. The computer study of transport processes under extreme conditions. *J. Phys. C*, **5**: 1921–1929, 1972.

- [111] S. NOSÉ. A Unified Formulation of the Constant Temperature Molecular Dynamics Methods. *J. Chem. Phys.*, **81** (1): 511–519, 1984.
- [112] S. NOSÉ. A Molecular Dynamics Method for Simulations in the Canonical Ensemble. *Mol. Phys.*, **52** (2): 255–268, 1984.
- [113] S. NOSÉ. *Molecular dynamics at constant temperature and pressure*, pages 21–41. Kluwer Academic Publishers, 1991. Computer Simulation in Materials Science.
- [114] W. G. HOOVER. Canonical dynamics: Equilibrium phase–space distributions. *Phys. Rev. A*, **31** (3): 1695–1697, 1985.
- [115] H. C. ANDERSEN. Molecular dynamics simulations at constant pressure and/or temperature. *J. Chem. Phys.*, **72** (4): 2384–2393, 1980.
- [116] J. R. BEELER. *Radiation Effects Computer Simulations*, volume 13. North Holland Amsterdam, New York, Oxford, 1983.
- [117] R. KUBO. Statistical-mechanical theory of irreversible processes I. General theory and simple application to magnetic and conduction problems. *J. Phys. Soc. Jpn.*, **12**: 570, 1957.
- [118] B. ALDER and T. WAINWRIGHT. Studies in Molecular Dynamics. I. General Method. *J. Chem. Phys.*, **31** (2): 459–466, 1959.
- [119] W. T. ASHURST and W. G. HOOVER. Dense-fluid shear viscosity via nonequilibrium molecular dynamics. *Phys. Rev. A*, **11** (2): 658–678, 1975.
- [120] W. G. HOOVER, A. J. C. LADD, R. B. HICKMAN, and B. L. HOLIAN. Bulk viscosity via nonequilibrium and equilibrium molecular dynamics. *Phys. Rev. A*, **21** (5): 1756–1760, 1980.
- [121] W. G. HOOVER, D. J. EVANS, R. B. HICKMAN, A. J. C. LADD, W. T. ASHURST, and B. MORAN. Lennard-Jones triple-point bulk and shear viscosities. Green-Kubo theory, Hamiltonian mechanics, and non-equilibrium molecular dynamics. *Phys. Rev. A*, **22** (4): 1690–1697, 1980.

-
- [122] D. J. EVANS and G. P. MORRIS. Non-Newtonian molecular dynamics. *Comp. Phys. Rep.*, **1**: 297–344, 1984.
- [123] D. J. EVANS and G. P. MORRIS. *Statistical Mechanics of Nonequilibrium Liquids*. Academic Press, San Diego, 1990.
- [124] J. SCHULZE-DÖBOLD, R. NIEMEIER, and U. LANG. The Perspective Shear-Warp Algorithm in a Virtual Environment. In *Proceedings of IEEE Visualization 2001*, pages 201–213. 2001.
- [125] JOHANNES ROTH. *Thermodynamische Stabilität von Quasikristallen und der Einfluß von Frenkeldefekten*. PhD thesis, Universität Stuttgart, February 1992.
- [126] D. LORENZ. *Untersuchungen zur homogenen Versetzungsnukleation mittels Nanoindentierung*. PhD thesis, Martin-Luther-Universität Halle-Wittenberg, 2001.
- [127] C. P. RUDHART. to be published.
- [128] C. L. HENLEY. All 3D Penrose Tiling Local Environments. Technical report, 1985.
- [129] C. L. HENLEY. Sphere packings and local environments in Penrose tilings. *Phys. Rev. B*, **34** (2): 797–816, 1986.
- [130] L. D. LANDAU and E. M. LIFSHITZ. *Theory of elasticity*, volume 7 of *Course of theoretical physics*. , 1959.

Glossary

- 3D visualizations, [56](#)
- 3D Penrose tiling, [18](#)
- algorithm
 - leap-frog, [62](#)
- activation parameters, [44](#)
- activation area, [45](#)
- activation volume, [45](#)
- algorithm
 - synthetic, [72](#)
- amorphous structures, [15](#)
- approximant, [21](#)
- basis, [16](#)
- bonds, [16](#)
- boundaries
 - fixed, [65](#)
 - free, [65](#)
 - Lees-Edwards, [66](#)
 - periodic, [66](#)
- boundary conditions, [65](#)
- Bragg peaks, [16](#)
- brittle-to-ductile transition, [47](#)
- Burgers circuit, [31](#)
- Burgers vector, [29](#)
 - local, [31](#)
 - true, [31](#)
- cluster friction mechanism, [52](#)
- configuration, [124](#)
- coordinate
 - Eulerian, [123](#)
 - Lagrangian, [123](#)
 - material, [123](#)
 - spatial, [123](#)
- crystals, [15](#)
- cut and project method, [20](#)
- cut-off radius, [63](#)
- decoration, [19](#)
- deformation, [124](#)
- density-wave description, [22](#)
- diffraction pattern, [16](#)
- diffusion, [23](#)
- diffusion coefficient, [60](#)
- dislocation
 - climb, [29](#)
 - core, [31](#)
 - density, [34](#)
 - displacement field, [32](#)
 - elastic energy, [33](#)
 - glide, [29](#)
 - line, [29](#)
 - mixed, [29](#)
 - node, [32](#)

- partial, 35, 42
- Peierls-Nabarro, 37, 39
- perfect, 35
- reaction, 32
- stress field, 33
- width, 36
- displacement field
 - Peierls-Nabarro, 39
- Doll's tensor, 72
- edge dislocation, 28
- Einstein frequency, 69
- electron diffraction, 16
- ensemble, 59
 - canonical (NVT), 68
 - global convergence (GLOC), 70
 - isothermal-isobaric (NPT), 69
 - microcanonical (NVE), 68
 - microconvergence (MIC), 70
- ensemble average, 59
- equations of motion
 - Doll's, 72
 - Hamiltonian, 57
 - SLLOD, 72
- ergodic, 59
- extinction condition, 49
 - strong, 49
 - weak, 49
- Fibonacci chain, 21
- Frank-Read source, 35
- function
 - quasiperiodic, 18
- gamma surface, 42
- golden mean, 19
- i-AlMgZn, 24
- i-AlPdMn, 13
- icosahedral binary tiling, 23
- IMD, 58
- index, 17
- integrator, 61
- kink, 41
- kink pair, 41
- Kubo relation, 71
- lattice, 16
 - crystalline, 16
 - reciprocal, 17
- Lennard-Jones potential, 63
- line tension approximation, 35
- line tension force, 35
- linked-cell method, 64
- minimum-image convention, 66
- molecular dynamics, 57
- nearest neighbors, 16
- non-equilibrium molecular dynamics (NEMD), 71
- Nosé-Hoover thermostat, 68
- order
 - crystalline, 13
 - orientational, 16
 - translational, 13, 15
- Orowan equation, 44
- parallelization, 65
- Peierls mechanism, 41
- Peierls energy, 40
- Peierls hill, 41
- Peierls stress, 40
- Peierls valley, 41

- Penrose tiling, 17
- perpendicular space, 20
- phase space, 58
- phase space density, 59
- phason flip, 22
- phason displacement, 22
- phason strain, 15
- phason wall, 46
- physical space, 20
- plastic flow, 44
- plastic strain, 44
- plastic strain rate, 44
- plasticity, 43
 - thermally activated, 44
- quasicrystal, 13
- quasicrystals
 - decagonal, 14
 - dodecagonal, 14
 - octagonal, 14
 - one-dimensional, 14
- quasilattice, 17
- reference state, 123
- relaxation, 70
- relaxation algorithms, 70
- resolved shear stress, 34
- retiling, 77
- rhombic dodecahedron, 22
- rhombohedron
 - oblate, 23
 - prolate, 23
- Schmid factor, 34
- screw dislocation, 28
- Shockley partials, 42
- slip, 27
- slip bands, 27
- slip plane, 27
- softening, 48
- splitting, 32
- stacking fault, 42
- statistical mechanics, 58
- strain accommodation parameter, 50
- stress relaxation experiment, 44
- strip, 20
- structure
 - incommensurate, 19
 - quasicrystalline, 19
 - translationally ordered, 17
- structure factor, 17
- symmetry
 - icosahedral, 13
 - non-crystallographic, 14, 17
- T-phases, 14
- ten-fold rings, 53
- theoretical shear strength, 28
- tile, 18
- time average, 59
- time step, 61
- trajectories, 58
- unit cell, 16
- virial, 60
- work hardening, 44
- x-ray diffraction, 16
- yield stress, 44

Lebenslauf von Gunther Schaaf

15.4.1971	geboren in Stuttgart
1978-1982	Martin-Luther-Grundschule Stuttgart
1982-1991	Johannes-Kepler-Gymnasium Stuttgart
Juni 1991	Abitur
1991-1992	Zivildienst
1992-1998	Studium der Physik an der Universität Stuttgart
1994-1999	Studium der Mathematik an der Universität Stuttgart
Mai 1998	Diplom in Physik
seit Juli 1998	Promotion bei Prof. Dr. H.-R. Trebin Institut für Theoretische und Angewandte Physik Universität Stuttgart
Februar 1999	Diplom in Mathematik
seit 14.7.2000	verheiratet mit Silke, geb. Kubin

Veröffentlichungen:

G. Schaaf: Numerische Simulation des mechanischen Verhaltens von Quasikristallen, Diplomarbeit, Universität Stuttgart, Mai 1998

G. Schaaf, J. Roth, H.-R. Trebin, and R. Mikulla: Numerical simulation of dislocation motion in three-dimensional icosahedral quasicrys-

tals, *Phil. Mag. A* **80**: 1657–1668, 2000.

G. Schaaf, R. Mikulla, J. Roth, and H.-R. Trebin: Numerical simulation of dislocation motion in an icosahedral quasicrystal, *Mater. Sci. Eng. A* **294–296**: 799–802, 2000.

Danksagung

An dieser Stelle möchte ich einigen Menschen danken, die auf verschiedene Weise zum Gelingen dieser Arbeit beigetragen haben.

Herrn Prof. Dr. Hans-Rainer Trebin danke ich für die freundliche Aufnahme am Institut für Theoretische und Angewandte Physik (ITAP) sowie für die herausfordernde Aufgabenstellung und die Unterstützung bei ihrer Bearbeitung.

Herrn Prof. Dr. Günter Wunner danke ich für die Übernahme des Mitberichts.

Herr Prof. Dr. Peter Gumbsch vom Fraunhofer Institut für Werkstoffmechanik, Freiburg und Halle hat dieser Arbeit viel seiner Zeit gewidmet. Den Diskussionen mit ihm entsprangen zahlreiche Ideen zur Interpretation der erhaltenen Ergebnisse.

Herr Prof. Dr. Ulrich Messerschmidt vom Max-Planck-Institut für Mikrostrukturphysik, Halle verdanke ich wertvolle Anregungen aus der Sicht eines Experimentators.

Dr. Ralf Mikulla war mein Betreuer während der Diplomarbeit. Von ihm habe ich einen hervorragenden Einblick in das Arbeitsgebiet erhalten.

Dr. Johannes Roth hat mir verschiedene Programme zur Konstruktion quasikristalliner Strukturen überlassen. Ich konnte auch von seinem großen Wissen sowohl auf dem Gebiet der Simulation als auch über die Administration von Rechnern profitieren.

Dr. Franz Gähler hat das institutseigene Simulationsprogramm IMD verwaltet und viele Änderungen und Verbesserungen eingeführt, insbesondere im Hinblick auf die Simulation bei vorgegebener Temperatur. Besonderer Dank gebührt ihm für die geduldige Beantwortung unzähliger Fragen zu Tilings und allem, was dazugehört.

In Christoph Rudhart fand ich einen idealen Diskussionspartner, da er fast alles kritisch hinterfragte. Die Gespräche mit ihm haben viel zu meinem Verständnis des Gebietes der Quasikristallplastizität beigetragen. Auch gebührt ihm zusammen mit Johannes Roth und Franz Gähler Dank für das Korrektur lesen dieser Arbeit.

Michael Reichenstein hat als Tex-Manager für eine perfekte Arbeitsumgebung gesorgt. Seine Beratung in Sachen Layout hat mir bei der Erstellung dieses Dokumentes sehr oft weiter geholfen.

Ohne sie alle aufzuzählen bedanke mich bei den Mitarbeitern des ITAPs und des Sekretariats für die angenehme Arbeitsatmosphäre und die schöne Zeit, die ich hier verbracht habe. Die große Hilfsbereitschaft, auf die ich traf, hat wesentlich zum Gelingen dieser Arbeit beigetragen.

Holger Kollmer, Steffen Krusch, Marc Lätzel und Markus Schulte haben mich durch mein Studium hindurch begleitet. Ihnen danke ich für viele interessante Gespräche und Hinweise zu meiner Arbeit.

Meinen Eltern gebührt mein ganz besonderer Dank dafür, dass sie mir meine Ausbildung ermöglicht haben.

Ich danke meiner Frau Silke für ihren Zuspruch in schwierigen Phasen dieser Arbeit und ihr Verständnis. Meinem Sohn Cedric danke ich für viele schöne Stunden, einige davon nachts, in denen er es mühelos schaffte, mich von der Quasikristallplastizität und den damit verbundenen Problemen abzulenken.

Zuletzt danke ich der Deutschen Forschungsgemeinschaft, die im Rahmen des Sonderforschungsbereiches 382 (Verfahren und Algorithmen zur Simulation physikalischer Prozesse auf Höchstleistungsrechnern) diese Arbeit finanziell gefördert hat.